# Nanocarbon-based sheets
## Advances in processing methods and applications

Kostaras, Christos ; Pavlou, Christos ; Galiotis, Costas ; Dassios, Konstantinos G.

**DOI**
10.1016/j.carbon.2024.118909

**Publication date**
2024

**Document Version**
Final published version

**Published in**
Carbon

**Citation (APA)**
Kostaras, C., Pavlou, C., Galiotis, C., & Dassios, K. G. (2024). Nanocarbon-based sheets: Advances in processing methods and applications. *Carbon*, *221*, Article 118909.
https://doi.org/10.1016/j.carbon.2024.118909

Carbon 221 (2024) 118909

Contents lists available at ScienceDirect

Carbon

journal homepage: www.elsevier.com/locate/carbon

# Nanocarbon-based sheets: Advances in processing methods and applications

Christos Kostaras [a], Christos Pavlou [a,b,c], Costas Galiotis [b], Konstantinos G. Dassios [a,*]

[a] University of Patras, Department of Chemical Engineering, Caratheodory 1, 26504, Greece
[b] FORTH/ICE-HT, Stadiou Str., Rion-Patras, 26504, Greece
[c] Delft University of Technology, Department of Microelectronics, Faculty of Electrical Engineering, Mathematics and Computer Science, Delft, 2600 AA, the Netherlands

ARTICLE INFO

*Keywords:*
Carbon nanotubes
Graphene
Cross-linking
Energy storage
EMI shielding
Thermal dissipation
Water treatment

ABSTRACT

As an emerging class of materials, nanocarbons have attracted significant interest for practical applications due to their remarkable mechanical, electrical and thermal properties coupled with high surface areas and tunable surface chemistry. However, challenges like high aspect ratios and poor dispersibility in polymer matrices hinder their widespread use in technological applications. The problems are most prominently resolved with the use of free-standing nanocarbon sheets. The present paper reviews recent advancements in fabricating and utilizing free-standing sheets consisting of various nanocarbons: carbon nanotubes and 2D materials like graphene, graphene oxide, and reduced graphene oxide. It initially delves into the nanomechanics of these sheets, focusing on inter-particle cross-linking and nacre-like microstructures. Energy storage applications are also examined, with emphasis on the role of nanocarbon-based sheets in the enhancement of specific energy capacity and performance retention of batteries, electric double layer supercapacitors, and pseudocapacitors. In the field of electromagnetic interference shielding, the sheets' superior electrical conductivity and microstructures, which amplify internal reflections in the GHz and THz regions, are showcased. Their potential in heat dissipation, owing to their high thermal conductivity and large surface area, is also explored. Additionally, they are reviewed for membrane-based separation processes, specifically gas separation, reverse osmosis, forward osmosis, and pervaporation, highlighting properties like ion selectivity and chlorine resistance. The last discussion concerns the role of nanocarbon-based sheets in catalysis where they can enhance reaction efficiencies and promote sustainable solutions. Either as catalysts and/or supports, with key features such as high surface area, electrical conductivity, and adaptable functionalities, they showcase significant potential in various catalytic processes like electrocatalysis and environmental remediation.

## 1. Introduction

For three decades since their discovery as the newest allotropes of carbon, carbon nanotubes (CNTs) [1] and graphene [2], have attracted impressive scientific attention, owing mostly to their extraordinary properties [3–6]. The two main areas of research focus are the fundamentals of their synthesis and physico-chemical performance, and their exploitation in novel applications. Intriguingly, their nanoscale dimensions that are responsible for their unique properties, are also hindering their ease of handling for introduction into practical macro-structures. The greatest challenge in using the otherwise exotic nanocarbons in everyday life applications is actually the design of macro-formats that can encapsulate them in a manner that permits exploitation of specific properties to the advantage of the application.

### 1.1. *Physical properties of nanocarbons*

Carbon nanotubes (CNTs) and graphene, known for their exceptional physical properties, have significantly impacted materials science and nanotechnology. CNTs, cylindrical nanostructures composed of graphene sheets, come in two forms: single-walled and multi-walled. Single-walled nanotubes typically measure 0.8–2 nm in diameter, while multi-walled nanotubes range from 5 to 20 nm. They are recognized for their strength, being about 100 times stronger than steel with a tensile strength of approximately 63 GPa, yet they are much lighter. The electrical conductivity of CNTs varies based on their chirality, with metallic

---

* Corresponding author.
*E-mail address:* kdassios@upatras.gr (K.G. Dassios).

https://doi.org/10.1016/j.carbon.2024.118909
Received 15 October 2023; Received in revised form 31 January 2024; Accepted 8 February 2024

CNTs exhibiting conductivity around $10^6$ S/m, comparable to that of copper. Their thermal conductivity is also noteworthy, reaching up to 3500 W/mK [7]. Graphene, a single layer of carbon atoms arranged in a two-dimensional honeycomb lattice, exhibits extraordinary physical properties. It is incredibly strong, with an intrinsic tensile strength of about 130 GPa and a Young's modulus of approximately 1 TPa. Graphene is not just strong but also thin, measuring about 0.33 nm thick. Its electrical conductivity is exceptional, surpassing that of silver, presenting values up to $10^8$ S/m. Similarly, graphene's thermal conductivity is around 5000 W/mK, making it an excellent heat conductor. The material also has a remarkable surface area of about 2630 $m^2$/g, useful in applications requiring a high surface-to-volume ratio [8–10].

Moving to graphene derivatives [11], these materials exhibit varied physical properties that extend their applicability. Graphene oxide (GO), produced by the oxidation and exfoliation of graphite, contains oxygen functional groups like hydroxyl, epoxy, and carboxyl [12,13]. These groups make GO hydrophilic and dispersible in water. However, the presence of these oxygen groups in GO results in a decrease in electrical conductivity compared to pristine graphene, while retaining a significant portion of its mechanical strength. Its thermal conductivity is also reduced due to the disruption in the $sp^2$ bonding network [14]. Reduced graphene oxide (rGO) is derived by chemically reducing GO, which partially restores some of the graphene-like structure [15]. The electrical conductivity of rGO is improved compared to GO but remains lower than that of pristine graphene. Similarly, its mechanical and thermal properties are enhanced from GO but do not fully match unmodified graphene. Graphene nanoplates (GNPs), consisting of multiple layers of graphene stacked together, demonstrate a balance between the properties of single-layer graphene and bulk graphite [16,17]. Their electrical and thermal conductivity are high but decrease with an increase in the number of layers. The mechanical strength of GNPs is also strong but less than that of single-layer graphene. Functionalized graphene, achieved by attaching various functional groups or molecules to graphene, displays altered properties depending on the nature of the functionalization. The electrical conductivity and mechanical and thermal properties of functionalized graphene can increase or decrease based on the type of functional groups added.

### 1.2. *Nanocarbon-based sheets*

One of the first macro-structures developed exclusively from carbon nanomaterials which overcame this challenge were the paper-like CNT sheets termed "buckypapers", prefix owed to Buckminster "Bucky" Fuller, the inventor of the geodesic sphere that accurately simulates the structure of the fullerene allotrope of carbon [18]. Buckypapers are self-standing thin paper-like films of highly porous networks of randomly entangled CNTs [19]. It is exactly this entanglement that endows the self-standing feature in the otherwise pure-CNT structure. The papers can be prepared by vacuum filtration, compression and evaporation of well-dispersed CNT suspensions and their internal structure can be controlled by altering the parameters of either the suspension preparation methodology, namely sonication duration and tube concentration, or by post-treatment [20], namely pressing and stretching [21,22]. Most importantly, the highly porous microstructure of buckypapers enables their usage as scaffolds for well-dispersed high filler-loaded composites [23] with good mechanical performance. The latter can be further enhanced by tailoring of the filler-matrix interface through chemical functionalization of the tubes [24] without degradation of their favorable inherent thermal and electrical properties [25].

Using similar methods, graphene-based papers and hybrid CNT/graphene papers can also be fabricated [26]. Depending on flake size and number of layers, graphene can display superior properties than CNTs, as also documented in numerous recent reports on its polymer matrix reinforcing potential, electrical and thermal applications. On the other hand, unless complicated fabrication methods are employed, graphene papers lack the porous structure of CNT-based buckypapers which is highly advantageous, if not indispensable in applications such as energy storage [27], water treatment [28] and EMI shielding [29,30].

The properties of such nanocarbon-based thin films are highly tailorable by tuning of a great number of experimental parameters in their synthesis protocols, as per target application specifications. Accordingly, a big number of publications have in the last two decades reported use of such films in a diverse range of applications [31]. The present manuscript aims to review the most promising and representative latest advances in use of CNTs/graphene papers in each of five major application areas, namely mechanical reinforcement, water treatment, energy storage, electromagnetic interference shielding and heat dissipation.

## 2. Mechanical reinforcement

### 2.1. *Cross-linking of CNTs*

In self-supported buckypapers consisting purely of CNTs, mechanical interlocking and van der Waals forces active on the surface of the tubes are insufficient for efficient stress transfer, hence also plausible mechanical performance. This is not only due to the low values of the forces but also due to the low inter-tube contact surface area expected in entangled networks of 1D materials. Together with open porosity, the effect is also responsible for inefficient electric transfer within the papers. During the last decade, scientific effort has focused on improvement of the stress transfer in the papers via covalent cross-linking of the nanotubes (Table 1).

CNTs can be functionalized through a variety of reactions [32] which result in the decoration of their surfaces with hydroxyl (– OH), carboxyl (– COOH) and epoxide (C–O–C) [19] functionalities. Through a condensation reaction and the use of 1,3-dicyclohexylcarbodiimide (DCC), Ogino et al. [33] achieved the formation of an ester bond between the – OH and – COOH functionalities of acid treated multi-walled CNT (MWCNT) buckypapers. As a result, the ultimate tensile strength (UTS) of the cross-linked MWCNT buckypapers tripled in value. The functionalities can react with various molecules to form covalent bonds thus promoting CNT cross-linking. Jakubinek et al. demonstrated this achievement using a multitude of polymers on acid-functionalized SWCNTs [34]. The aim of their work was to create a cross-linked scaffold for epoxy impregnation; thus, the partial maintenance of porosity was of importance (Fig. 1). More interestingly, they developed cross-links on a structure where individual CNTs were encased in polymer shells which were themselves functionalized with – $NH_2$ and – OH groups before cross-linking.

### 2.2. *Alignment induced strengthening*

Due to the reliance of lamellar structured graphene-based nanocomposites on interaction between the nanocarbons, the degree of compaction and alignment plays an important role in their mechanical performance [35]. Zhong et al. [36] recently introduced the continuous centrifugal casting (CCC) method for increasing the level of alignment and compaction of comprising nanomaterials. The method relies on the application of shear and centrifugal forces on spray-deposited nanomaterials to produce GO, rGO, composite and GO/CNT hybrid films with significantly improved mechanical properties. CCC-prone GO films exhibited a maximum strength of 157 MPa while in-situ chemical reduction further enhanced the mechanical performance of resulting rGO films to ca. 660 MPa through the decrease of inter-lamellar spacing [37,38].

Wan et al. [38] demonstrated a similar near-room-temperature process that used covalent and π-π inter-platelet bridging to freeze the stretch-induced alignment of graphene sheets. Through the featured process, graphene sheets isotropic in-plane microstructure were obtained; hence, displaying tensile strengths exceeding those of the strongest previously described graphene composite [37] and CNT

**Table 1**
Cumulative table of the mechanical properties of the nanocarbon-based films presented in this chapter.

| Materials used | Fabrication method | Strengthening method | UTS (MPa) | Young's modulus (GPa) | Toughness (MJ/m$^3$) | ref |
|---|---|---|---|---|---|---|
| MWCNT | Filtration | cross-linking | 15 | | | Ogino et al. [33] |
| SWCNT | Filtration | epoxy coating/cross-linking | 32 | 3.06 | 0.202 | Jakubinek et al. [34] |
| GO, rGO | spray coating, chemical reduction | continuous centrifugal casting | 157, 660 | | | Zhong et al. [36] |
| GO, rGO | filtration, chemical reduction | UV cross-linking/stretching | 1547 | 64.5 | 35.9 | Wan et al. [38] |
| MWCNT | filtration | cross-linking/1,4-addition polymerization | 150 | 10.18 | | Chen et al. [40] |
| MWCNT/rGO | filtration/chemical reduction | π-π cross-linking | 625 | 54.5 | 28.5 | Wang et al. [42] |
| GO | filtration | covalent cross-linking | 91.9 | 25.5 | | Park et al. [43] |
| GO | filtration | cross-linking/hydrogen bonding | 185 | | | An et al. [45] |
| rGO | filtration | π-π cross linking/1,4-addition polymerization | 944.5 | 15.6 | 20.6 | Wan et al. [46] |
| GO, rGO | filtration/chemical reduction | polymer co-filtration/hydrogen bonding | 188.9 | 10.4 | | Li et al. [47] |
| GO | filtration | void filling via porous GO | 145 | 35.0 | | Mao et al. [54] |

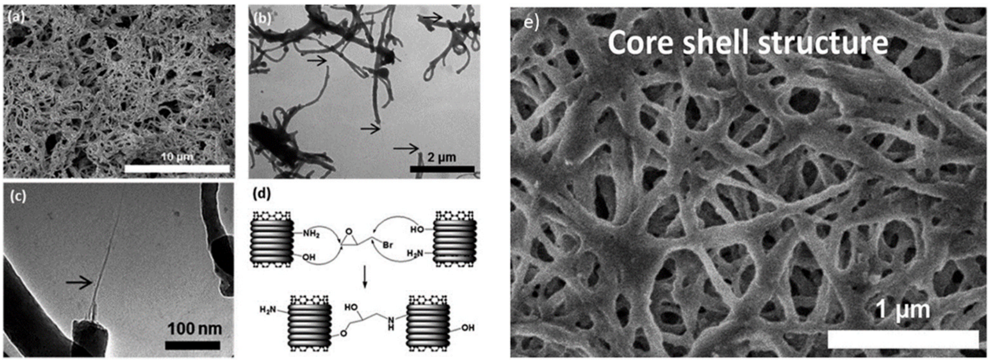

**Fig. 1.** A) SEM image of cross-linked buckypaper b) TEM image of core-shell cross-linked CNTs c) Close-up of previous image showing cross-links. d) Schematic representation of cross-linking reaction mechanism. *Reproduced for ref.* [34]. e) Cross-linked core-shell CNT buckypaper. Despite the polymer shell porosity is maintained allowing further infiltration of use as a membrane. *Reproduced for ref.* [34].

composite [39] by 1.47 and 2.50 times, respectively. Specifically, sequentially bridged (SB) and biaxially stretched (BS) rGO sheets (termed SB-BS-rGO) exhibited a high in-plane tensile strength of 1.55 GPa and a high Young's modulus of ~60 GPa coupled with an electrical conductivity of ~1400S/cm. The fabricated stretch-bridged graphene sheets were scalable by adjustment of casting doctor blade and could be bonded together easily using a commercial resin without appreciable performance degradation.

A notable case of CNT cross-linking was presented by Chen et al. [40], wherein prepared buckypapers were mechanically stretched to increase MWCNT alignment (see Fig. 2). The papers were subsequently treated in nitric acid to achieve –COOH functionalization and immersed in a 10,12-pentacosadyin-1-ol (PCDO) in tetrahydrofuran THF solution. PCDO contains triple bonds at the 10 and 12 positions of the molecule that when irradiated under UV, wavelength of 365 nm, break down and allow the PCDO molecule to undergo a 1,4-addition polymerization reaction with adjacent molecules [41]. Apart from mechanical strengthening due to cross-linking, buckypapers also exhibited enhanced conductivity. This, reportedly, is the combined effect of MWCNT alignment within the sheet and the conjugational nature of the

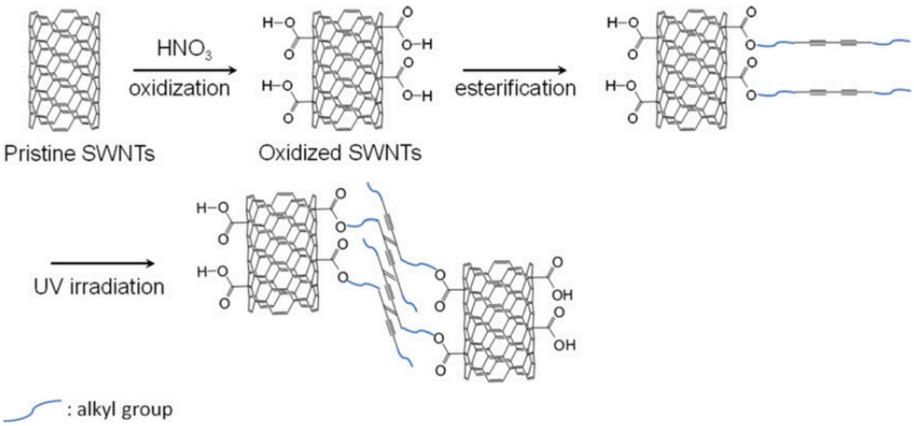

**Fig. 2.** Cross-linking mechanism between functionalized nanotubes. UV-irradiation breaks the triple bonds of the PCDO molecule thus allowing the 1,4-addition reaction between adjacent molecules. *Reproduced from Ref.* [40]. (A colour version of this figure can be viewed online.)

ester bond providing electron paths between cross-linked MWCNTs.

In another recent effort [42], graphene and its hybrids were cross-linked to CNTs using a diamine that was double-edge terminated with 1-pyrenebutyric acid (PBA-diamine-PBA) as a bridging agent. By exploiting the multiple π-π interactions between the fused PBA rings, the graphene nanosheets and CNTs, high-performance nanocarbon-based papers were obtained that exhibited a high tensile strength of 625.2 MPa, high toughness of 28.5 MJ/m$^3$, and an electrical conductivity of 233.4 S/cm. Results were supported by in-situ Raman analysis and simulation calculations demonstrating the effective stress transfer and the reduction of slipping distance between rGO and CNTs during stretching, resulting in the improved mechanical and electrical properties of the composite papers.

### 2.3. *Cross-linking and Nacre-like structure*

Introduction of graphene and GO in polymer matrices for the purpose of endowing the continuous medium with the nanocarbons' exceptional mechanical, electrical and thermal features, is a widely visited research path over the last two decades. Still, dispersion control at higher filler loadings poses great challenges as graphene tends to aggregate and cannot be exfoliated easily. Other than providing a matrix to accommodate the reinforcing graphene, polymers can also strengthen graphene- and GO-based papers through the formation of cross-links between stacked sheets. The fabrication of papers consisting of GO, covalently cross-linked with polyallylamine (PAA), was reported by Park et al. [43]. The authors used dead-end filtration of suspended PAA cross-linked GO flakes to fabricate PAA-GO papers and measure their mechanical properties. A Young's modulus of 33 GPa and an UTS of 91 MPa revealed only small improvement compared to films of un-modified GO. In a similar approach [44], An et al. were inspired by the ability of borate ester to form covalent bonds with the oxygen-containing functional groups of Rhamnogalacturonan II polysaccharides found on high plant cell walls, to produce GO papers of very high stiffness via the simultaneous filtration of GO and varying concentrations of sodium tetraborate [45]. The cross-linked films exhibited an UTS of 160 MPa which was 23% higher than the films that did not contain sodium tetraborate (130 MPa). The results are clearly better than those of Park et al. [43]. Strengthening came with the trade-off of a significant decrease in ductility, with the strain-to-failure lowered to 0.24% from the initial 1.4%.

Wan et al. [46] exploited the covalent cross-linking and π-bond formation to produce graphene papers cross-linked by pentacosadyindioic acid (PCDO) and a compound of 1-pyrenebutyric acid N-hydroxy succinimide ester with 1-aminopyrene (PSE-AP), a small molecule with pyrene functionalities on both edges. Filtration-prone GO sheets were immersed in a PCDO solution in tetrahydrofuran (THF) (same monomer as in Ref. [40] discussed previously), then dried and UV-irradiated. The resultant GO sheets were then reduced and successively immersed in solutions of N-hydroxy succinimide ester (PSE) and 1-aminopyrene (AP) for π-bond formation with rGO planes and covalently bonded between them to form π-bridged rGO flakes. The film showed exceptional values of UTS of 944 MPa and toughness of 20.6 MJ/m$^3$. The method was later retested with another UV-polymerizable molecule, namely bis(1-pyrene methyl)docosa-10,12-diyniodate (BPDD) [37]. Graphene papers formed from the reduction of GO papers were immersed in solutions of the molecule where pyrene functionalities from both edges of the molecules were attached on the basal planes of rGO flakes in the sheet through π-interaction (π-bridging). When irradiated, the triple bonds at 10 and 12 positions of the diacetylene chain break, allowing the 1,4-addition polymerization reaction between BPDD molecules. The resulting sheets exhibit slightly higher values than the reference work, with 1054 MPa and 36 MJ/m$^3$, for UTS and toughness respectively (see Fig. 3).

As far as the synthesis of graphene papers with polymer intermediates is concerned, there is a growing interest in nacre-like hierarchical structures made up from graphene or graphene oxide (GO) [47–49]. Nacre, a calcite mineral-based material found on mollusk shells, is hierarchically structured primary of 95 vol% calcite and 5 vol% biopolymer proteins. The material is twice as strong and three orders of

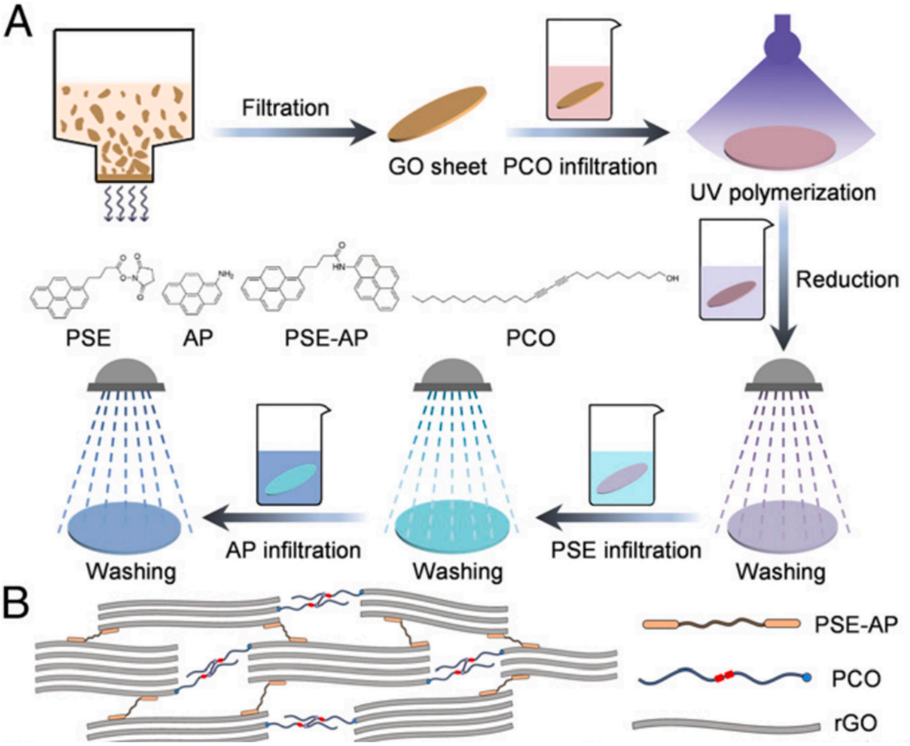

**Fig. 3.** Process for GO sheet fabrication reduction and chemical and π-bridged cross-linking. *Reproduced from Ref.* [37]. (A colour version of this figure can be viewed online.)

magnitude tougher than its otherwise brittle primary constituent [50]. Mimicking the naturally-occurring structure with stronger constituents like graphene (strength of 130 GPa [51]) or GO (strength of ca. 63 GPa depending on defects and density of functional groups [52]) is expected to provide even stronger and tougher hierarchical structures. One straightforward approach to obtain the nacre-like structure, also termed brick-and-mortar structure, was presented by Li et al. Claiming that water-evaporation-induced self-assembly is more scalable than filtration, the authors achieved fabrication of PVA/GO papers and PVA/rGO papers; the latter were the result of reduction of PVA/GO papers in hydroiodic acid (HI) [47]. PVA/rGO exhibited superior mechanical and electrical properties than both GO and PVA/GO papers with tensile strength of 188.9 MPa compared to 118 MPa and 67.1 MPa of PVA/GO and GO papers, respectively. Additionally, pure GO sheets demonstrated a rather low electrical conductivity value of 0.75 S $m^{-1}$ which was further reduced for GO/PVA composites; the corresponding value for PVA/rGO sheets was a favorable 5265 S $m^{-1}$. In both works by An [45] and Li [47], the formation of hydrogen bonds between hydroxyl- and oxygen-containing functionalities aided the formation of alternating lamellae within the sheets, during filtration or deposition, by means of physical adsorption (Fig. 4).

The brick-and-mortar structure can also be achieved by pure GO papers. Mao et al. fabricated GO papers that consisted of GO flakes of varying mechanical properties [54]. They produced the flakes after the modified Hummers' method and induced further chemical "damage" such as pores and greatly reduced rigidity through oxidative etching of the flakes. AFM nano-indentation testing showed a clear difference in mechanical properties between unetched GO flakes and those exposed to 1, 3 and 5h of chemical etching. The authors proposed that mechanical strengthening stems from the insertion of folded chemically etched GO flakes in the spaces left by the more rigid non-etched flakes within the sheet.

Drawing further inspiration from the nacre structure, Peng et al. [55] fabricated composites exhibiting the inverse structure in terms of constituent apportionment, i.e. minimum graphene concentration in a matrix of high volume fraction (Fig. 5). Authors essentially aimed to improve the fracture toughness of the epoxy matrix with graphene, at loadings that inhibited graphene agglomeration phenomena within the matrix. Using bi-directional freeze casting on a blend of GO and carboxymethyl cellulose sodium (CMC), layered ice crystals were formed with GO-CMC sheets in between the layers. After sublimation, an interconnected layered GO-CMC scaffold remained. Annealing at 200 °C yielded an electrically conductive rGO-CMC scaffold at 65% of its initial weight. In the final step a liquid epoxy precursor was infiltrated under vacuum into the scaffold and cured at 130 °C. The resulting composite was made up of 99.27 wt% epoxy and a conductive rGO skeleton which contributed to extrinsic toughening of the matrix via crack deflection and branching mechanisms. The conductive composite scaffold offered the additional functionality of anisotropic conductivity which can be exploited for composite health and crack propagation monitoring.

## 3. Energy storage

### 3.1. Batteries

Having been successfully integrated in a vast multitude of applications that require portable energy sources including military [56], medical [57], telecommunications [58], transportation [59], and renewable energy [60], batteries have evolved to appear in a variety of form factors as well as electrode and electrolyte types [61]. Depending on their reusability, batteries are categorized into primary and secondary – i.e., non-rechargeable and rechargeable, respectively. The single use nature of primary batteries renders them an environmental concern, a fact which lead to a decline in their market share [62]. On the other hand, the ever-increasing popularity of wireless telecommunications and electric vehicles over the last decade has sparked a steady increase in use of secondary batteries [58].

In order to properly curate the various battery systems available, a brief overview of the main terminology is necessary. First, coulombic efficiency (CE) represents the ratio of the charge delivered from a battery over the charge loaded to the battery in a full charge/discharge cycle [63]. CE is affected by thermal loss and non-favorable side reactions during charge/discharge cycles [61,64] and affects battery lifetime [63,65,66]. Specific capacity is the amount of charge stored per unit of mass (mAh/g) of the corresponding electrode [67]. The working voltage is determined from the electrochemical potential difference between the cathode and the anode [67,68] while the property value of a cell depends on the electrolyte and electrode materials used [67,69]. Energy density represents the amount of energy that can be offered from a battery per unit of mass and is determined as the product of the specific capacity and the working voltage of the cell [67,69]. When determining the capacity of a cell, the current density under which the measurements were conducted must be taken into account as higher current density batteries deliver smaller capacities [70]. Current rate (C) quantifies the rate of discharge of a battery relative to its maximum capacity. For example, a rate of 1C is the current rate needed to fully discharge a battery in 1 h. This signifies that for a 100 mAh capacity battery, 0.2C, 0.5C and 2C will represent 20 mA, 50 mA and 200 mA currents, respectively [70].

Modern lithium ion (Li-ion) secondary batteries (also abbreviated as

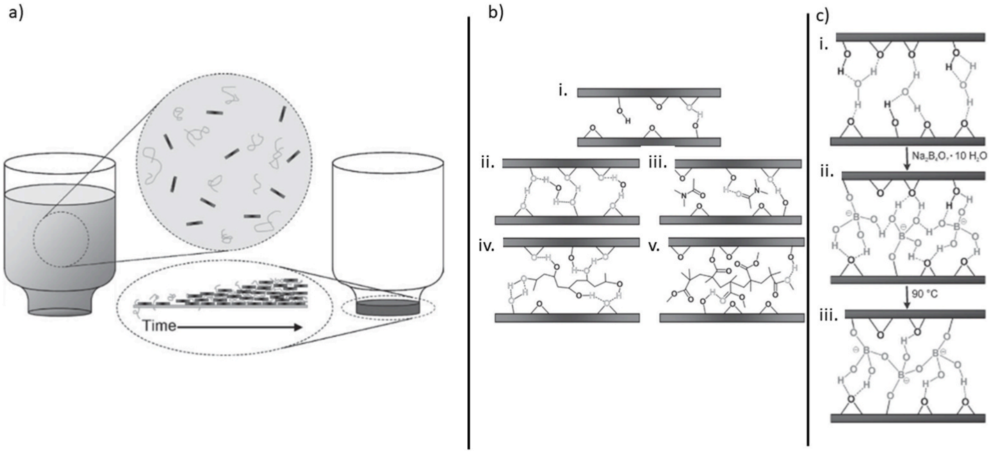

**Fig. 4.** Self-assembly of nacre-like GO sheets during filtration. *Reproduced from Ref.* [53]. b) Hydrogen bonding between i) GO flakes ii) GO flakes and water iii) GO flakes and THF iv) GO flakes and PVA v) GO flakes and PMMA. *Reproduced from Ref.* [53]. c) Hydrogen bonding between sodium tetraborate is replaced by covalent bonding after annealing. *Reproduced from Ref.* [45].

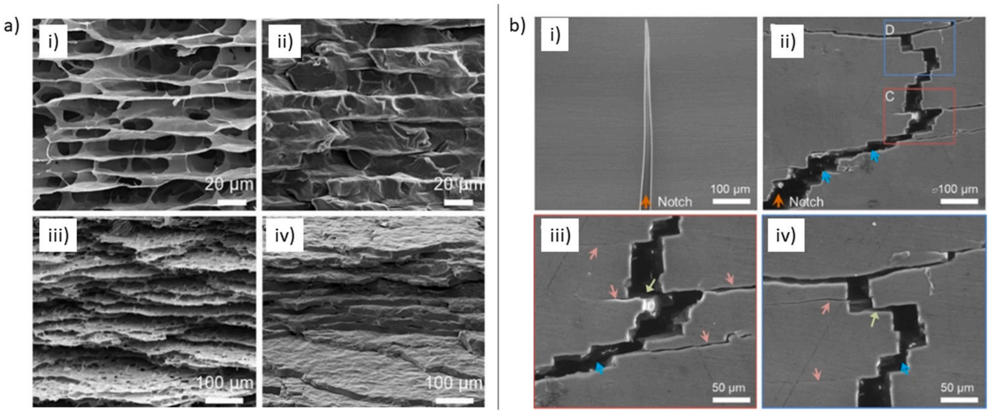

**Fig. 5.** a) SEM pictures of the rGO scaffold i, ii) before and iii, iv) after epoxy infiltration. Reproduced from Ref. [55]. b) SEM pictures of crack propagation in i) pure epoxy and ii, iii, iv) epoxy infiltrated nanocomposites. One can clearly see the crack deflection and crack branching mechanisms at work. Reproduced from Ref. [55]. (A colour version of this figure can be viewed online.)

LIBs) use a graphite anode and $LiCoO_2$ as cathode. When working in liquid electrolyte battery cells, dendritic structures eventually form on the lithium electrode that affect the cell's performance and can also lead to the short circuit of the cell giving rise to safety concerns [71]. Battery life and efficiency of a LIB can be influenced due to solid electrolyte interface growth (SEI) on the electrode and electrolyte interface [67,71,72]. SEI formation takes place on the first charge of the device due to chemical interaction of the anode with the electrolyte and causes an irreversible capacity loss at the first charge/discharge cycle [72]. Although graphite is an abundant material with a layered structure that can allow for reversible intercalation of lithium ions, graphite anodes have a relatively low specific capacity (~370 mAh/g) [73] which is becoming insufficient for modern applications. An alternative to graphite anodes is the use of graphene anodes [74–76].

Graphene has exceptional electrical properties and a large specific surface area (SSA); properties which are important for energy storage applications of both supercapacitor electrodes and battery anodes. Li ion diffusion is much faster in graphene than in graphite due to the smaller energy barrier of graphene edges [77,78], while the material can accommodate such ions on both of sides of the flake during charging [79] hence which reaching higher theoretical capacities. However, when used as an anode, graphene and it's 2D analogues ($MoS_2$, $WS_2$) tend to lack cycle stability due to degradation between discharge/charge cycles caused by intercalating ion species [80,81]. One graphene analogue that has attracted much interest for its use in battery applications is molybdenum disulfide ($MoS_2$), a transition metal dichalcogenide (TMD) that exhibits lithium-ion intercalation capabilities due to its layered structure. Research findings point to the enhanced capacity of $MoS_2$ due to reversible redox reactions that take place between 3.0 V and 0.01 V [64]. Concerns with 2D nanomaterial volume change during lithiation/de-lithiation cycles can be counteracted with the use of polymer binders or the inclusion of carbon nanomaterials like carbon black, rGO [82], CNFs [83] or CNTs [84]. On the other hand, binders can lead to poor interface with active material which allows reaggregation and incorporation of electrochemically inactive mass in the electrode [85]. The CNT network in buckypapers provides a conductive scaffold for the support of the TMD while its porous structure allows better interface with the electrolyte which, in turn, results in increased diffusion of ions. Vacuum filtration of $MoS_2$/CNT inks allows the fast and easy incorporation of $MoS_2$ in a CNT network while ensuring the fabrication of self-standing electrodes [86–88]. Wang et al. [86] demonstrated this effect by comparing the morphology of $MoS_2$/SWCNT and pure $MoS_2$ electrodes after 100 charge/discharge cycles at a current density of 0.1 A/g. Electrochemical measurements were carried out in a CR2032 coin-type battery cell configuration with a Li counter electrode and $LiPF_6$ in ethylene carbonate/dimethyl carbonate solution. Morphological studies via FESEM showed the formation of cracks within the pure $MoS_2$ electrodes, confirming a significant protection against electrode degradation offered by SWCNTs. Patole et al. [89] demonstrated a scalable filtration technique to fabricate large area CNT/graphene sheets (dimensions of A4 size paper) that can be used as anodes in LIBs. When used in such a configuration, the sheets exhibit a theoretical capacity of 744 mAh/g that is nearly double that of graphite.

Another method that proved promising for maintaining the layered structure of 2D materials during charge/discharge cycling, is freeze drying. The process allows for GO dispersions to obtain the sponge-like configuration of aerogels. Shu et al. [90] exploited this strategy to form a free-standing graphene sheet via freeze-drying of a GO hydrogel followed by chemical and thermal reduction process (Fig. 6). The process prevented re-stacking of graphene and allowed formation of a mechanically robust and highly porous graphene paper. When used as a binder-free anode on a lithium battery cell, the resulting sheet exhibited high discharge capacities of 683 and 420 mAh/g, at current densities of 0.2 and 2 A/g, respectively. $MoS_2$/Graphene aerogels are currently fabricated following freeze-drying methods in which molybdate and sulfur precursors and GO are used as starting materials. Specifically, Zhong et al. [91] employed a hydrothermal method where $(NH_4)_2MoS_2$ dissolved in DMF and aqueous GO dispersion were sonicated to form a homogenous solution which was then autoclaved at 200 °C for 12h for the formation of a $MoS_2$/rGO hydrogel. Subsequent freeze-drying and annealing at 700 °C produced a $MoS_2$/rGO aerogel which was used as a binder-free anode in a coin type cell. The electrode showed excellent electrochemical performance of discharge capacity of 1041 mAh/g at a current density of 0.1 A/g current; the performance remained stable within 50 cycles. It should be noted that reference $MoS_2$ electrodes, fabricated via a similar method for comparison, failed to exhibit such cycling stability. Following a similar method, but using $(NH_4)_6Mo_7O_{24}\bullet 4H_2O$ and $CH_4N_2S$ as $MoS_2$ precursors and GO dispersion, Wang et al. [92] fabricated $MoS_2$/GO aerogels via freeze-drying which are then annealed at 750 °C. The aerogels were then used as active materials with binders at coin type cell configurations and exhibited a more modest specific capacity of 742 mAh/g and 480 mAh/g at current densities of 0.1 A/g and 3.0 A/g, respectively.

The growth of $MoS_2$ on GO via solvothermal methods for the fabrication of graphene and $MoS_2$ was achieved earlier this decade, with remarkable electrochemical performance for an anode and the composite as active material [93]. Shan et al. [94] employed a noteworthy method for growing $MoS_2$ nanoparticles within porous rGO papers to create self-standing electrodes which exhibited very high capacitance values. The methodology involved the fabrication of an initial GO film with $(NH_4)_6Mo_7O_{24}$, its subsequent reduction with hydrazine vapor and the in situ solvothermal growth of $MoS_2$ in a thiourea solution. The high

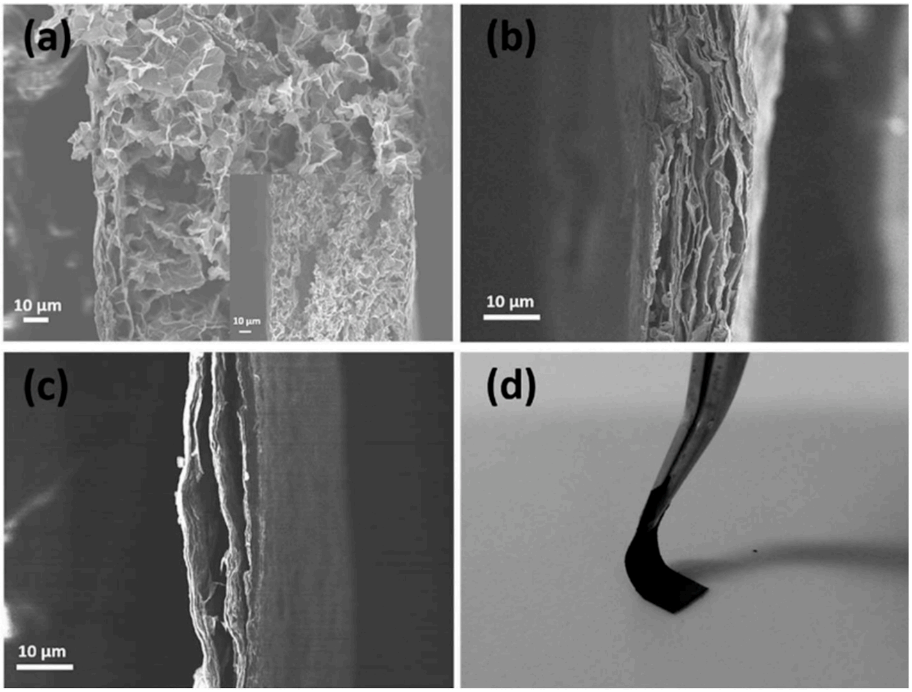

**Fig. 6.** SEM images of graphene sheets fabricated from reduced freeze-dried GO hydrogel. a) Sheet fabricated from water-filled hydrogel (Inset: Same sheet after many cycles of use as electrode) b, c) sheets fabricated from hydrogel that was initially dried in air. d) Macroscopic photograph of flexible sheet. *Reproduced from Ref.* [90].

porosity of the resulting rGO paper was due to the escaping of hydrogen gas during the reduction process. The growth of $MoS_2$ within the pores of the paper led to the development of a hierarchical structure in the electrode material. The electrochemical performance of the self-standing electrode exhibited an astounding capacity value of 1875 mAh/g at 0.1 A/g discharge current. More interestingly, after the electrode was cycled at 5.0 A/g, it exhibited a reversible capacity of 710 mAh/g. This value increased to 1150 mAh/g after the electrode was cycled at 0.1 A/g.

The potential of CNTs to serve as conductive interconnected scaffolds for 2 dimensional nanomaterials has also demonstrated with $MoS_2$ hydrothermally grown on MWCNT networks fabricated by CVD [95,96]. A very interesting structure was achieved by Zhang et al. [97], wherein $MoS_2$ nanostructures were epitaxially formed on CNTs and then coated with amorphous carbon via CVD. The nanomaterial termed CNT@$MoS_2$@C, which constituted the active electrode material, was mixed in an 8:1:1 ratio with acetylene black and carboxymethylcellulose under 24h of magnetic stirring. The resulting slurry was coated on a copper foil and further dried and cut to fit CR2032 coin-type battery cells for electrochemical testing. The electrode exhibited reversible capacities of 982 mAh/g, 905 mAh/g and 707 mAh/g at 0.1 A/g, 1 A/g and 2.5 A/g current densities respectively, combined with excellent rate capability. Also via the hydrothermal method, Pan et al. [98] fabricated $MoS_2$ and graphene nanosheets ($MoS_2$-GNS) and $MoS_2$-CNT-GNS composites. Therein, slurries were prepared from active materials (8:1:1 ratio of composite: acetylene carbon black: PVdF in NMP) which were deposited on Cu foil, dried and used as anodes in a 2032 cell configuration for electrochemical testing. The $MoS_2$-GNS-CNT composite demonstrated better electrochemical performance toward higher current rates, which was attributed to the smaller size and layer count of $MoS_2$ nanoflowers and better electronic conduction with the interconnected CNT support. Highlighted are the capacity values of 870, 703, 619, 524, 461, 434 and 287 mAh/g for respective current densities of 0.5, 1, 2, 5, 8, 10 and 20 A/g. Hydrothermally grown $MoS_2$ on CNT has also been highlighted as binder-free electrode with reversible capacities far exceeding the previous referenced works. Lu et al. [95] use this method to produce MWCNTs grown on current collectors via CVD. The MWCNTs are then treated by $O_2$ plasma to ensure wetting by ammonium tetrathiomolybdate ($(NH_4)_2MoS_4$) solution when placed in an autoclave oven for curing at 200 °C. The electrode exhibited an impressive first charge capacity of 1712 mAh/g and first discharge of 1305 mAh/g at current density of 0.2 A/g, providing the cell with a 76.1% CE at the first cycle.

### 3.2. *Supercapacitors*

A different philosophy in energy storage is offered by electric double layer supercapacitors (EDLCs) which rely on charging and discharging with considerably greater speeds, while storing smaller amounts of charge (energy density) than batteries [99]. Hence, although they exhibit small energy densities compared to batteries, supercapacitors excel in cycling performance and power density [100,101]. Based on the way they store charge, supercapacitors can be divided in electric double layer capacitors (EDLC), pseudocapacitors and hybrid. The main components of an EDLC are the separator, the electrolyte, the electrodes and the current collectors [99]. The way EDLCs store energy is through the formation of an electric double layer (EDL) at the electrode/electrolyte interface which is created by the concentration of cations on the negative electrode and anions on the positive electrodes of the device. Therefore, the larger the available area of the electrode the greater the amount of energy stored on the device. Pseudocapacitance relies on fast and highly reversible surface or near surface redox reactions.

Specific capacitance (SC) values can be calculated either from cyclic voltammetry (CV) or galvanostatic charge-discharge (GCD), through the following equations [102,103]:

$$C = \frac{\int_{V_1}^{V_2} I dV}{vm(V_2 - V_1)} \tag{1}$$

where the integral represents the area under the CV curve, $v$ is the voltage scan rate, $m$ is the mass of the electrode and $V_2$ and $V_1$ are the upper and lower voltage of voltammogram as the ones shown in Fig. 7, respectively, while GCD derived capacitance is calculated as:

$$C=\frac{2I}{m(dv/dt)} \tag{2}$$

where $I$ is the applied current and $dv/dt$ is the slope of the discharge curve of the GCD plot. The energy density is calculated via [99,102,104]:

$$E=\frac{1}{2}CV^2 \tag{3}$$

where $V$ represents the potential window and power density is calculated from Refs. [99,104]:

$$P=\frac{V^2}{4R} \tag{4}$$

where $R$ is the equivalent series resistance.

When researching and designing modern electrodes for EDLC devices, porous materials are preferred as they allow ionic diffusion while offering ample surface [99,106]. Thickness of the electrode plays a major role in supercapacitor performance as thicker electrodes contribute more on the equivalent series resistance of the EDLC and have a negative effect on the rate capability of the device [107]. The above factors necessitate the fabrication of electrodes from conductive materials which can offer high SSA while maintaining small electrode thickness. To this end, buckypapers have manifested a capability as favorable EDLC electrode materials, owing to the conductance of CNTs, their pore distribution that can be narrowly defined in the mesoporous region [32], their moderate SSA values [108,109] and low thickness which can range within 10 μm–~100 μm. Although they generally exhibit a lower SSA than activated carbon (AC), they form mechanically robust structures without the use of binders [99]. Furthermore, their reduced capacitance in aqueous electrolytes due to the hydrophobic nature of CNTs can be enhanced by chemical treatment [104,109]. Moreover, CNTs can offer conductive host scaffolds for accommodation of other nanomaterials which can enhance capacity by SSA increase or development of pseudocapacity [110]. An example of the former is reported by Susantyoko et al. [111] where free-standing MWCNT/AC buckypapers fabricated by doctor-blade coating of copper with a MWCNT/AC dispersion in water and ethanol and subsequent drying in an oven environment, exhibited SC values of up to 135 F/g. The procedure can be also scaled-up to a tape-casting method as demonstrated in the authors' earlier work [112].

Hybrid sheets composed of CNTs and graphene have been reported to exhibit a higher density than AC electrodes (0.7 g/cm$^3$) [113]; this ensures a greater volumetric capacity which is a highly desirable characteristic for many modern devices that require efficient energy storage at small sizes. The effect had independently been shown by Yang et al. [114] who demonstrated the fabrication of dense GO sheets which achieved a high volumetric capacity of 255.5 F/cm$^3$. In their work, they fabricated hydrogel films via filtration of GO and then exchanged the water content with a volatile solvent which was then removed by vacuum evaporation. Diez et al. fabricated a rGO/MWCNT film with apparent densities ranging from 1 to 1.5 g/cm$^3$ through hot pressing of a rGO/MWCNT hydrogel [105]. When compared to rGO films, the rGO/MWCNT counterparts exhibited higher SSAs and a 29% increase in volumetric capacity at a value of 238 F/cm$^3$. The increase was attributed to the ordered structure of MWCNTs between rGO flakes which lead to better electrolyte infusion of the sheet while maintaining a high mass density. For electrodes fabricated with the same technique, Lin et al. [115] showed a 92% and 85% capacitance retention at 32 A/g cycle rates after 250,000 and 450,000 cycles respectively.

Graphene is well known for its high theoretical SSA of ~2675 m$^2$/g and superior mechanical and electrical properties [116]. Electrodes fabricated from graphene are very attractive due to their flexibility and the excellent conductivity of the starting material. However, due to the 2D geometry of graphene, the weak van der Waals forces between individual flakes become so prevalent, that the fabrication of an electrode with a large SSA from pristine graphene is rendered an extremely challenging task. Many researchers have attempted to fabricate graphene films that maintain a porous microscopic morphology via the reduction of GO through hydrothermal and or chemical treatment methods [117,118]. Jiang et al. [119] used filtration to fabricate porous graphene, CNT and rGO composites. Porous graphene was obtained by $MnO_2$ etching [120] while rGO was obtained by thermochemical reduction of GO/CNT suspension. The incorporation of porous graphene in the electrode allowed for better cross-plane ion diffusion. The composite exhibited a relatively high SC of 294 F/g and a high volumetric capacitance of 331 F/cm$^3$. Using filtration and thermal reduction, Lu et al. [121] created binder-free rGO electrodes that incorporated nitrogen-doped porous carbon polyhedrons (NC) which prevented restacking of rGO flakes. The composite exhibited a hierarchical porous structure suitable for EDL storage due to NC nanoparticle presence, while rGO flakes provided a mechanically robust and conductive scaffold with reduced interparticle resistance. The electrode achieved a SC of 280 F/g at 1 A/g, 67% of which was retained at 20 A/g. Additionally, when tested at 5 A/g the supercapacitor exhibited an excellent stability for over 10,000 cycles.

A noteworthy strategy to produce free-standing graphene films which incorporate nanomaterials of different structures or compositions was presented by Wu et al. [122]. A ball milling process was used to initially mix SWCNT, $MoS_2$, Vanadium Nitride (VN) or Silicon Carbide (SiC) nanoparticles with copper nanoparticles (Cu NPs). The resulting mixtures were sintered to produce Cu-based templates for subsequent CVD graphene growth. After the process, Cu was chemically etched and the remaining material was washed successively with HCl and DI water, leaving a hydrogel that maintained the geometry of the original template. Subsequent freeze-drying produced an aerogel of graphene and the nanomaterials incorporated on the original template. GCD testing at

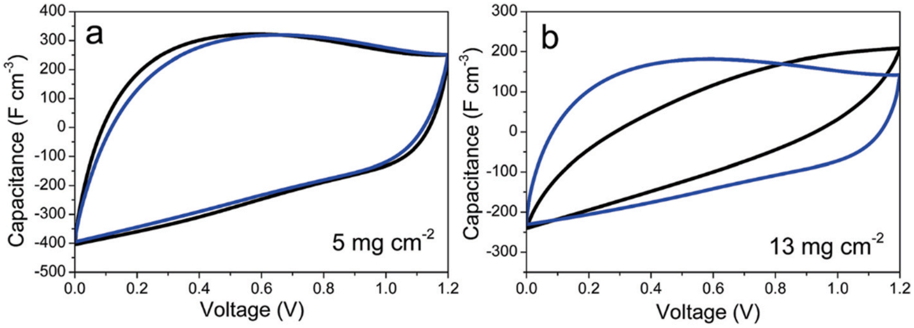

**Fig. 7.** Characteristic cyclic voltammetry curves, for nanocarbon-based supercapacitor electrodes reproduced from Ref. [105]. (A colour version of this figure can be viewed online.)

a relatively low current density rate (0.25 A/g) revealed SC values of 232.4 F/g for the SWCNT-containing electrode and 311.1 F/g for the $MoS_2$-containing one, allowing the authors to attribute the latter value to a pseudocapacitive storage mechanism.

As mentioned earlier, pseudocapacitance employs fast faradaic reactions for charge storage. Although the redox processes have a negative effect on cycle stability, the adversity is balanced out by an increased SC. Conductive polymers have long been regarded as potential materials for pseudocapacitor electrodes due to their fast charging and superior capacitance [99,123]. However, redox reactions during cycling cause degradation of the polymer electrode material [124]. Polymers that are widely used on supercapacitor applications are polypyrrole (PPy) [125], polyaniline (PANI) [126] and poly(3,4-ethylenedioxythiophene) PEDOT [127]. In a recent work, Kim et al. [102] fabricated electrodes based on a ternary composite of silver nanoparticles (Ag NPs), PPy and MWCNTs. The MWCNTs where chemically treated to develop epoxide groups that would form covalent bonds with the pyrrole unit. Meanwhile, Ag NPs that have been shown to enhance electrical performance, have a high affinity to nitrogen atoms and are expected to form co-ordinate bonds with nitrogen-containing pyrrole monomers. At a scan rate of 10 mV $s^{-1}$, the epoxy-functionalized CNT electrode achieved a SC of 349.87 F/g. Calculations from GCD measurements after addition of Ag NPs and of PPy on pristine and on epoxidized MWNCT electrodes, showed a definite capacitance increase in every step of the procedure, with higher values consistently linked with epoxidized MWCNTs. GCD measurements at 0.25 A/g showed a maximum SC of 625 F/g achieved by Ag NP and PPy electrodes on epoxidized MWCNTs.

Applications such as health monitoring and wearable tech require energy storage devices that can work reliably under compression or tension. As already documented, CNTs can offer flexible and conductive porous scaffolds for growth or deposition of conductive polymers which are also lightweight and mechanically robust enough to be used in flexible supercapacitors [128–130]. The concept has also been extended to carbon fiber clothes (CFC), as shown by Rajesh et al. that used the CFC structure as a support for poly(ethylene dioxy-thiophene) (PEDOT) which was polymerized via a solvothermal procedure [131]. Advancing a step further, Liu et al. fabricated a supercapacitor consisting of textile-like CNT/graphene/PANI electrodes and a gel polymer electrolyte [132]. Graphene growth via CVD on a nickel textile was followed by growth of CNT forests and subsequent etching of the Ni substrate. PANI was then electrodeposited on the textile. Graphene/CNT textiles with and without PANI were subsequently immersed in a $H_3PO_4$/PVA gel, dried and pressed together to form a flexible supercapacitor. Results showed a clear increase in areal capacitance with the addition of PANI, with values of 3.1 mF $cm^{-2}$ and 160 mF $cm^{-2}$ achieved for unloaded and PANI-loaded graphene/CNT textiles, respectively. Furthermore, the devices showed a 97% and 90% capacity retention in 120% and 200% tensile strains, respectively.

Nitrogen, a neighbor of carbon in the periodic table of elements, has a similar radius to carbon but contains five electrons in its outer shell. Thus, when inserted in carbonaceous nanomaterials, nitrogen will act as an electron donor. Moreover, pyridinic and pyrrolic N atoms are believed to offer sites for faradaic redox reactions that involve protons [133], making N-doped carbon-based materials attractive for use in pseudocapacitors [134–138]. A straightforward method for fabricating N-doped rGO hydrogels was presented by Gao et al. [139] which involved treatment of a GO and *ortho*-phenylenediamine (*o*-PDA) suspension, in $H_2SO_4$ under hydrothermal conditions. The hydrogels were subsequently freeze-dried to form free-standing electrodes with a SC of 495.4 F/g at 0.5 A/g.

The remarkable flexibility of free-standing nanocarbon-based structures can also be exploited in supercapacitor applications which additionally involve other types of nanomaterials. Wang et al. [140] successfully developed asymmetric flexible supercapacitors that consisted of porous rGO sheets and rGO/$Mn_3O_4$ sheets; these were essentially rGO sheets with $Mn_3O_4$-decorated pores. Not only did both electrode materials exhibited very high SSAs (682 and 368 $m^2$ respectively), but the fabricated supercapacitor also operated without significant performance loss at various bending states. The SC of the device was calculated at 66 F/g, at a current density of 1 A/g, with an 80% capacitance retention at 10 A/g current rate. Testing of the cycle stability of the device at 2 A/g showed an excellent capacitance retention after 3000 cycles. The device was further tested in a bending state of up to 40% of its initial length under 2 A/g and exhibited low capacitance loss even after 200 bending cycles.

## 4. Electromagnetic interference (EMI) shielding

As portable electronic telecommunications and the Internet of Things (IoT) become rooted in modern societies, the problem of electromagnetic interference (EMI) is getting progressively pronounced. Problems caused by EMI, range from damage of electronic components, corruption of scientific measurements, interference of airline communications, to suspected human health risks. In general, EMI shielding efficiency is referred to as the situation where electromagnetic wave dispersion into a desired area is inhibited by a conductive shield. The main mechanisms for diminishing EMI are absorption, reflection, and internal reflections [141,142]. Reflection of EM waves is attributed to their interaction with highly mobile charge carriers, hence basic EMI shielding approaches rely on metallic materials around the targeted device. However, metals are heavy, have high processing costs, exhibit inferior mechanical integrity and are prone to environmental corrosion [143]. Moreover, the high concentration in charge carriers means that shielding from metallic materials is governed by the reflection mechanism [144]. Carbon nanomaterials may exhibit a smaller conductivity than copper, but can form structures that are lighter, thinner, more flexible and more resistant to corrosion. As an added benefit, materials made up of nanocarbons usually offer i) higher conductive area for EM radiation interaction and ii) microstructures that can favor internal reflections, resulting in a longer path length, hence also higher attenuation [145].

Conductivity is not the only parameter responsible for endowing high EMI shielding efficiency. Electric and magnetic dipoles can also provide such efficiency through the absorption mechanism. Materials that display high values of dielectric constant and magnetic permeability are very rich in electric and magnetic dipoles, respectively. These dipoles dissipate energy of impinging EM waves through the absorption mechanism [142], which is strongly related to the thickness of material [141,142,144]. Materials that provide high absorption are those with high dielectric constants, e.g., $SiO_2$, ZnO, $BaTiO_3$ and $TiO_2$, or high magnetic permeability such as Co, Ni, Fe-based alloys, $Fe_3O_4$, and carbonyl iron. However, difficulties related to their processing, low permeability or permittivity in GHz frequencies, narrow band activity and high weight, emerge when these materials are used as shields.

Multiple reflection is the third mechanism controlling EMI shielding efficiency and is correlated to reflections at the interfaces or surfaces of the shield. These are scattering events resulting from the inherent inhomogeneity of the materials; the presence of a large interface area (e.g., porous structures) hence promotes multiple reflections. Suitable materials for achieving EMI shielding efficiency through multiple reflections are composites, foams, foamed composites, honeycomb structures etc. [141,142,146].

The shielding effectiveness (*SE*) is defined as the total attenuation and results from three contributions due to absorption, surface reflection and multiple internal reflections [141,142,144]. *SE* can be described by the logarithmic equation of the ratio of the incident to transmitted fields (E, H, F, (where *E* the electric field, *H* the magnetic field, *F* planar wave field intensities)) [144] and it is expressed in decibels (dB):

It can also be expressed as a function of the logarithmic ratios of the incident to the transmission power, as follows:

$$SE = 20\,log\left(\frac{P_i}{P_t}\right) \tag{5}$$

where $P_i$ in eq. (5) corresponds to the incident power and $P_t$ to the transmitted power. This equation is often used in conjunction with experimental measurements or numerical simulations to characterize the shielding effectiveness of various materials and structures, and to optimize their design for specific applications. Finally, the total *SE* that is provided by a shielding material is the sum of the attenuation due to the reflection ($SE_R$), absorption ($SE_A$) and multiple reflections ($SE_M$) and it is described by the following equation:

$$SE_{total} = SE_R + SE_M + SE_A = -20 \, log \, \mathrm{T}(\omega) \tag{6}$$

### 4.1. GHz Range

Liang et al. [147] were the first who studied the EMI shielding efficiency of graphene-based polymer nanocomposites. By incorporating r-GO at an 8.8% volume fraction in an epoxy matrix, the total shielding effectiveness was measured as 21 dB at a frequency of 8.2 GHz pertaining to the X-band. Zhang et al. [148] investigated the EMI SE of a graphene/PMMA system prepared by solution blending and melt compounding. The produced microcellular graphene/PMMA nanocomposite foam achieved a conductivity of 3.1 *S/m* at a 1.8% graphene volume fraction, exhibiting an *EMI S*E of 13–19 dB in the X-band. The microcellular cells were claimed to not only improve the tensile toughness of the material, but also improve its absorption (i.e. attenuation of reflection).

Similarly, Zhang [149] managed to increase even more the EMI SE of PMMA/GNPs foam with the addition of 8% v/v MWCNTs (up to 36 dB at 8–12 GHz frequencies). The production process for this system was based on solution mixing and bath foaming. In a step further, Sharif et al. [150] produced a hybrid segregated PMMA/r-GO system by incorporation of magnetic nanoparticles at a 0.5% vol. concentration. This led to an increase in the recorded EMI SE from the 20.7 dB–29.3 dB (in 1.1% vol. rGO at 20 GHz frequency). In their system, the electrical percolation threshold was achieved at 0.3% rGO volume fraction and the maximum *SE* was 63.2 dB for a 2.6% vol. r-GO volume fraction.

Batrakov et al. [151] demonstrated achievement of an absorption of 50% of the incident electromagnetic wave in PMMA/CVD graphene stacks at 26.5–40 GHz frequency range. They also briefly presented that a 3-layer stack of PMMA/CVD graphene is capable to shielding 75% of the incident electromagnetic wave at 1 THz. Yan-Jun Wan et al. [35] conducted research on the effect of size of individual GO flakes on the shielding effectiveness of GO sheets. GO flakes formed from the Hummers' method were separated by size by means of centrifugation. The resulting GO sheets were chemically reduced in HI at 90 $^{o}$C, washed with water, dried with ethanol and annealed at 1600 $^{o}$C under inert (Ar gas) atmosphere to produce iodine-doped rGO sheets with improved electrical conductivity. The SE of sheets of a thickness of 21.3 μm, reached ~65.3 dB at the 8.2–12.5 GHz frequency range. Demonstrating the SE of graphene-based structures at low form factors, Shen et al. [152] fabricated graphene sheets through thermal reduction of GO sheets that accomplished a ~20 dB SE at ~8.4 μm thickness. Along with excellent mechanical flexibility and good structural integrity, the sheets also possessed a very high in-plane thermal conductivity (*k*) of ~1100 W/m/K. Furthermore, reduction via thermal annealing of the GO sheets increased the conductivity by 7 orders of magnitude, from reference GO sheet values of $6.0 \times 10^{-4}$ S/cm, to ~1000 S/cm for graphene sheets. When taking into account the SE over thickness ratio and working frequency ranges, the results of the above works were surpassed by the results of Sijie Wan et al., in 2019 [37], wherein at a mere thickness of ~3.4 μm, the cross-linked rGO sheets exhibited a SE of 36.5 dB at the 0.3–18 GHz range along with a 1192 S/cm electrical conductivity and 1054 MPa of strength. Zhou et al. [42] addressed the challenge in designing the interface between adjacent graphene nanosheets to achieve high strength, toughness, and conductivity through the use of a long-chain molecule, 1-pyrenylbutyric acid–linear diamine–1-pyrenylbutyric acid (PBA-diamine-PBA), as a bridging agent between graphene as the matrix and CNTs as the reinforcement. The multiple π-π interactions between the fused rings of PBA, rGO, and CNTs significantly improved the mechanical and electrical properties of the cross-linked composite papers, with the as-obtained graphene-based paper (CLP-6) exhibiting a high tensile strength (625.2 MPa), high fracture energy (28.5 MJ/m$^3$), and high electrical conductivity (233.4 S/cm). The 3.3 μm thick papers exhibited an EMI shielding efficiency of up to 26 dB in the 8–12 GHz range (dominated by absorption) and a SSE/t up to 44,502 dB cm$^2$/g. Tang et al. [153] reported a highly effective electrophoretic deposition process to create a flexible and ultrathin Ti3C2Tx@CNT hybrid buckypaper with exceptional EMI shielding performance. The hybrid buckypaper exhibited EMI SE values of 60.5 dB and 50.4 dB in the X-band at 100 μm and 15 μm thickness, respectively. The average specific SE value of 5.7 × 104 dB cm$^2$/g was observed in the 5-μm hybrid buckypaper. However, no information was provided regarding the mechanical performance of the material. Bin et al. [154] fabricated a new multifunctional natural rubber toughened CNT buckypaper (NR-BP) by vacuum filtration. The NR-BP exhibited excellent mechanical properties compared to the neat buckypaper; The tensile strength was 170% greater, and the fracture strain was 1200% greater. The electrical conductivity of the buckypapers ranged from 21.74 to 34.48 S/cm while the EMI shielding efficiency (EMI SE) was 31.9–28.3 dB in the C-band domain (5.5–8.5 GHz), presenting a specific EMI SE value (SSE/t) at 8504-6232 dB cm$^2$/g. Potential applications of the NR-BP included thermal management and triboelectric nanogenerators (TENGs). Rojas et al. [155] aimed to evaluate the electromagnetic and mechanical properties of glass fiber/epoxy resin composites (GF/EP) incorporating highly porous CNT buckypaper (BP) with serrated and rectangular strip designs. The laminates were analyzed for their electromagnetic interference (EMI) shielding effectiveness (SE) at the 8.2–12.4 GHz (X-band) and 12.4–18 GHz (Ku-band) through electrical permittivity, reflectivity, and attenuation measurements. The results showed that laminates containing 0.75–2.5 wt% MWCNT exhibited a large region promoting electromagnetic wave attenuation up to more than 90% in the frequency range of 8.2–10.8 GHz, showcasing a total EMI SE at ca. 13 dB. The GF/EP/BP/SES laminate exhibited the highest attenuation values of all samples (−41.04 dB at 8.3 GHz), while the GF/EP/BP/RS-CB laminate containing the highest concentration of MWCNTs, 2.5 wt%, showed high values of real and imaginary components of electrical permittivity. Interlaminar shear strength (ILSS), dynamic mechanical analyses (DMA), and impulse excitation technique (IET) tests showed an increase in the GF/EP/BP/SES and GF/EP/BP/SES-CB laminates by 23%, 6% and 16%, respectively; indicating the potential of the GF/EP/BP composites as lightweight, multifunctional, and high-performance EMI shielding materials for electronics and aerospace applications. Choi et al. [156] explored the use of polymer composites as electromagnetic interference (EMI) shielding materials, which are preferred over metals due to their low density and flexibility. However, the conducting pathways within the filler-to-filler contacts inside the polymer matrix often limit their EMI shielding effectiveness (EMI SE). The researchers used a combination of electrospinning, thermal-rolling (at 130 °C), and vacuum filtration to prepare ultrathin and lightweight multiwalled carbon nanotube (MWCNT) buckypaper/electrospun polyacrylonitrile (PAN) nanofiber (BP/NF) composite membranes. They demonstrated that the interfacial network between the BP and NF substrates significantly enhanced the mechanical strength, surface energy, and specific shielding efficiency of the composite membrane. The mechanical strength of the composite membrane was found to be 19 MPa. The 100 μm thick BP/NF-130 membrane showed a 23.3 dB EMI SE and achieved a specific shielding efficiency of 13,734 dB cm$^2$/g, which is superior to most of the previously reported MWCNT/polymer composite membranes. The researchers also explored the effect of nanofiber porosity and structure on the EMI shielding performance of the composite membranes. Overall, the study successfully demonstrated a novel approach for enhancing the EMI shielding performance of polymer composites by improving the interfacial polarization between the MWCNT BP and NF substrates. The results are promising for lightweight, practical, and high-performance EMI shielding applications in a large variety of aerospace, military, smart, wearable, and flexible electronics. Via the vacuum filtration method, Bin et al. [145] prepared multilayer and sandwiched Buckypapers (BP) as electromagnetic interference (EMI) shielding material for X-band frequencies, which achieved an EMI shielding effectiveness (SE) of 31.2 dB and a high specific SE of 19850 dB cm$^2$/g at a thickness of 35 μm. Multilayer and sandwich structures were constructed using BP and polypropylene sheet, with the sandwich structure showing higher SE due to constructive interference between parallel BP layers. Optimum polypropylene sheet thickness was found to be 0.32–0.48λ (λ is the minimum wavelength of the X-band at ca.25 mm), with a resonance peak appearing at d > 0.48λ (d is the thickness of the wave-transmitting layer). The SE of sandwiched structures with one and two wave-transmitting layers increased by 61.5% and 90%, respectively, compared to multilayer structures with the same BP component. The absorption-dominated SE above 100 dB was achieved by adjusting thickness of the shielding layer or the wave-transmitting layer for multilayer structure and sandwich structure. The study has important implications for the development of EMI shielding materials in various applications., and the shielding performance enhancement mechanisms were discussed based on shielding and wave-transmitting layer thickness.

### 4.2. THz Range

The THz frequency domain is considered as the ideal spectrum for fulfilling the continuously increasing demand for faster information transfer. It is foreseen that within the next 10 years, current communication systems will be replaced with THz-based ones [157] providing data transfer rates of up to 5–10 GB/s. To date, development of THz amplifiers and integrated circuits up to 600 GHz have been reported [158]. Hence, with the development of THz devices, it is crucial to produce materials with sufficient EMI shielding performance in that frequency domain [159]. Metal-containing nanocomposites would seem as ideal candidate materials for SE in the THz domain, however they are limited by their weight, environmental sensitivity such as corrosion and lack in processing efficiency.

Carbon-based composites are more appealing since, due to their high conductivity, they present good EMI SE in the THz domain, are facile to fabricate, can be lightweight and cost effective. Okotrub [160] et al. reduced GO buckypapers by chemical and thermal methods and compared their electromagnetic behaviors in the sub-THz range. Chemical reduction proved a more effective route in removing the oxygen groups than thermal reduction. Moreover, they illustrated that the reduction processes create additional favorable defects and vacancies, though affecting the absorption properties in the sub-THz range. Interaction with hydrazine vapor reduced transmittance by 5%, while annealing reduced it by no more than 2%. After 10 min of hydrazine treatment, there were no changes in transmittance due to the limitation of reductant diffusion to the internal GO layers. Accordingly, numerous literature reports focus on the THz-domain EMI SE of carbon-based polymer nanocomposites systems such as CNTs [161], onion-like carbons [159], carbon nano-whiskers [162], and graphene-based nanocomposites [163]. A summary of the most promising studies in the THz

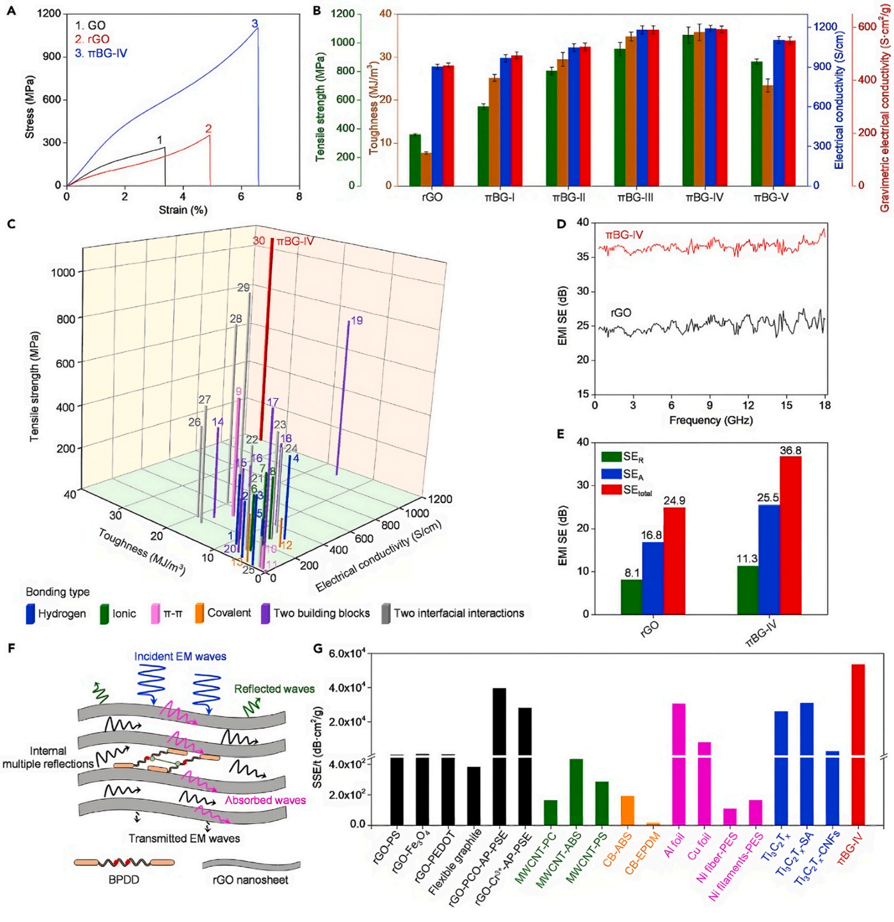

**Fig. 8.** Here, the exceptional mechanical and EMI shielding properties of cross-linked rGO sheets are presented. A,B,C) Summary of sequential increase of the mechanical properties of the sheets following reduction and cross-linking D,E,G) SE of cross-linked sheets F) Model of the EMI reflectance and absorbance mechanisms. *Reproduced from Ref.* [37]. (A colour version of this figure can be viewed online.)

domain is presented in a review article by Megaridis et al. [146] (Fig. 8).

## 5. Thermal management

Powerful contemporary electronic components are fitted in devices with increasingly smaller form factors. Increased core counts and higher clock speeds (calculations per second) require more electrical current which in turn affects the thermal design power (TDP) of a component; some models can reach TDPs of 280W. To avoid catastrophic failure mainly due to localized hotspots causing thermal stresses on a CPU, components are designed with lower clock speeds and limiting mechanisms such as thermal throttling. Two routes are currently pursued for thermal management in electronic components. The first is thermal dissipation, which aims to reduce the temperature difference between hotspots and the rest of the component. Materials with good in-plane $k$ are suitable for such applications. The other is improvement of the thermal interface. Most times, function critical components are connected to heat sinks that are either cooled passively by surrounding air or actively via a fan or a liquid coolant. Thermal interface materials (TIM) are crucial to the conduction of heat from electronics to heat sinks, because air entrapped between any non-flat surfaces of the two components, provides for incomplete contact which renders cooling inefficient [164]. Materials with good cross-plane $k$ would be the best candidates for such applications.

While copper, aluminum, and silver are reliable thermal conductors, graphitic nanomaterials, especially graphene, display superior $k$ (Table 2). The unique atomic structure and high-quality crystalline lattice of graphitic nanomaterials enable efficient heat transfer, which holds promising implications for advanced heat management systems, electronics, and energy storage applications. Continued research and development in the field of graphitic nanomaterials may pave the way for revolutionary advancements in thermal conductivity and energy-efficient technologies.

Graphene, has been reported to exhibit high $k$ in the range of 4800–5300 W/m/K [5] and has attracted scientific interest for heat dissipation applications. Even earlier than the 1D nanocarbon [165] and throughout recent works [166,167], attention was drawn on the thermal properties its 2D counterpart, CNTs, mainly their thermal conductivity in the range of 1000–3500 W/m/K [4]. Graphene and CNT nanofillers have already been researched in composite TIMs [168]. However, due to low thermal conductivity of the polymer matrix and interfacial resistance [169], corresponding values for composites are relatively low [170]. An additional concern are the high temperature ranges that some components work in, that contribute to accelerated aging of polymer matrices [171]. Hence, applicability of free-standing sheets consisting of graphene and CNTs in thermal management applications like electronics packaging [172] still remains a challenge.

### 5.1. High temperature treatment

When GO papers are treated in temperatures high enough, the functional groups containing oxygen decompose [173] while the whole material undergoes a transition to the graphitic state [174]. Thermal annealing combined with certain pre-treatment greatly improves the thermal and electrical properties of the sheets with values for thermal conductivity ($k$) starting from 826 W/m/K [175] and reaching up to 1950 W/m/K [176] with one reported maximum of 3200 W/m/K [177]. Mean phonon free path (MFP) in graphene ranges from 700 to 800 nm [178]. Hence, along with reduction temperature, flake size of GO film prior to reduction is an important factor for thermal performance of its papers. Peng et al. [176] achieved an astounding value for $k$ of 1950 W/m/K; the finding was attributed to the large lateral size of the initial comprising GO flakes – which were separated from smaller flakes to achieve a narrow distribution around an average of 108 μm – and a rather high C/O ratio of 443.1, achieved by thermal treatment at 3000 °C. Chen et al. also researched the effect of high temperature, on rGO films pretreated under pressure, at 300, 1000 and 2000 °C where the, initial GO flake lateral size ranged from 0.1 to 10 μm. After 2000 °C, oxygen disappeared completely and TEM along with XRD and XPS studies indicated restoration of the graphitic basal plane and in-plane thermal conductivity achieved a lower value of 1200 W/m/K.

**Table 2**
Comparison of thermal conductivity values (in W/m/K) for various materials.

| Material | Thermal Conductivity (W/m/K) |
|---|---|
| Copper (Cu) | 400 |
| Aluminum (Al) | 200 |
| Silver (Ag) | 430 |
| Graphene | 3000–5000 |
| Graphene Nanoribbons | Varies up to 5000 |
| Carbon Nanotubes | Varies up to 5000 |
| Single Walled Carbon Nanotubes (SWCNT) | 350–5000 |
| Multi-Walled Carbon Nanotubes (MWCNT) | 10–300 |

Wrinkling affects the thermal conductivity of individual flakes hence also the film's in-plane thermal conductivity [179]. This was show by Lu et al. [180], who prepared hybrid GO/CNT papers with CNT content ranging from 0 to 50 wt%, which were subsequently reduced through thermal treatment. At 15 wt% CNT content, a decrease in the wrinkling of rGO flakes in papers reduced at the relatively lower temperature of 1000 °C, allowed for in-plane K values of 1388 W/m/K.

Akbari et al. showed that film density also appears to affect thermal conductivity [181]. The work demonstrated that introduction of smaller rGO flakes covered the gaps left by the larger flakes in the lateral dimension of the as prepared film hence promoting crystallinity following reduction, pressing and graphitization at 3000 °C. Opto-thermal Raman measurements coupled with finite element analysis provided a high $k$ value of 2025 W/m/K. Wang et al. [177] demonstrated that the films' thermal performance is also affected by film thickness. In that work, 0.8 μm thick films achieved a remarkable 3200 W/m/K which then gradually decreased and leveled off at 2250 W/m/K with increasing film thickness. Another effect of film thickness on thermal properties was demonstrated for films produced by blade-coating [182]. Therein, in GO films prepared by solution-based techniques to thicknesses higher than ca. 100 μm, the laminar stacking of individual flakes in the resulting rGO film begins to break down. Presumably, this effect is related to the amount of water trapped in the middle of the GO film thickness during the thermal pre-treatment and graphitization steps.

### 5.2. Molecular welding

The main carriers for heat in graphene are acoustic phonons [183] hence thermal conductivity in CVD graphene is affected by factors such as the presence of lattice impurities [184–186], flake size [187] and grain size [188]. The scattering of phonons by individual flake boundaries severely deteriorates the rGO papers' thermal performance. Achieving a narrow distribution of large GO flakes is not always a viable option and, as already stated, does not ensure maximum density of graphene within the material. Therefore, researchers have employed macromolecules and various smaller molecules that bridge the edges of graphene flakes and help them fuse together into larger flakes during graphitization. Molecules used so far include polyimide (PI) [189–191], polydopamine (PDA) [192], dehydroascorbic acid (DHA) [193], glucose [194] and polyacrylonitrile (PAN) [195].

### 5.3. Nanocarbons as heating elements

Sheets based on nanocarbons such as graphene and CNTs, possess favorable characteristics for integration into heating applications that rely on the Joule heating effect. In the highly electrically and thermally conductive nanocarbon-based sheets, the effect manifests as prominent heat generation when an electrical current passes through the sheet.

Nanocarbons enable the effective transfer and dissipation of heat generated by the Joule effect due to the synergistic action of high electric conductivity and unique electronic band structure which facilitates efficient movement of charge carriers and rapid phonon transport. However, to their comparatively higher resistance compared to metallic materials, imposes higher electrical potential requirements on nanocarbon-based sheets to generate sufficient heat. Table 3 lists the various nanocarbon-based heater types based on main material used, applied voltage, maximum achieved temperature, heating rate and power draw per unit area.

In nanocarbon-based resistive heating applications, performance indicators include parameters such as temperature increase $\Delta T$, which can be met as a steady-state Temperature ($T_s$), working voltage $V$, power draw and heating rate. Heating power heating, is essentially the amount of heat produced (or the electrical power consumed) has a quadratic dependence to the applied voltage and is directly proportional with the produced current flow as expected from Ohm's equation considerations:

$$P = V^2/R = IV \tag{7}$$

where $I$ is the mean value of direct current measured at each voltage level, $V$. Ideally, for a heating element based on the Joule heating effect, $T_s$ must be achieved as rapidly as possible and the energy balance at a given time $t$ can be expressed by the equation introduced by Sorel et al. [212]:

$$I^2R = mC_p\frac{dT(t)}{dt} + Ah[T(t) - T_0] + \sigma_{SB}A\varepsilon\left[T^4(t) - T_0^4\right] \tag{8}$$

where $m$ is the mass of the material, $C_p$ is its specific heat capacity under constant pressure, $A$ its surface area,h the coefficient of convection, $\sigma_{SB}$ the Stefan – Boltzmann coefficient, $\varepsilon$ the coefficient of emissivity and $T_0$ the ambient temperature which in usual case coincides with the temperature of the film at the Off state of the voltage. The first term on the right-hand side (RHS) of the equation expresses the increase of temperature, the second the heat loss due to convection and the third the radiative heat losses. By applying a Taylor expansion on the latter term, solving the differential equation and inserting the general heat transfer constant (where $a = h + 4\sigma_{SB}A\varepsilon T^3$), the equation for $t_{\rightarrow\infty}$ reduces at:

$$T_{max} - T_0 = \frac{1}{a}\frac{I^2R}{A} \tag{9}$$

Composite resistive heaters exhibit low heating rates or high response times as a trade-off for mechanical robustness [213,214]. The thermal resistance at the nanocarbon/polymer interface and the dielectric nature of the polymer matrix result in accordingly longer electrothermal response times and lower steady-state temperatures ($T_s$) at corresponding values of $V$. This is demonstrated on the composite heating elements studied by Zhou et al. [214], which achieved a steady-state $\Delta T$ of 100 °C at 5 V for $\Delta t$ of the order of ~100 s as well as on the GRM-containing rubber heater by Zhan et al. [213] which required 20 s to reach a plateau of 50 °C at 15 V. Ultrathin-film nanocarbon-based heaters exhibit similarly sub-optimal working parameters while introducing the requirement for a substrate, as a trade-off for transparency [215]. On the other hand, nanocarbon-based paper-like films have relatively low resistance and are expected to exhibit smaller response times for higher $\Delta T$ at smaller voltages. This kind of performance was demonstrated by Guo et al. [216] with rGO papers achieving a $\Delta T$ of 180 °C at 8 V in a few seconds. Wang et al. [206] presented graphene-based fiber (GF) heaters which achieved exceptional properties such as failure strains up to 70%, toughness of 22.45 MJ/m$^3$, electrical conductivity of $6 \times 10^5$ S/m, heating rates of 571 °C/s, and cooling rate of 891 °C/s. The heaters reached temperatures of up to 424 °C at 5V and 220 °C at 3.7 V, demonstrating high electrothermal efficiency. Guo et al. [216] prepared a freestanding graphene paper with high out-of-plane thermal conductivity for wearable personal thermal management. The graphene paper exhibited superior Joule heating features, achieving an extra warmth of 42 °C at a relative low supply voltage of 3.2 V. Additionally, it provided efficient passive cooling by transferring heat from the human body to the environment within 7 s. Compared to normal cotton fabric, the graphene paper demonstrated a superior cooling performance, with a temperature gap reduced from 9.2 °C to 6.5 °C. An independent strategy for enhancing the heating performance of freestanding CNT sheets was proposed from Im et al. [200] by decorating them with granular-type palladium (Pd) particles. The addition of Pd to the CNT sheet increased its heating efficiency by a factor of 3.6, resulting in a heating resistance efficiency of 99.9 °Ccm$^2$/W compared to 27.3 °Ccm$^2$/W without Pd. The improved heating efficiency was attributed to the suppression of convective heat transfer loss and the additional heat generation mechanism provided by the Pd particles. The CNT/Pd sheet demonstrated stable characteristics even after 300 cycles of on-off voltage pulses, with fast heating and cooling rates of 154 and -248 °C/s, respectively. The reduction in electrical resistance of the CNT sheet after Pd deposition further supported the improved performance. These findings highlight the potential of CNT/Pd sheets as high-performance microheaters with applications in various fields. Li et al. [217] prepared polyoxymethylene (POM)/multi-walled MWCNT and POM/graphene nanoplate (GNP) composites (PMCNT and PMGNP) by a new strategy assisted by poly(L-lactide) (PLLA). The composites exhibited uniform dispersion and high contents of MWCNT and GNP. PMCNT40 (40 wt% MWCNT) showed an electromagnetic interference (EMI) shielding effectiveness of 45.7 dB, electrical conductivity of 3484 S/m, and through-plane thermal conductivity of

**Table 3**
The applied voltage, maximum achieved temperature, heating rate and power draw per unit area for various nanocarbon-based sheets.

| Type of Heating element | Material | Applied voltage (V) | $T_s$ (C) | Heating rate (C/s) | Power (W) | Areal Power Density (W/m$^2$) | Ref. |
|---|---|---|---|---|---|---|---|
| laminate-composite | Rgo | 1 | 60 | 1.5 | 1 | N/A | [196] |
| composite | CNT/PVA | 15 | 120 | 11.4 | N/A | N/A | [197] |
| composite | PET/AgNWs/CNTs | 15 | 110 | 3.7 | 0.256 | 160 | [198] |
| composite | PEN/SWCNTS | 7 | 100 | <100 | 0.784 | 3000 | [199] |
| composite-sheet | Pd/CNTs | 5.5 | 105 | 154.0 | 0.188 | 7500 | [200] |
| laminate | Graphene | 8 | 163 | 3.3 | 0.9 | 9500 | [201] |
| composite fiber | CNTs | 40 | 90 | 2.0 | 0.8 | 2000 | [202] |
| films | CNT |  | 400 | 3500.0 | 18 | 300 | [203] |
| sheet | MWCNT/rGO | 8 | 413 | 373 | 6.3 | N/A | [204] |
| Sheet | CNT | 34 | 200 | 3.3 | 5.04 | 840 | [205] |
| fiber | Graphene fibers | 5 | 424 | 571.0 | N/A | N/A | [206] |
| coating | SWCNT | 12 | 140 | 2.3 | 4 | 6400 | [207] |
| coating | MWCNT | 10 | 80 | 4.4 | 0.186 | 350 | [208] |
| coating | RGO | 60 | 206 | 16.0 | 0.4 | 1200 | [209] |
| coating | CNTs | 60 | 160 | 1.3 | n/a | N/A | [210] |
| coating | MWCNT forest | 40 | 140 | 3.5 | 0.26 | 530000 | [211] |
| coating | rGO | 60 | 206 | 16.0 | 5 | N/A | [209] |
| sheet | MWCNT/GRM | 8 | 366 | 355 | 16 | 30792 | [204] |

1.95 W/m/K. Similarly, PMGNP48 (48 wt% GNP) exhibited an EMI shielding effectiveness of 44.7 dB, electrical conductivity of 2695 S/m, and through-plane thermal conductivity of 4.24 W/m/K. Furthermore, the composites exhibited excellent Joule heating performance, with rapid temperature increases at low driving voltages. The surface temperature increased to 101.4 °C and 107.6 °C for PMCNT40 and PMGNP48, at driving voltages of 3.0 V and 6.0 V, respectively. Chang et al. [218] presented the development of a three-dimensional graphene/carbonized-PAN composite freestanding paper intended as an electrothermal heater. It achieved a specific heating rate of up to 213 °C/s/V and a maximum steady-state temperature ($T_s$) of 235 °C at a low driving voltage of 1.75V. The composite paper also retained the intrinsic properties of graphene and allowed for facile and large-scale fabrication, hence suitable for flexible electronics applications. In their study, Shobin and Manivannan [219] focused on the enhancement of electrothermal performance in SWCNT transparent heaters through a room temperature post-treatment process. The researchers fabricated high-performance transparent heaters on glass substrates using a spray coating method with solution-processed SWCNTs. The heaters were then treated with an acid and alcohol mixture to improve their heating performance. The post-treated SWCNT heater exhibited 81% transmittance at 550 nm and reached a steady-state temperature of 150 °C with a heating rate of 0.6 °C/s at an applied voltage of 60 V and an areal power density of 0.035W/cm$^2$. Wang et al. [201] presented the development of a nacre-like styrene-butadiene rubber/crumpled graphene nanosheets heater (NSGH) with superior performance. The NSGH were prepared using the blade-coating technique on a large scale. The NSGH exhibited excellent anisotropic conductivity, flexible stretchable Joule heating performance, and comprehensive mechanical properties. The authors achieved almost constant saturation temperature up to163 °C at 8 V DC voltage and 70% strain with 4000 bends. Abdulkareem et al. [220] employed a graphene-based paper as a potential de-icing material in composite panels. Systems were fabricated using either chemical vapor deposition (CVD) or hot-pressing for the nanocarbon-based paper and vacuum bagging for the glass-fiber composite panel. De-icing was achieved by applying electrical potential to the composite panel to induce the Joule heating effect. Results showed that application of $V_{DC} = 5$ V was sufficient to remove ice from the panel's surface at low power consumptions. When $V_{DC} = 10$ V was applied, the CVD graphene-based paper exhibited higher temperature profiles due to its higher in-plane thermal conductivity compared to hot-pressed graphene-based paper. Su et al. [196] used a nanocarbon-based sheet as heating element by sandwiching it between a top thermochromic layer and a bottom poly (vinylidene fluoride-co-hexafluoropropylene) (PVDF-HFP) substrate. As a result, the thermochromic layer exhibited fast and reversible color conversions of blue-pink-yellow under a low input power (1 W, T = 60 °C). Recently, in order to determine the effects of internal microstructure of nanocarbon based sheets, Kostaras et al. [204] conducted a comparative study of hybrid MWCNT/Graphene based sheets of a wide range of graphene/MWCNT ratios. By comparing the electrothermal performance of hybrid films containing either smaller and thicker graphene nano-platelets (GNPs), thermally reduced GO (trGO) or large chemically reduced GO (crGO), it was demonstrated that the efficiency of the heaters was enhanced by the compaction of the films. It was also found that electrical conductivity was affected by the apparent size of the 2D constituents and their ratios over MWCNTs. The free-standing sheets achieved maximum $\Delta T$ of 366 °C and a heating rate of 355 °C/s.

### 5.4. Joule welding

Joule heating has been also employed to achieve graphitization temperatures on nanocarbon-based sheets without the need of external heating [221,222]. Depending on the initial resistance of the film for a certain voltage, temperatures at the order of 3000 °C can be reached [223,224] while lattice reconstruction takes place. The salability potential of Joule welding was highlighted in the work by Liu et al. [222]. In a device that employed a feed roll and a collection roll at its respective edges and graphite rods at the center, current was driven through a strip of rGO reduced in HI acid and thermally pre-treated. Joule heating at 2433 °C took place in an ultra-dry $H_2$/Ar atmosphere which yielded films with $k = 1285$ W/m/K.

### 5.5. Cross-plane thermal Conductivity

Due to graphene's highly anisotropic thermal conductivity, rGO films are expected to exhibit low cross-plane conductivity values [225]. Wrinkling of rGO papers fabricated by thermal reduction can further affect cross-plane thermal conductivity. This is attributed to gaps between individual flakes that wrinkle during the reduction process. In their work, Hong et al. [226] reported a noticeable increase of cross-plane conductivity for thermally-reduced rGO papers with alumina nanoparticles acting as intersheet gap fillers. The initial GO/alumina films were formed from LbL deposition of GO and alumina layers. CNTs have also been suggested as fillers for intersheet gaps and for improving cross-plane K values [227,228]. Jia et al. [228] demonstrated this effect by producing CNT/rGO hybrid films by combination of chemical reduction, pressing and graphitization at 2800 °C. Similarly Hu et al. [229] combined spinning of CNTs from aligned forests around a mandrel and GO spraying to achieve films of interchanging layers of highly aligned CNTs and GO flakes. After graphitization at 2800 °C, the films of optimized CNT/GO ratios exhibited in-plane thermal conductivity of 1056 W/m/K and cross-plane thermal conductivity of 335 W/m/K. The formation of carbon nanorings (CNR) has been also reported to enhance cross-plane thermal conductivity. By taking advantage of the graphitization of PMMA around Ni nanoparticles, Zhang et al. [230] fabricated CNR-bridged graphene papers by annealing a GO/Ni $(COOH)_2$/PMMA hybrid paper. A reported cross-plane conductivity of 5.8 W/m/K was achieved. More recently, Gao et al. [231] fabricated thick papers of hierarchical structure by the immediate freeze-drying of thick material "cakes" collected during dead-end filtration of large- (12 μm lateral size) and small-sized (2 μm lateral size) graphene flakes. As the cake-like structures were freeze-dried before the total expulsion of water, a vertical orientation of the smaller graphene flakes was achieved. Subsequent graphitization provided a cross-plane conductivity of 12.6 W/m/K.

### 5.6. Electrospray deposition

Xin et al. [232,233] presented a method for fabricating large-scale free-standing graphene papers (GPs) by an electrospraying deposition (ESD) approach integrated with a roller set-up (Fig. 9). Well-dispersed graphene suspensions were sprayed onto Al-foils under a high voltage between nozzle and substrates. Variation of the graphene suspension concentration and of deposition times, controlled the film microstructure of free-standing GPs that were peeled off from the substrate following immersion in water.

### 5.7. Chemical Reduction

Reduction of GO papers can be achieved also by chemical means. While reported reducing agents such as hydrazine cause extensive structural damage due to release of H gas [234], hydroiodic acid has been shown to efficiently reduce GO papers, with the resulting rGO papers maintaining good mechanical properties [216,235,236]. Kumar et al. demonstrated this by comparing the thermal properties of rGO papers of variable flake size, to those of GO papers prior to reduction [235]. Meanwhile, Guo et al. [216] reported the production of graphene papers by reduction of GO papers with vitamin C; they exhibited high values of both in-plane and cross-plane thermal conductivities as paper thickness reached values of 1 μm. Therein, thermal conductivity was shown to be inversely proportional to sheet thickness with cross-plane and in-plane values of 490 ± 50 W/m/K and 730 ± 50 W/m/K,

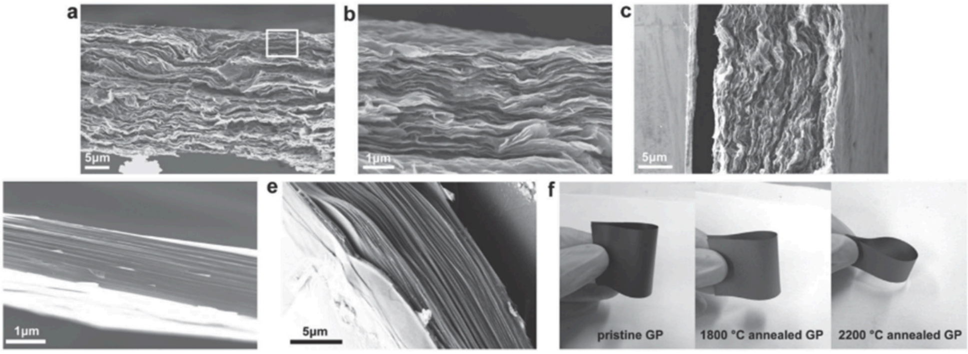

**Fig. 9.** a, b, c) SEM images of graphene sheets deposited on Al with ESD d, e) SEM images of annealed samples in high temperatures f) Photograph of graphene papers before and after annealing. *Reproduced from Ref.* [232].

respectively, for sheet thickness of 8 μm and 2100 ± 50 W/m/K and 2600 ± 50 W/m/K, respectively, for 1 μm sheet thickness. Emphasis on the effect of rGO paper microstructure on the thermal and electrical conductivities was given by Yang et al. [237]. They demonstrated both types of conductivities can be regulated by the ratio of smaller GO flakes in the papers before the reduction process. While papers consisting of larger flakes offered longer paths for carrier propagation due to the smaller number of edges, rGO papers that were fabricated from GO papers containing 50% of smaller flakes showed maximum thermal and electrical conductivities of 1102 W $m^{-1}$ $K^{-1}$ and 8982 S $m^{-1}$, respectively. This indicated that the compaction offered by smaller flakes filling the voids between larger ones, plays a significant role in conductivity. Table 4 summarizes the properties of thermally conductive nanocarbon-based sheets, as function of mean flake size L of GO used to create the initial films, the thermal reduction method employed, reduction temperature *Tr*, C/O ratio after the reduction process, in-plane and cross-plane thermal conductivities, *k//* and $k^{\perp}$ respectively, and the characterization method.

## 6. Membrane separation

The superior performance of nanocarbon-based membranes in separation processes is underpinned by their advanced physical properties and the mechanisms that govern their function. Key properties include the high surface area, which provides ample space for molecular interactions, and the ability to tailor pore size for specific separation tasks. The mechanical strength and flexibility of these materials ensure durability under various operational conditions, while their chemical and thermal stability make them suitable for a wide range of applications. The main mechanism for achieving gas separation is kinetic diameter exclusion for porous membranes and diffusion when considering dense membranes [239]. Concerning water separation, the primary mechanisms include size exclusion, where molecules larger than the membrane's pore size are mechanically blocked, and selective adsorption, where specific molecules are preferentially adsorbed due to the unique surface characteristics of the nanocarbon material. Charge-based separation and hydrophilicity also play crucial roles, where these properties facilitate the efficient removal of contaminants and the passage of clean water. These nanocarbon-based membranes exhibit remarkable properties such as high mechanical strength, chemical stability, and unique transport characteristics, making nanocarbon-based sheets highly effective in separation processes.

### 6.1. Applications in gas separation

One of the critical applications of nanocarbon-based membranes is in gas separation. The intrinsic porosity and tunable interlayer spacing of graphene sheets, for instance, enable selective permeation of specific gas molecules. This selectivity is crucial for applications like carbon dioxide capture from industrial emissions and the purification of natural gas. Graphene oxide membranes, with their laminar structures and functional groups, can be engineered to allow the fast passage of small gas molecules like hydrogen while effectively blocking larger molecules such as nitrogen or methane [240]. Climate-change has expedited the need for efficient capture of greenhouse gases, such as $CO_2$. GO-based membranes have been tested for such an application due to their permselective function of $CO_2$ over other gases. This was recently investigated by molecular dynamics studies [241] that showed GO membranes with varying pore sizes displaying permselectivity between $N_2$ and $CO_2$ gases. The authors proposed that $N_2$ molecules are more

**Table 4**
Cumulative table outlining the properties of thermally conductive nanocarbon-based sheets, where reported.

| *L* (μm) | Reduction method | $T_r$ (°C) | C/O ratio | $k_{//}$(W/m/K) | $k_{\perp}$ (W/m/K) | Characterization Method | Ref. |
|---|---|---|---|---|---|---|---|
| 105 | Heating/Press | 3000 | 443.1 | 1940 | – | IR imaging | [176] |
| 0.1–10 | Press/Heating | 2000/2750 | – | 1200 | – | Laser flash | [174] |
| <2 | Chemical/Press/Heating | 1000/2800 | 95.62 | 933.4 | 6.27 | Laser flash | [228] |
| | Heating | 1000 | 93.62 | 1389 | – | Laser flash/DSC | [180] |
| 35–45 | Heating/Press | 2800 | – | 1224 | – | Laser flash | [182] |
| 2–7 | Chemical/Heating/Press | 3000 | – | 2025 | – | Raman/Finite Element Analysis | [181] |
| – | Chemical/Heating | 800 | 23.66 | 1032 | – | Laser flash | [193] |
| – | Press/Heating | 2800 | – | 802.3 | – | Laser flash | [189] |
| – | Microwave/Heating/Chemical | 2800 | – | 1352 | – | Laser flash | [191] |
| – | Chemical/Heating | RT/3000 | – | 1584 | – | Laser flash | [192] |
| – | Hydrothermal/Pressing | 180/100 | – | 836.8 | 0.058 | Laser flash | [227] |
| 50–100 | Pressing/Heating | 800/2800 | – | 1053 | – | Laser flash | [190] |
| – | Heating/Graphitization | 1000/ | – | 1331 | – | Laser flash/DSC | [194] |
| 1–50 | – | – | 81 | 1428 | 150 | Laser flash | [238] |
| >6 μm | Chemical/Pressing/Heating | 2850 | >1000 | 3200 | 14 | DRT/ITB/PPR | [177] |
| 15–20 | Chemical/Thermal/Joule | 300/2433 | 50.4 | 1285 | | HR IR imaging | [222] |
| | Heating | 250/2800 | – | 1056 | 335 | Laser flash/DSC | [229] |

likely to adopt a direct pathway through the membrane pores than $CO_2$ molecules that preferentially diffuse on the graphitic layers of GO. This effect is experimentally demonstrated by the work of Zhou et al. [242], where selective permeation of H, He and $N_2$ gases over $CO_2$ was achieved using lamellar GO/amine membranes fabricated by the scalable method of Layer-by-Layer (LbL) ink-jet printing on polymeric supports. Specifically, apart from kinetic diameter exclusion, $CO_2$ retention was enhanced by the addition of layers consisting of $CO_2$-philic amine molecules. Enhancement of $CO_2$ retention was also achieved by Widakdo et al. [243] on GO-based membranes that employed melamine molecules as cross-linking agents between GO flakes. Similar to the work by Zhou et al. [242] the amine-based cross-linkers enhanced $CO_2$ adsorption and by extension displayed increased $CO_2/O_2$ and $CO_2/N_2$ selectivities for increased melamine contents.

Similarly, CNT membranes, known for their smooth inner surfaces and uniform pore sizes, provide an ideal pathway for the rapid transport of gas molecules, offering high permeability and selectivity in gas separation processes [244,245]. The random networks developed within CNT-based membranes give rise to pores following size distributions of variable width. The width of the pore size distributions relies primarily on the length and diameter of the CNTs [246] and on the process used to chemically modify the outer surfaces of the particles [19,23]. The high porosity of such membranes allows high gas permeability. On the other hand, selectivity is important in gas separation applications. To this end, Li et al. [247] studied the increase of the selectivity of CNT membranes by the incorporation of poly (amic acid) (PAA). The subsequent pyrolytic treatment of CNT/PAA membranes led to the development of carbon/CNT hybrid membranes that displayed enhanced selectivity of $CO_2$ over methane ($CH_4$) (two molecules with similar kinetic diameters [248]).

### 6.2. Desalination and wastewater reprocess

One of the main concerns in the on-going environmental crisis is the depletion of natural fresh water sources, which comes as a result of urban overpopulation, increased irrigation for crops, usage for food production [249] and industrial processes [250,251] and contamination from pharmaceuticals close to inhabited areas [252]. Scientific interest for water treatment and separation techniques for reducing fresh water contamination and converting sea or brackish water to potable, has known a tremendous increase during the last decades. Water purification can be achieved through a variety of approaches such as adsorption [253] or flocculation and sedimentation [254] of contaminants, while desalination is achieved through phase-change [255] and separation processes. Membrane separation is a process in which a semipermeable barrier is used to retain certain molecules between two liquid phases. The retention of molecules depends on a variety of characteristics including molecular diameter, charge and solubility [256]. Separation processes are in general less energy demanding than thermal ones [257–259] and show versatility concerning the salinity of the source water and the type of compounds retained (see Table 4 above).

Table 5 contains a description of the various water treatment methods used in literature.

**Table 5**
Brief overview of water separation methods.

| Separation Method | Description |
|---|---|
| Distillation | Separates water from impurities by boiling and condensation based on the differences in boiling points. |
| Reverse Osmosis | Uses a semi-permeable membrane to separate water from dissolved solids and contaminants by applying pressure. |
| Forward Osmosis | Uses a semi-permeable membrane to extract water from a feed solution into a more concentrated draw solution through osmosis. |
| Ion Exchange | Involves the exchange of ions between a solid resin and water to remove dissolved salts and other ions. |
| Filtration | Passes water through a physical barrier (e.g., sand, activated carbon, or membranes) to remove impurities. |
| Pervaporation | Utilizes a membrane to separate water from volatile components in a liquid mixture based on differences in vapor pressure. |
| Electrocoagulation | Uses an electric current to destabilize and aggregate suspended particles and colloids for removal |
| Flocculation | Adds chemicals (flocculants) to water to create larger particles (flocs) that can be easily removed by sedimentation or filtration |
| Biological Treatment | Utilizes microorganisms to break down and remove organic compounds and pollutants through biological processes. |
| Adsorption (AD) | Uses adsorbents (e.g., activated carbon) to attract and remove contaminants from water through surface interactions. |

### 6.3. Reverse osmosis (RO) and Nanofiltration (NF)

Reverse osmosis, a process employed for crossflow filtration, is the most popular separation process for desalination. Over the last five decades, RO has gained popularity owing to the process' potential to effectively desalinate a wide range of water types, ranging from brackish to sea water [260,261], with smaller energy burdens than phase-change processes [257,262]. However, RO use still carries an impact on the environment due to the electric energy needed to create hydraulic pressure for the feed water [262] and also due to the nature of the concentrate produced which has higher salinity than the source water and contains the contaminants of the purification process [263,264]. For RO, a thin film composite (TFC) is typically used as membrane, which employs a thin active layer (commonly polyamide (PA) [265], poly (vinyl pyrrolidone) (PVP) [266] or polyimide [267]) on a microporous polymer substrate. This kind of membrane is easily damaged from chlorine or sodium hypochlorite (NaClO) which is used to inhibit bio-fouling during water treatment [268–271].

Although widely used for their low cost, Cl-based cleaning solutions are responsible for presence of hypochlorous acid (HClO) [272,273], a substance which reacts with PA membranes through a variety of mechanisms [272], to affect their salt rejection performance. Nanocarbons exhibit a free radical scavenging mechanism that contains electron-transfer processes [274,275] and adduct formation [276]. GO also exhibits free radical absorbing capabilities [277] together with an excellent affinity to water due to the presence of oxygenated functional groups [278]. Over the course of the last decade researchers have focused on using GO either as an additive in the active layer [277, 279–281] or as thin film on top of the active layer [282–284] to counteract the issues of sensitivity to chemicals and increased fouling that plagued membranes for RO. Stacked GO flakes can form a thin membrane that allows for water flux between layers and is held together through hydrogen bonding between the hydroxyl and carboxyl groups present [285]. Ion sieving is achieved through size exclusion [286], electrostatic interaction [287] and ion adsorption effects [286]. Acting either as nanofiller or as over-layer, GO has been shown to reduce the surface roughness [282,288] and enhance the hydrophilicity of PA active layers [289]; the two main factors known to affect membrane fouling [290]. Furthermore, GO has been reported to imbue the layer with antimicrobial properties [288,291].

Parallel to RO, nanofiltration (NF) has also been extensively researched for water separation. Although commercial NF membranes are, similarly to RO membranes, formed through phase inversion, they present some key differences. First, along with size exclusion, electrostatic (Donnan exclusion) and dielectric effects play a role to separation by NF [292]. Secondly, NF membranes operate in lower pressures (2–5 bars) than those used for RO (seawater: 55–65 bar, brackish water: 10–30 bar) [293], a fact which renders them attractive for use as assistive systems to RO-based processes [294,295]. The most interesting difference of NF to RO is the selective rejection of divalent over monovalent salts [296] while still presenting a molecular weight cut-off (MWCO) of 300–500 Da. The latter property comes of use to the textile industry where it is common for inorganic salts to be used as dye pickup enhancers for textiles [297]. The fractionation of dye/salt mixtures is necessary as high salinity of used water hinders either the biodegradation of organic dyes by microorganisms or the reuse of dying agents [298].

Along with size and charge selectivity [299], stacked GO membranes also exhibit higher rejections of divalent and multivalent ions over monovalent ions [299,300], highlighting the membranes' usefulness in NF applications like water softening [301] and dye/salt mixture fractionation [298].

GO films have been documented to exhibit the undesirable tendency to swell under contact with water, resulting in an increase of water flux and a decrease of salt rejection [302]. Moreover, as interlayer distance is determined by the electrostatic interactions between the functionalities of GO [303], the property can be affected by the pH level or ion concentration in the feed solution [304,305]. The effect has been shown to be modulated by feed water pressure [306,307]. Accordingly, significant research effort has focused on ensuring the stability of the distance between comprising flakes through covalent cross-linking using either urea [308], *meta*-phenylenediamine (MPD) [309] or various dicarboxylic acids [310]. Diamines have been used extensively for the formation of cross-links between individual GO lamellae. The size of the cross-linking molecule controls the interlamellar distances and hence the flux and rejection performance of the corresponding membrane [309,311–313]. Covalent crosslinking has also been suggested for stabilization of GO stacked films over the active layer of the membrane [314,315].

Another way to remedy the swelling of GO membranes in water is through partial reduction. For this task, rGO/$TiO_2$ and rGO/$TiO_2$/CS membranes have been developed via photoreduction of corresponding membranes consisting either of GO and $TiO_2$ flakes or GO, $TiO_2$ flake and chitosan [316]. The operating principle of desalination using nanoporous graphene and the water transport/salt rejection mechanism in rGO membranes through nanoslits, nanopores and nanochannels are shown in Fig. 10.

### 6.4. Forward osmosis (FO)

Contrary to RO and NF, forward osmosis (FO) does not rely on the use of pumps for pushing the feed solution through the membrane, but the movement rather relies on the osmotic pressure caused by a draw solution of greater salinity than that of the feed solution [319]. This means that FO not only provides an energetically less demanding approach to desalination, but it can also be used in an auxiliary manner by using the concentrate from RO processes as a draw solution and thus reducing the operation costs of RO plants [320]. Additionally, the organic fouling layer that accumulates on FO membranes over time, is much more loosely adhered and thus easier to remove. This is because, in contrast to RO, which relies on hydraulic pressure that contributes to the formation of a compact fouling layer that reduces permeate flux, FO relies on an osmotic pressure gradient to drive the separation and is more sensitive to concentration polarization effects than the primer [319,321]. For an asymmetric membrane – one that employs separate active and supporting layers – to operate in FO mode, the active layer must face the feed solution. External concentration polarization (ECP) is developed due to the accumulation of solute on the side of the membrane of the feed solution causing its concentration to be higher than that in the draw solution. Thus, the differential osmotic pressure and solvent flow are decreased. Internal concentration polarization (ICP) appears within the supporting layer on asymmetric membranes and is affected by the thickness $t$, porosity $\varepsilon$ and tortuosity $\tau$ of the layer as described by the parameter $S$ [319,322].

$$S = \frac{t\tau}{\varepsilon} \tag{10}$$

While ECP can be easily counteracted by changing the flow conditions, ICP cannot be easily minimized as it occurs within the supporting layer [319,322]. Hence, efficient desalination by FO membranes requires simultaneous satisfaction of the conditions of hydrophilicity for reduction ECP, small thickness of the active layer for increased flux, high selectivity and minimal thickness of supporting layer for low $S$ parameter values.

Stacked GO membranes are an attractive choice for FO and pressure-retarded osmosis (PRO) as they offer a very thin and selective structure that is hydrophilic, highly permeable to water and with rejection efficiency controlled by thickness. However, interlayer spacing increases when membranes are wet, especially in the presence of $Na^+$, which leads to decreased salt rejection. Stabilization of interlayer spacing through cross-linking of GO flakes that comprise the membrane has been also employed in the case of FO processes [309,323,324]. To that end, LbL deposition of GO and various molecules has been suggested [325,326]; the added benefit of the method is the ability to control the membranes' rejection performance through adjustment of the number of deposited layers.

Another route to weaken the effect of certain ions to the interlayer spacing of GO membranes is their partial reduction. Loss of negatively charged oxygen functionalities entails that the comprising flakes will have a reduced interaction with ions wherein, along with the beneficial increased stability of rGO membranes, water flux is facilitated due to reduction of water side-pinning effects [327]. When in contact with HI vapors or after thermal treatment, GO membranes will be partially reduced with a definite increase of contact angle [327–330]. Partially reduced membranes have been examined as free-standing FO membranes [328,329] or as a stable interlayer between pDA active layer and support layer [330]. The absence of a supporting layer, as shown by Yan et al. [329], was connected to increased water permeation performance through non-supported membranes. Insufficient water flux was attributed to ICP effects that hinder the development of high osmotic pressure difference between the feed and draw sides of the supported membrane.

### 6.5. Pervaporation

Water-alcohol separation processes are important for the environment because they simultaneously ensure the conservation of clean water and the recycling of alcohols which are produced at the costs of

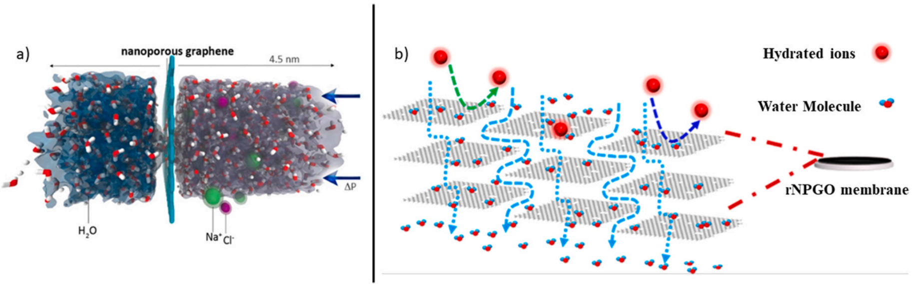

**Fig. 10.** a) Schematic representing desalination using nanoporous graphene (reproduced from Ref. [317]). b) Water transport and salt rejection mechanism in rGO membranes through nanoslits, nanopores and nanochannels (reproduced from Ref. [318]). (A colour version of this figure can be viewed online.)

energy and natural resources. Alcohol/water mixtures turn azeotropic at certain water molar fractions where mixture vapors contain the same water fractions as the liquid phase [331]. This renders complete dehydration of alcohols via distillation practically impossible. Pervaporation (PV) is a membrane process for separating liquids by employing a selectively permeable (permselective) filter to separate the permeate in vapor form from a feed solution preheated below the boiling point and pressurized over its bubble point [332]. As new hydrophilic materials emerge for use in separation technologies, PV processes are also being introduced as valid options for desalination [333]. Water adsorbed on the feed solution diffuses within the membrane where the liquid-to-vapor phase change takes place and is desorbed in vapor form at the permeate side leaving behind up to 99.9% of dissolved salts [332].

The hydrophilicity and favorable water diffusion mechanism of water through stacked GO membranes highlight them as excellent candidate materials for PV. Moreover, GO displays a preferential interaction with water over alcohols [278] and various organic solvents [334]. GO membranes deposited via filtration on polyacrylonitrile substrates were shown to produce 99.5 wt% water permeate from a 70 wt% IPA/water mixture at a relatively low temperature of 70 °C [331]. Subsequent research on alcohol and water mixtures provided exceptional water purities on the permeate side of the membrane [335–337].

## 7. Catalysis

The role of nanocarbon-based materials, particularly graphene and carbon nanotubes (CNTs), has become increasingly significant in the field of catalysis. These materials, characterized by their unique structural and chemical properties, offer new avenues for catalytic applications [338]. This section delves into how nanocarbon-based sheets are utilized as catalysts and catalyst supports, highlighting their high surface area, electrical conductivity, and specific surface functionalities.

The exceptional electrical conductivity, alongside a high surface area make graphene an ideal candidate for catalytic applications, particularly in electrocatalysis [339]. Graphene's conductivity facilitates electron transfer, enhancing the efficiency of electrocatalytic reactions [340]. Its large surface area allows for a higher density of catalytic sites, improving reaction rates [341]. For example, graphene has been employed as a support material for metal nanoparticles in fuel cell reactions. The metal nanoparticles, dispersed on the graphene sheet, benefit from enhanced electron transfer, improving the overall efficiency of the fuel cell [342]. Xuning Li et al. [343]. provided compelling evidence of graphene's exceptional qualities for catalytic applications, specifically showcased in the development of an efficient Fenton-like catalyst. In this catalyst design, the high surface area is utilized to anchor single cobalt atoms and to create dual reaction sites on porous nitrogen-doped graphene. This configuration significantly improves reaction rates, as seen in the efficient degradation of organic contaminants. In their effort it is highlighted not only the graphene's potential in electrocatalysis but also its practical application in environmental remediation, affirming the text's assertion of graphene's suitability for catalytic uses.

Similarly, carbon nanotubes, with their cylindrical nanostructure and remarkable electrical properties, have found significant applications in catalysis. Their unique structure enables efficient electron transfer, which is crucial in various catalytic processes [344]. CNTs have been used as supports for metal catalysts in reactions such as hydrogenation and oxidation [345]. In catalysis, hydrogenation and oxidation are key processes. Hydrogenation involves the addition of hydrogen ($H_2$) to compounds, using metal catalysts (e.g. palladium or platinum) to convert unsaturated bonds (double or triple) into saturated (single) bonds. Conversely, oxidation involves adding oxygen or removing hydrogen, often catalyzed by metal oxides, changing the oxidation state of molecules. The high surface area of CNTs allows for the dispersion of a large number of metal nanoparticles, thereby increasing the active sites available for catalysis [345]. Additionally, the strong interaction between the metal nanoparticles and CNTs prevents the leaching of the catalyst, enhancing the stability and reusability of the catalytic system. Yi Cheng et al. [346] effectively illustrates the critical role of carbon nanotubes (CNTs) in catalysis, aligning well with the established understanding of CNTs' properties and applications. CNTs, with their unique cylindrical nanostructure and remarkable electrical properties, are utilized as a support for metal catalysts, specifically single-atom catalysts like nickel (Ni) and cobalt (Co). This study showcases how the efficient electron transfer capability of CNTs, a consequence of their distinctive structure, is crucial in catalytic processes, particularly in the electrochemical reduction of $CO_2$. The high surface area of the nitrogen-doped CNTs (N-CNTs) used in this research allows for an ultrahigh dispersion of these metal atoms, significantly increasing the number of active sites available for catalysis. This dispersion is instrumental in achieving the remarkably high metal loading (up to 20 wt% for Ni), which is a notable advancement in the field. Moreover, the strong interaction between the metal nanoparticles and the CNTs, highlighted in the study, prevents the leaching of the catalyst. This aspect enhances the stability and reusability of the catalytic system, addressing a common challenge in catalyst design. A highlighted research that effectively demonstrates how the cylindrical nanostructure and electrical properties of CNTs contribute in catalysis, particularly in reactions such as hydrogenation and oxidation is being presented by Chen et al. [347]. They demonstrated the catalytic prowess of CNTs in electrocatalytic ammonia synthesis. Utilizing CNTs as supports for iron nanoparticles, the study achieved a remarkable ammonia formation rate of $2.2 \times 10^{-3}$ g $NH_3$ $m^{-2}$ $h^{-1}$ at room temperature and atmospheric pressure. The high surface area of CNTs allowed for efficient dispersion of iron nanoparticles, increasing active catalytic sites. This setup enhanced electron transfer efficiency, as evidenced by a high total Faraday efficiency of 95.1%. The strong interaction between the metal nanoparticles and CNTs enhanced the catalyst's stability and selectivity, preventing leaching and improving reusability.

Moreover, the surface chemistry of nanocarbon materials can be modified to introduce functional groups, which further enhances their catalytic properties. For instance, the introduction of oxygen-containing groups in graphene oxide improves its hydrophilicity, which is beneficial in aqueous-phase reactions. Similarly, doping CNTs with heteroatoms like nitrogen or boron can modify their electronic properties, making them suitable for specific catalytic reactions [345]. For example, Kang et al. demonstrated the impactful role of heteroatom doping in modifying the electronic properties of CNTs. Nitrogen doping of CNTs, combined with the encapsulation of Ni–Co alloy nanoparticles, creates a synergistic effect that significantly enhances both the catalytic activity and stability of the CNTs. This modification led to a notably fast reaction rate of 0.31 $min^{-1}$ in the catalytic activation of peroxymonosulfate for the degradation of ibuprofen [348]. Recent advancements in the field have also seen the development of hybrid structures combining graphene and CNTs, which leverage the benefits of both materials [349]. These hybrids exhibit enhanced electrical conductivity and a larger surface area, making them highly effective as catalyst supports. Such hybrid structures have been explored in various environmental applications, including water treatment and air purification, where they aid in the breakdown of pollutants through catalytic reactions [350]. In the research presented by Zamani et al. [351] by applying ammonia treatment, the study tunes the nitrogen incorporation into these nanocarbons, enhancing their catalytic activity. The resulting catalyst features a robust morphology of porous, 2-D graphene-like structures intermixed with 1-D CNTs, enriched with nitrogen and iron species. This unique surface chemistry yields impressive results, achieving a half-wave potential of 0.81 V, a current density of 77 mA $cm^2$ at 0.8 V, and a maximum power density of 335 mW $cm^2$ in H2-air fuel cell testing. The study of Pongpichayakul et al. [352] on platinum-loaded reduced graphene oxide (rGO) and carbon nanotube (CNT) composites for methanol oxidation reaction highlights their exceptional properties in catalysis. rGO offers superior electrical and thermal conductivity, large surface area, and mechanical strength, while CNTs provide high conductivity and adsorption capacity, enhancing catalyst stability and efficiency. These combined properties make rGO and CNTs excellent support materials for electrochemical applications, particularly in methanol oxidation reactions.

In regard of water treatment applications, nanocarbon-based catalysts are employed to degrade organic pollutants, remove heavy metals, and even for disinfection purposes. Graphene and its derivatives, with their large surface area, act as excellent platforms for photocatalytic reactions [353]. When doped with metals or metal oxides, graphene-based catalysts can efficiently generate reactive oxygen species under light irradiation, which can break down organic pollutants in water into less harmful substances [354,355]. This photocatalytic process is particularly effective in degrading persistent organic pollutants, such as pharmaceuticals and personal care products, which are typically resistant to conventional water treatment methods [356]. Carbon nanotubes also play a significant role in water purification. Their hollow and porous structure makes them ideal for adsorbing heavy metals and organic contaminants. Functionalized CNTs, where the surface is modified with specific chemical groups, can target and remove specific pollutants from water [357]. For example, CNTs functionalized with amino groups have shown high efficiency in capturing and removing heavy metals like lead and mercury from contaminated water [358]. In the current review there is an extended section below in regard to the water treatment using various nanocarbons as materials.

In summary, the unique properties of nanocarbon-based sheets, such as high surface area, excellent conductivity, and tunable surface chemistry, make them ideal candidates for catalytic applications. Their use in supporting metal nanoparticles, coupled with the ability to modify their surface properties, opens up new possibilities in various catalytic processes. The ongoing research and development in this area promise further innovations, potentially leading to more efficient and sustainable catalytic systems in the future.

## 8. Conclusion

Although mass production and commercialization of pristine graphene are not yet mature, the importance of graphitic nanomaterials and especially graphene in modern technological applications is already apparent. The fabrication of sheets based on nanocarbons such as CNTs and graphene and its derivatives, through techniques like cross-linking and alignment-induced strengthening, has overcome processing challenges and demonstrated their unique multifaceted performance. These sheets find applications in diverse fields such as water treatment, energy storage, electromagnetic interference (EMI) shielding and thermal management, where they offer valuable assets such as ion selectivity, chlorine resistance, solvent separation capabilities, increased energy capacity and excellent electrical conductivity. Furthermore, graphitic nanomaterials, including graphene and CNTs, exhibit superior thermal conductivity compared to traditional materials, hence emerging as promising candidates for thermal management in electronic components. Water treatment for desalination purposes has gained significant interest, with reverse osmosis and nanofiltration currently highlighted as promising strategies. GO· is highlighted as an auspicious material for RO membrane applications, addressing issues of sensitivity to chemicals, fouling, and antimicrobial properties, while stacked GO membranes show advantages in forward osmosis and pervaporation processes. Moreover, the fabrication of high-capacity electrodes for electrochemical energy storage devices, such as batteries with excellent rate capabilities and supercapacitors, can greatly benefit of nanocarbon-based porous materials such as buckypapers of graphene and CNTs which emerge as ideal candidate materials for supercapacitor electrodes and flexible structures for wearable devices. It is apparent that the unique properties of graphene and its derivatives and carbon nanotubes (CNTs) as well, particularly in terms of high surface area and electronic properties, play a crucial role in catalytic mechanisms. These nanocarbons enhance technologies in electrocatalysis and environmental remediation by facilitating improved electron transfer and offering a high density of active sites, which are essential for advanced catalytic reactions. These advancements in nanocarbon-based sheets, electrode materials, graphitic nanomaterials, catalysis, and water treatment technologies collectively hold great promise for a wide range of practical applications, addressing challenges in the major current concerns of our environment and lives, namely water, energy and thermal management, which pave the way for sustainable and efficient solutions for the planet.

## CRediT authorship contribution statement

**Christos Kostaras:** Data curation, Investigation, Methodology, Writing – original draft, Writing – review & editing. **Christos Pavlou:** Data curation, Investigation, Methodology, Writing – original draft. **Costas Galiotis:** Methodology, Supervision, Validation. **Konstantinos G. Dassios:** Methodology, Resources, Supervision, Visualization, Writing – original draft, Writing – review & editing.

## Declaration of competing interest

The authors declare that they have no known competing financial interests or personal relationships that could have appeared to influence the work reported in this paper.

## Data availability

The authors are unable or have chosen not to specify which data has been used.

## References

[1] S. Iijima, Helical microtubules of graphitic carbon, Nature 354 (1991) 56–58, https://doi.org/10.1038/354056a0.
[2] K.S. Novoselov, Electric field effect in Atomically thin carbon films, Science 306 (2004) 666–669, https://doi.org/10.1126/science.1102896.
[3] K. Shirasu, G. Yamamoto, T. Hashida, How do the mechanical properties of carbon nanotubes increase? An experimental evaluation and modeling of the engineering tensile strength of individual carbon nanotubes, Mater. Res. Express 6 (2019), https://doi.org/10.1088/2053-1591/ab069f.
[4] E. Pop, D. Mann, Q. Wang, K. Goodson, H. Dai, Thermal conductance of an individual single-wall carbon nanotube above room temperature, Nano Lett. 6 (2006) 96–100, https://doi.org/10.1021/nl052145f.
[5] A.A. Balandin, S. Ghosh, W. Bao, I. Calizo, D. Teweldebrhan, F. Miao, C.N. Lau, Superior thermal conductivity of single-layer graphene, Nano Lett. 8 (2008) 902–907, https://doi.org/10.1021/nl0731872.
[6] Z. Hu, X. Lu, Mechanical properties of carbon nanotubes and graphene, in: Carbon Nanotubes and Graphene, second ed., Elsevier, 2014, pp. 165–200, https://doi.org/10.1016/B978-0-08-098232-8.00008-5.
[7] Z. Spitalsky, D. Tasis, K. Papagelis, C. Galiotis, Carbon nanotube–polymer composites: chemistry, processing, mechanical and electrical properties, Prog. Polym. Sci. 35 (2010) 357–401, https://doi.org/10.1016/j.progpolymsci.2009.09.003.
[8] A.A. Balandin, Thermal properties of graphene and nanostructured carbon materials, Nat. Mater. 10 (2011) 569–581, https://doi.org/10.1038/nmat3064.
[9] A.A. Balandin, S. Ghosh, W. Bao, I. Calizo, D. Teweldebrhan, F. Miao, C.N. Lau, Superior thermal conductivity of single-layer graphene, Nano Lett. 8 (2008) 902–907, https://doi.org/10.1021/nl0731872.
[10] C.N.R. Rao, A.K. Sood, K.S. Subrahmanyam, A. Govindaraj, Graphene: the new two-dimensional nanomaterial, Angew. Chem. Int. Ed. 48 (2009) 7752–7777, https://doi.org/10.1002/anie.200901678.
[11] V. Palermo, I.A. Kinloch, S. Ligi, N.M. Pugno, Nanoscale Mechanics of graphene and graphene oxide in composites: a scientific and technological perspective, Adv. Mater. 28 (2016) 6232–6238, https://doi.org/10.1002/adma.201505469.
[12] W. Gao, L.B. Alemany, L. Ci, P.M. Ajayan, New insights into the structure and reduction of graphite oxide, Nat. Chem. 1 (2009) 403–408, https://doi.org/10.1038/nchem.281.
[13] D.R. Dreyer, S. Park, C.W. Bielawski, R.S. Ruoff, The chemistry of graphene oxide, Chem. Soc. Rev. 39 (2009) 228–240, https://doi.org/10.1039/B917103G.
[14] A.C. Ferrari, F. Bonaccorso, V. Fal'ko, K.S. Novoselov, S. Roche, P. Bøggild, S. Borini, F.H.L. Koppens, V. Palermo, N. Pugno, J.A. Garrido, R. Sordan, A. Bianco, L. Ballerini, M. Prato, E. Lidorikis, J. Kivioja, C. Marinelli, T. Ryhänen, A. Morpurgo, J.N. Coleman, V. Nicolosi, L. Colombo, A. Fert, M. Garcia-Hernandez, A. Bachtold, G.F. Schneider, F. Guinea, C. Dekker, M. Barbone, Z. Sun, C. Galiotis, A.N. Grigorenko, G. Konstantatos, A. Kis, M. Katsnelson,

L. Vandersypen, A. Loiseau, V. Morandi, D. Neumaier, E. Treossi, V. Pellegrini, M. Polini, A. Tredicucci, G.M. Williams, B.H. Hong, J.-H. Ahn, J.M. Kim, H. Zirath, B.J. van Wees, H. van der Zant, L. Occhipinti, A.D. Matteo, I.A. Kinloch, T. Seyller, E. Quesnel, X. Feng, K. Teo, N. Rupesinghe, P. Hakonen, S.R.T. Neil, Q. Tannock, T. Löfwander, J. Kinaret, Science and technology roadmap for graphene, related two-dimensional crystals, and hybrid systems, Nanoscale 7 (2015) 4598–4810, https://doi.org/10.1039/C4NR01600A.

[15] F. Perrozzi, S. Croce, E. Treossi, V. Palermo, S. Santucci, G. Fioravanti, L. Ottaviano, Reduction dependent wetting properties of graphene oxide, Carbon 77 (2014) 473–480, https://doi.org/10.1016/j.carbon.2014.05.052.

[16] H. Shioyama, Polymerization of isoprene and styrene in the interlayer spacing of graphite, Carbon 35 (1997) 1664–1665, https://doi.org/10.1016/S0008-6223(97)82797-2.

[17] M.A. Gervasoni Nasar Ali, William I. Milne, Cengiz S. Ozkan, in: Stanislaw Mitura, L. Juana (Eds.), Graphene Science Handbook: Mechanical and Chemical Properties, CRC Press, Boca Raton, 2016, https://doi.org/10.1201/b19674.

[18] MdH.-O. Rashid, S.F. Ralph, Carbon nanotube membranes: synthesis, properties, and future filtration applications, Nanomaterials 7 (2017) 99, https://doi.org/10.3390/nano7050099.

[19] G. Trakakis, D. Tasis, J. Parthenios, C. Galiotis, K. Papagelis, Structural properties of chemically functionalized carbon nanotube thin films, Materials 6 (2013) 2360–2371, https://doi.org/10.3390/ma6062360.

[20] B. Natarajan, Processing-structure-mechanical property relationships in direct formed carbon nanotube articles and their composites: a review, Compos. Sci. Technol. 225 (2022) 109501, https://doi.org/10.1016/j.compscitech.2022.109501.

[21] X. Zhang, D. Yang, H. Li, W. Yang, S. Qu, W. Lu, Ultrasonic assisted stretching approach toward aligned CNT for high strength and conductive nanocomposite, Compos. Commun. 35 (2022) 101335, https://doi.org/10.1016/j.coco.2022.101335.

[22] Q.Q. Shi, H. Zhan, R.W. Mo, J.N. Wang, High-strength and toughness carbon nanotube fiber/resin composites by controllable wet-stretching and stepped pressing, Carbon 189 (2022) 1–9, https://doi.org/10.1016/j.carbon.2021.12.034.

[23] G. Trakakis, D. Tasis, C. Aggelopoulos, J. Parthenios, C. Galiotis, K. Papagelis, Open structured in comparison with dense multi-walled carbon nanotube buckypapers and their composites, Compos. Sci. Technol. 77 (2013) 52–59, https://doi.org/10.1016/j.compscitech.2013.01.003.

[24] G. Trakakis, G. Anagnostopoulos, L. Sygellou, A. Bakolas, J. Parthenios, D. Tasis, C. Galiotis, K. Papagelis, Epoxidized multi-walled carbon nanotube buckypapers: a scaffold for polymer nanocomposites with enhanced mechanical properties, Chem. Eng. J. 281 (2015) 793–803, https://doi.org/10.1016/j.cej.2015.06.085.

[25] G. Trakakis, G. Tomara, V. Datsyuk, L. Sygellou, A. Bakolas, D. Tasis, J. Parthenios, C. Krontiras, S. Georga, C. Galiotis, K. Papagelis, Mechanical, electrical, and thermal properties of carbon nanotube buckypapers/epoxy nanocomposites produced by oxidized and epoxidized nanotubes, Materials 13 (2020) 1–20, https://doi.org/10.3390/ma13194308.

[26] J. Huang, X. Yang, S.C. Her, Y.M. Liang, Carbon nanotube/graphene nanoplatelet hybrid film as a flexible multifunctional sensor, Sensors 19 (2019), https://doi.org/10.3390/s19020317.

[27] A.A. Iurchenkova, E.O. Fedorovskaya, I.P. Asanov, V.E. Arkhipov, K.M. Popov, K. I. Baskakova, A.V. Okotrub, MWCNT buckypaper/polypyrrole nanocomposites for supercapasitor application, Electrochim. Acta 335 (2020) 135700, https://doi.org/10.1016/j.electacta.2020.135700.

[28] MdH.-O. Rashid, G. Triani, N. Scales, M. in het Panhuis, L.D. Nghiem, S.F. Ralph, Nanofiltration applications of tough MWNT buckypaper membranes containing biopolymers, J. Mem. Sci. 529 (2017) 23–34, https://doi.org/10.1016/j.memsci.2017.01.040.

[29] Z. Zeng, C. Wang, G. Siqueira, D. Han, A. Huch, S. Abdolhosseinzadeh, J. Heier, F. Nüesch, C. (John), Zhang, G. Nyström, Nanocellulose-MXene Biomimetic aerogels with orientation-tunable electromagnetic interference shielding performance, Adv. Sci. 7 (2020) 2000979, https://doi.org/10.1002/advs.202000979.

[30] J. Liu, M.-Y. Yu, Z.-Z. Yu, V. Nicolosi, Design and advanced manufacturing of electromagnetic interference shielding materials, Mater. Today 66 (2023) 245–272, https://doi.org/10.1016/j.mattod.2023.03.022.

[31] X. Zhu, K. Yang, B. Chen, Membranes prepared from graphene-based nanomaterials for sustainable applications: a review, Environ. Sci.: Nano 4 (2017) 2267–2285, https://doi.org/10.1039/C7EN00548B.

[32] V. Datsyuk, M. Kalyva, K. Papagelis, J. Parthenios, D. Tasis, A. Siokou, I. Kallitsis, C. Galiotis, Chemical oxidation of multiwalled carbon nanotubes, Carbon 46 (2008) 833–840, https://doi.org/10.1016/j.carbon.2008.02.012.

[33] S. Ogino, Y. Sato, G. Yamamoto, K. Sasamori, H. Kimura, T. Hashida, K. Motomiya, B. Jeyadevan, K. Tohji, Relation of the number of cross-links and mechanical properties of multi-walled carbon nanotube films formed by a dehydration condensation reaction, J. Phys. Chem. B 110 (2006) 23159–23163, https://doi.org/10.1021/jp0642387.

[34] M.B. Jakubinek, B. Ashrafi, J. Guan, M.B. Johnson, M.A. White, B. Simard, 3D chemically cross-linked single-walled carbon nanotube buckypapers, RSC Adv. 4 (2014) 57564–57573, https://doi.org/10.1039/c4ra12026d.

[35] Y.-J. Wan, P.-L. Zhu, S.-H. Yu, R. Sun, C.-P. Wong, W.-H. Liao, Graphene paper for exceptional EMI shielding performance using large-sized graphene oxide sheets and doping strategy, Carbon 122 (2017) 74–81, https://doi.org/10.1016/j.carbon.2017.06.042.

[36] J. Zhong, W. Sun, Q. Wei, X. Qian, H.-M. Cheng, W. Ren, Efficient and scalable synthesis of highly aligned and compact two-dimensional nanosheet films with record performances, Nat. Commun. 9 (2018) 3484, https://doi.org/10.1038/s41467-018-05723-2.

[37] S. Wan, Y. Chen, Y. Wang, G. Li, G. Wang, L. Liu, J. Zhang, Y. Liu, Z. Xu, A. P. Tomsia, L. Jiang, Q. Cheng, Ultrastrong graphene films via long-chain π-bridging, Matter 1 (2019) 389–401, https://doi.org/10.1016/j.matt.2019.04.006.

[38] S. Wan, Y. Chen, S. Fang, S. Wang, Z. Xu, L. Jiang, R.H. Baughman, Q. Cheng, High-strength scalable graphene sheets by freezing stretch-induced alignment, Nat. Mater. 20 (2021) 624–631, https://doi.org/10.1038/s41563-020-00892-2.

[39] Q. Cheng, J. Bao, J.G. Park, Z. Liang, C. Zhang, B. Wang, High mechanical performance composite conductor: multi-walled carbon nanotube sheet/bismaleimide nanocomposites, Adv. Funct. Mater. 19 (2009) 3219–3225, https://doi.org/10.1002/adfm.200900663.

[40] I.-W.W. Peter Chen, R. Liang, H. Zhao, B. Wang, C. Zhang, Highly conductive carbon nanotube buckypapers with improved doping stability via conjugational cross-linking, Nanotechnology 22 (2011) 485708, https://doi.org/10.1088/0957-4484/22/48/485708.

[41] D. Takajo, A. Inaba, K. Sudoh, Two-dimensional solid-state topochemical reactions of 10,12-pentacosadiyn- 1-ol adsorbed on graphite, Langmuir 30 (2014) 2738–2744, https://doi.org/10.1021/la4049314.

[42] Y. Wang, F. Meng, F. Huang, Y. Li, X. Tian, Y. Mei, Z. Zhou, Ultrastrong carbon nanotubes/graphene papers via multiple π–π cross-linking, ACS Appl. Mater. Interfaces 12 (2020) 47811–47819, https://doi.org/10.1021/acsami.0c12501.

[43] S. Park, D.A. Dikin, S.T. Nguyen, R.S. Ruoff, Graphene oxide sheets chemically cross-linked by polyallylamine, J. Phys. Chem. C 113 (2009) 15801–15804, https://doi.org/10.1021/jp907613s.

[44] M.A. O'Neill, D. Warrenfeltz, K. Kates, P. Pellerin, T. Doco, A.G. Darvill, P. Albersheim, Rhamnogalacturonan-II, a pectic polysaccharide in the walls of growing plant cell, forms a dimer that is covalently cross-linked by a borate ester. In vitro conditions for the formation and hydrolysis of the dimer, J. Biol. Chem. 271 (1996) 22923–22930, https://doi.org/10.1074/jbc.271.37.22923.

[45] Z. An, O.C. Compton, K.W. Putz, L.C. Brinson, S.T. Nguyen, Bio-inspired borate cross-linking in ultra-stiff graphene oxide thin films, Adv. Mater. 23 (2011) 3842–3846, https://doi.org/10.1002/adma.201101544.

[46] S. Wan, Y. Li, J. Mu, A.E. Aliev, S. Fang, N.A. Kotov, L. Jiang, Q. Cheng, R. H. Baughman, Sequentially bridged graphene sheets with high strength, toughness, and electrical conductivity, Proc. Natl. Acad. Sci. USA 115 (2018) 5359–5364, https://doi.org/10.1073/pnas.1719111115.

[47] Y.-Q. Li, T. Yu, T.-Y. Yang, L.-X. Zheng, K. Liao, Bio-inspired nacre-like composite films based on graphene with superior mechanical, electrical, and Biocompatible properties, Adv. Mater. 24 (2012) 3426–3431, https://doi.org/10.1002/adma.201200452.

[48] O.C. Compton, S.W. Cranford, K.W. Putz, Z. An, L.C. Brinson, M.J. Buehler, S. T. Nguyen, Tuning the mechanical properties of graphene oxide paper and its associated polymer nanocomposites by controlling Cooperative intersheet hydrogen bonding, ACS Nano 6 (2012) 2008–2019, https://doi.org/10.1021/nn202928w.

[49] C.T. Chen, F.J. Martin-Martinez, S. Ling, Z. Qin, M.J. Buehler, Nacre-inspired design of graphene oxide–polydopamine nanocomposites for enhanced mechanical properties and multi-functionalities, Nano Futures 1 (2017), https://doi.org/10.1088/2399-1984/aa6aed.

[50] X. Li, W.C. Chang, Y.J. Chao, R. Wang, M. Chang, Nanoscale structural and mechanical characterization of a natural nanocomposite material: the shell of red abalone, Nano Lett. 4 (2004) 613–617, https://doi.org/10.1021/nl049962k.

[51] C. Lee, X. Wei, J.W. Kysar, J. Hone, Measurement of the Elastic properties and intrinsic strength of Monolayer graphene, Science 321 (2008) 385–388, https://doi.org/10.1126/science.1157996.

[52] J.T. Paci, T. Belytschko, G.C. Schatz, Computational studies of the structure, behavior upon heating and mechanical properties of graphite oxide, J. Phys. Chem. C 111 (2007) 18099–18111, https://doi.org/10.1021/jp075799g.

[53] K.W. Putz, O.C. Compton, M.J. Palmeri, S.B.T. Nguyen, L.C. Brinson, High-nanofiller-content graphene oxide-polymer nanocomposites via vacuum-assisted self-assembly, Adv. Funct. Mater. 20 (2010) 3322–3329, https://doi.org/10.1002/adfm.201000723.

[54] L. Mao, H. Park, R.A. Soler-Crespo, H.D. Espinosa, T.H. Han, S.T. Nguyen, J. Huang, Stiffening of graphene oxide films by soft porous sheets, Nat. Commun. 10 (2019) 4–10, https://doi.org/10.1038/s41467-019-11609-8.

[55] J. Peng, C. Huang, C. Cao, E. Saiz, Y. Du, S. Dou, A.P. Tomsia, H.D. Wagner, L. Jiang, Q. Cheng, Inverse nacre-like epoxy-graphene layered nanocomposites with integration of high toughness and self-monitoring, Matter (2019) 1–13, https://doi.org/10.1016/j.matt.2019.08.013.

[56] A. Yezeguelian, A.T. Isikveren, Methods to Improve UAV Performance Using Hybrid-Electric Architectures, Aircraft Engineering and Aerospace Technology, 2020, https://doi.org/10.1108/AEAT-11-2019-0227.

[57] David C. Bock, Amy C. Marschilok, Kenneth J. Takeuchi, Esther S. Takeuchi, Batteries used to power Implantable Biomedical devices, Electrochim. Acta 84 (2012) 155–164, https://doi.org/10.1016/j.electacta.2012.03.057.

[58] Y. Liang, C. Zhao, H. Yuan, Y. Chen, W. Zhang, J. Huang, D. Yu, Y. Liu, M. Titirici, Y. Chueh, H. Yu, Q. Zhang, A review of rechargeable batteries for portable electronic devices, InfoMat 1 (2019) 6–32, https://doi.org/10.1002/inf2.12000.

[59] Z. (John) Zhang, W. Fang, R. Ma, Brief review of batteries for XEV applications, eTransportation 2 (2019) 100032, https://doi.org/10.1016/j.etran.2019.100032.

[60] B. Diouf, R. Pode, Potential of lithium-ion batteries in renewable energy, Renew. Energy 76 (2015) 375–380, https://doi.org/10.1016/j.renene.2014.11.058.

[61] M. Winter, R.J. Brodd, What are batteries, fuel cells, and supercapacitors? Chem. Rev. 104 (2004) 4245–4269, https://doi.org/10.1021/cr020730k.

[62] G. Dolci, C. Tua, M. Grosso, L. Rigamonti, Life cycle assessment of consumption choices: a comparison between disposable and rechargeable household batteries, Int. J. Life Cycle Assess. 21 (2016) 1691–1705, https://doi.org/10.1007/s11367-016-1134-5.

[63] F. Yang, D. Wang, Y. Zhao, K.-L. Tsui, S.J. Bae, A study of the relationship between coulombic efficiency and capacity degradation of commercial lithium-ion batteries, Energy 145 (2018) 486–495, https://doi.org/10.1016/j.energy.2017.12.144.

[64] T. Wang, S. Chen, H. Pang, H. Xue, Y. Yu, MoS2-Based nanocomposites for electrochemical energy storage, Adv. Sci. 4 (2017), https://doi.org/10.1002/advs.201600289.

[65] J.C. Burns, A. Kassam, N.N. Sinha, L.E. Downie, L. Solnickova, B.M. Way, J. R. Dahn, Predicting and extending the lifetime of Li-ion batteries, J. Electrochem. Soc. 160 (2013), https://doi.org/10.1149/2.060309jes. A1451–A1456.

[66] F. Yang, X. Song, G. Dong, K.-L. Tsui, A coulombic efficiency-based model for prognostics and health estimation of lithium-ion batteries, Energy 171 (2019) 1173–1182, https://doi.org/10.1016/j.energy.2019.01.083.

[67] C. Liu, Z.G. Neale, G. Cao, Understanding electrochemical potentials of cathode materials in rechargeable batteries, Mater. Today 19 (2016) 109–123, https://doi.org/10.1016/j.mattod.2015.10.009.

[68] L.X. Yuan, Z.H. Wang, W.X. Zhang, X.L. Hu, J.T. Chen, Y.H. Huang, J. B. Goodenough, Development and challenges of LiFePO4 cathode material for lithium-ion batteries, Energy Environ. Sci. 4 (2011) 269–284, https://doi.org/10.1039/c0ee00029a.

[69] Y. Cao, M. Li, J. Lu, J. Liu, K. Amine, Bridging the academic and industrial metrics for next-generation practical batteries, Nat. Nanotechnol. (2019), https://doi.org/10.1038/s41565-019-0371-8.

[70] S.S. Madani, E. Schaltz, S.K. Kær, Effect of current rate and prior cycling on the coulombic efficiency of a lithium-ion battery, Batteries 5 (2019) 1–9, https://doi.org/10.3390/batteries5030057.

[71] X. Shen, H. Liu, X.-B. Cheng, C. Yan, J.-Q. Huang, Beyond lithium ion batteries: higher energy density battery systems based on lithium metal anodes, Energy Storage Mater. 12 (2018) 161–175, https://doi.org/10.1016/j.ensm.2017.12.002.

[72] X.G. Yang, Y. Leng, G. Zhang, S. Ge, C.Y. Wang, Modeling of lithium plating induced aging of lithium-ion batteries: transition from linear to nonlinear aging, J. Power Sources 360 (2017) 28–40, https://doi.org/10.1016/j.jpowsour.2017.05.110.

[73] Y. Gao, Graphene and polymer composites for supercapacitor applications: a review, Nanoscale Res. Lett. 12 (2017) 387, https://doi.org/10.1186/s11671-017-2150-5.

[74] W. Fan, Z. Peipei, P. Jiaolong, L. Chao, Y. Zhenyu, A facile electrospinning and electrospraying synchronization technique for preparation of high performance MnO/C@rGO composite anodes for lithium storage, RSC Adv. 7 (2017) 48294–48302, https://doi.org/10.1039/C7RA09636D.

[75] R. Mo, F. Li, X. Tan, P. Xu, R. Tao, G. Shen, X. Lu, F. Liu, L. Shen, B. Xu, Q. Xiao, X. Wang, C. Wang, J. Li, G. Wang, Y. Lu, High-quality mesoporous graphene particles as high-energy and fast-charging anodes for lithium-ion batteries, Nat. Commun. 10 (2019) 1474, https://doi.org/10.1038/s41467-019-09274-y.

[76] M. Wu, C. Liu, T. Ma, M. Tang, J. Shen, H. Ji, G. Yang, Heterostructural composite of few-layered MoS2/hexagonal MoO2 particles/graphene as anode material for highly reversible lithium/sodium storage, Int. J. Energy Res. 44 (2020) 518–527, https://doi.org/10.1002/er.4963.

[77] C. Uthaisar, V. Barone, Edge effects on the characteristics of Li diffusion in graphene, Nano Lett. 10 (2010) 2838–2842, https://doi.org/10.1021/nl100865a.

[78] E.G. Leggesse, C.L. Chen, J.C. Jiang, Lithium diffusion in graphene and graphite: effect of edge morphology, Carbon 103 (2016) 209–216, https://doi.org/10.1016/j.carbon.2016.03.016.

[79] N.A. Kaskhedikar, J. Maier, Lithium storage in carbon nanostructures, Adv. Mater. 21 (2009) 2664–2680, https://doi.org/10.1002/adma.200901079.

[80] S. Wang, J. Zhu, Y. Shao, W. Li, Y. Wu, L. Zhang, X. Hao, Three-dimensional MoS2@CNT/RGO network composites for high-performance flexible supercapacitors, Chem. Eur J. 23 (2017) 3438–3446, https://doi.org/10.1002/chem.201605465.

[81] R. Mo, F. Li, X. Tan, P. Xu, R. Tao, G. Shen, X. Lu, F. Liu, L. Shen, B. Xu, Q. Xiao, X. Wang, C. Wang, J. Li, G. Wang, Y. Lu, High-quality mesoporous graphene particles as high-energy and fast-charging anodes for lithium-ion batteries, Nat. Commun. 10 (2019) 1474, https://doi.org/10.1038/s41467-019-09274-y.

[82] M. Wu, C. Liu, T. Ma, M. Tang, J. Shen, H. Ji, G. Yang, Heterostructural composite of few-layered MoS2/hexagonal MoO2 particles/graphene as anode material for highly reversible lithium/sodium storage, Int. J. Energy Res. 44 (2020) 518–527, https://doi.org/10.1002/er.4963.

[83] C. Zhu, X. Mu, P.A. Vanaken, Y. Yu, J. Maier, Single-layered ultrasmall nanoplates of MoS2 embedded in carbon nanofibers with excellent electrochemical performance for lithium and sodium storage, Angew. Chem. Int. Ed. 53 (2014) 2152–2156, https://doi.org/10.1002/anie.201308354.

[84] C. George, A.J. Morris, M.H. Modarres, M. De Volder, Structural Evolution of electrochemically lithiated MoS 2 nanosheets and the role of carbon additive in Li-ion batteries, Chem. Mater. 28 (2016) 7304–7310, https://doi.org/10.1021/acs.chemmater.6b02607.

[85] Y. Kang, C. Deng, Y. Chen, X. Liu, Z. Liang, T. Li, Q. Hu, Y. Zhao, Binder-free electrodes and their application for Li-ion batteries, Nanoscale Res. Lett. 15 (2020), https://doi.org/10.1186/s11671-020-03325-w.

[86] J.Z. Wang, L. Lu, M. Lotya, J.N. Coleman, S.L. Chou, H.K. Liu, A.I. Minett, J. Chen, Development of MoS2-CNT composite thin film from layered MoS2 for lithium batteries, Adv. Energy Mater. 3 (2013) 798–805, https://doi.org/10.1002/aenm.201201000.

[87] F. Zoller, J. Luxa, T. Bein, D. Fattakhova-Rohlfing, D. Bouša, Z. Sofer, Flexible freestanding MoS2-based composite paper for energy conversion and storage, Beilstein J. Nanotechnol. 10 (2019) 1488–1496, https://doi.org/10.3762/bjnano.10.147.

[88] L. Noerochim, J.Z. Wang, S.L. Chou, D. Wexler, H.K. Liu, Free-standing single-walled carbon nanotube/SnO 2 anode paper for flexible lithium-ion batteries, Carbon 50 (2012) 1289–1297, https://doi.org/10.1016/j.carbon.2011.10.049.

[89] S.P. Patole, M.F. Arif, R.A. Susantyoko, S. Almheiri, S. Kumar, A wet-filtration-zipping approach for fabricating highly electroconductive and auxetic graphene/carbon nanotube hybrid buckypaper, Sci. Rep. 8 (2018) 1–12, https://doi.org/10.1038/s41598-018-30009-4.

[90] K. Shu, C. Wang, S. Li, C. Zhao, Y. Yang, H. Liu, G. Wallace, Flexible free-standing graphene paper with interconnected porous structure for energy storage, J. Mater. Chem. A 3 (2015) 4428–4434, https://doi.org/10.1039/C4TA04324C.

[91] Y. Zhong, T. Shi, Y. Huang, S. Cheng, C. Chen, G. Liao, Z. Tang, Three-dimensional MoS2/graphene aerogel as binder-free electrode for Li-ion battery, Nanoscale Res. Lett. 14 (2019), https://doi.org/10.1186/s11671-019-2916-z.

[92] S. Wang, R. Wang, Q. Zhao, L. Ren, J. Wen, J. Chang, X. Fang, N. Hu, C. Xu, Freeze-drying induced self-assembly approach for scalable constructing MoS 2/graphene hybrid aerogels for lithium-ion batteries, J. Colloid Interface Sci. 544 (2019) 37–45, https://doi.org/10.1016/j.jcis.2019.02.078.

[93] K. Chang, W. Chen, In situ synthesis of MoS2/graphene nanosheet composites with extraordinarily high electrochemical performance for lithium ion batteries, Chem. Commun. 47 (2011) 4252–4254, https://doi.org/10.1039/c1cc10631g.

[94] T.T. Shan, S. Xin, Y. You, H.P. Cong, S.H. Yu, A. Manthiram, Combining nitrogen-doped graphene sheets and MoS2: a unique film–foam–film structure for enhanced lithium storage, Angew. Chem. Int. Ed. 55 (2016) 12783–12788, https://doi.org/10.1002/anie.201606870.

[95] C. Lu, W.W. Liu, H. Li, B.K. Tay, A binder-free cnt network-mos2 composite as a high performance anode material in lithium ion batteries, Chem. Commun. 50 (2014) 3338–3340, https://doi.org/10.1039/c3cc49647c.

[96] X. Ma, X. Liu, J. Zhao, J. Hao, C. Chi, X. Liu, Y. Li, S. Liu, K. Zhang, Improved cycling stability of MoS2-coated carbon nanotubes on graphene foam as flexible anodes for lithium-ion batteries, New J. Chem. 41 (2017) 588–593, https://doi.org/10.1039/c6nj02238c.

[97] Z. Zhang, H. Zhao, Y. Teng, X. Chang, Q. Xia, Z. Li, J. Fang, Z. Du, K. Świerczek, Carbon-sheathed MoS2 Nanothorns epitaxially grown on CNTs: electrochemical application for highly stable and ultrafast lithium storage, Adv. Energy Mater. 8 (2018) 1–11, https://doi.org/10.1002/aenm.201700174.

[98] F. Pan, J. Wang, Z. Yang, L. Gu, Y. Yu, MoS2-graphene nanosheet-CNT hybrids with excellent electrochemical performances for lithium-ion batteries, RSC Adv. 5 (2015) 77518–77526, https://doi.org/10.1039/c5ra13262b.

[99] A. González, E. Goikolea, J.A. Barrena, R. Mysyk, Review on supercapacitors: technologies and materials, Renew. Sustain. Energy Rev. 58 (2016) 1189–1206, https://doi.org/10.1016/j.rser.2015.12.249.

[100] V.V.N. Obreja, On the performance of supercapacitors with electrodes based on carbon nanotubes and carbon activated material-A review, Phys. E Low-dimens. Syst. Nanostruct. 40 (2008) 2596–2605, https://doi.org/10.1016/j.physe.2007.09.044.

[101] P. Simon, Y. Gogotsi, Materials for Electrochemical Capacitors, Materials for Sustainable Energy: A Collection of Peer-Reviewed Research and Review Articles from, Nature Publishing Group, 2010, pp. 138–147, https://doi.org/10.1142/9789814317665_0021.

[102] H. Kim, M. Ramalingam, V. Balakumar, X. Zhang, W. Gao, Y.A. Son, P. D. Bradford, Chemically interconnected ternary AgNP/polypyrrole/functionalized buckypaper composites as high-energy-density supercapacitor electrodes, Chem. Phys. Lett. 739 (2020) 136957, https://doi.org/10.1016/j.cplett.2019.136957.

[103] Y.H. Kwon, S. Kumar, J. Bae, Y. Seo, CVD-graphene for low equivalent series resistance in rGO/CVD-graphene/Ni-based supercapacitors, Nanotechnology 29 (2018), https://doi.org/10.1088/1361-6528/aab236.

[104] A.G. Pandolfo, A.F. Hollenkamp, Carbon properties and their role in supercapacitors, J. Power Sources 157 (2006) 11–27, https://doi.org/10.1016/j.jpowsour.2006.02.065.

[105] N. Díez, C. Botas, R. Mysyk, E. Goikolea, T. Rojo, D. Carriazo, Highly packed graphene–CNT films as electrodes for aqueous supercapacitors with high volumetric performance, J. Mater. Chem. A 6 (2018) 3667–3673, https://doi.org/10.1039/C7TA10210K.

[106] A.P. Ranade, D.Y. Jung, B.G. Sammakia, T. Eilersten, T. Davis, Optimization study of supercapacitor electrode material composition and thickness for enhanced performance of the supercapacitor, Technical Proceedings of the 2011 NSTI Nanotechnology Conference and Expo, NSTI-Nanotech 2011 1 (2011) 730–733.

[107] S. Yoon, J.H. Jang, B.H. Ka, S.M. Oh, Complex capacitance analysis on rate capability of electric-double layer capacitor (EDLC) electrodes of different thickness, Electrochim. Acta 50 (2005) 2255–2262, https://doi.org/10.1016/j.electacta.2004.10.009.

[108] H. Muramatsu, T. Hayashi, Y.A. Kim, D. Shimamoto, Y.J. Kim, K. Tantrakarn, M. Endo, M. Terrones, M.S. Dresselhaus, Pore structure and oxidation stability of double-walled carbon nanotube-derived bucky paper, Chem. Phys. Lett. 414 (2005) 444–448, https://doi.org/10.1016/j.cplett.2005.08.110.

[109] E. Frackowiak, S. Delpeux, K. Jurewicz, K. Szostak, D. Cazorla-Amoros, F. Béguin, Enhanced capacitance of carbon nanotubes through chemical activation, Chem. Phys. Lett. 361 (2002) 35–41, https://doi.org/10.1016/S0009-2614(02)00684-X.

[110] K.D. Rasamani, F. Alimohammadi, Y. Sun, Interlayer-expanded MoS2, materials, Today Off. 20 (2017) 83–91, https://doi.org/10.1016/j.mattod.2016.10.004.

[111] R.A. Susantyoko, F. Parveen, I. Mustafa, S. Almheiri, MWCNT/activated-carbon freestanding sheets: a different approach to fabricate flexible electrodes for supercapacitors, Ionics 25 (2019) 265–273, https://doi.org/10.1007/s11581-018-2585-4.

[112] R.A. Susantyoko, Z. Karam, S. Alkhoori, I. Mustafa, C.H. Wu, S. Almheiri, A surface-engineered tape-casting fabrication technique toward the commercialisation of freestanding carbon nanotube sheets, J. Mater. Chem. A 5 (2017) 19255–19266, https://doi.org/10.1039/c7ta04999d.

[113] A. Burke, R&D considerations for the performance and application of electrochemical capacitors, Electrochim. Acta 53 (2007) 1083–1091, https://doi.org/10.1016/j.electacta.2007.01.011.

[114] X. Yang, C. Cheng, Y. Wang, L. Qiu, D. Li, Liquid-mediated dense integration of graphene materials for compact capacitive energy storage, Science 341 (2013) 534–537, https://doi.org/10.1126/science.1239089.

[115] D. Lin, Z. Tang, Q. Pan, S. Zhang, D. Huo, S. Yan, F. Han, Dense reduced graphene oxide films obtained by pressing create stable and compact capacitive energy storage, Chemelectrochem 7 (2020) 1987–1991, https://doi.org/10.1002/celc.202000246.

[116] A. Peigney, C. Laurent, E. Flahaut, R.R. Bacsa, A. Rousset, Specific surface area of carbon nanotubes and bundles of carbon nanotubes, Carbon 39 (2001) 507–514, https://doi.org/10.1016/S0008-6223(00)00155-X.

[117] H. Jiang, X. Ye, Y. Zhu, Z. Yue, L. Wang, J. Xie, Z. Wan, C. Jia, Flexible solid-state supercapacitors with high areal performance enabled by chlorine-doped graphene films with commercial-level mass loading, ACS Sustain. Chem. Eng. 7 (2019) 18844–18853, https://doi.org/10.1021/acssuschemeng.9b03810.

[118] Y. Zhu, X. Ye, H. Jiang, J. Xia, Z. Yue, L. Wang, Z. Wan, C. Jia, X. Yao, Controlled swelling of graphene films towards hierarchical structures for supercapacitor electrodes, J. Power Sources 453 (2020) 227851, https://doi.org/10.1016/j.jpowsour.2020.227851.

[119] L. Jiang, L. Sheng, C. Long, Z. Fan, Densely packed graphene nanomesh-carbon nanotube hybrid film for ultra-high volumetric performance supercapacitors, Nano Energy 11 (2015) 471–480, https://doi.org/10.1016/j.nanoen.2014.11.007.

[120] Z. Fan, Q. Zhao, T. Li, J. Yan, Y. Ren, J. Feng, T. Wei, Easy synthesis of porous graphene nanosheets and their use in supercapacitors, Carbon 50 (2012) 1699–1703, https://doi.org/10.1016/j.carbon.2011.12.016.

[121] H. Lu, S. Liu, Y. Zhang, Y. Huang, C. Zhang, T. Liu, Nitrogen-doped carbon Polyhedra Nanopapers: an advanced binder-free electrode for high-performance supercapacitors, ACS Sustain. Chem. Eng. 7 (2019) 5240–5248, https://doi.org/10.1021/acssuschemeng.8b06159.

[122] X. Wu, M. Yu, J. Liu, Y. Ma, S. Li, A facile pre-assembly strategy toward grain boundary-induced-graphene based hybrid frameworks with high capacitance, Chem. Eng. J. 381 (2020) 122684, https://doi.org/10.1016/j.cej.2019.122684.

[123] E. Frackowiak, K. Jurewicz, S. Delpeux, V. Bertagna, S. Bonnamy, F. Béguin, Synergy of components in supercapacitors based on nanotube/polypyrrole composites, Mol. Cryst. Liq. Cryst. 387 (2002) 73–78, https://doi.org/10.1080/10587250215244.

[124] T. Liu, L. Finn, M. Yu, H. Wang, T. Zhai, X. Lu, Y. Tong, Y. Li, Polyaniline and polypyrrole pseudocapacitor electrodes with excellent cycling stability, Nano Lett. 14 (2014) 2522–2527, https://doi.org/10.1021/nl500255v.

[125] E. Frackowiak, K. Jurewicz, S. Delpeux, F. Béguin, Nanotubular materials for supercapacitors, J. Power Sources 97–98 (2001) 822–825, https://doi.org/10.1016/S0378-7753(01)00736-4.

[126] A. Eftekhari, L. Li, Y. Yang, Polyaniline supercapacitors, J. Power Sources 347 (2017) 86–107, https://doi.org/10.1016/j.jpowsour.2017.02.054.

[127] Z. Zhao, G.F. Richardson, Q. Meng, S. Zhu, H.C. Kuan, J. Ma, PEDOT-based composites as electrode materials for supercapacitors, Nanotechnology 27 (2015), https://doi.org/10.1088/0957-4484/27/4/042001.

[128] C. Meng, C. Liu, L. Chen, C. Hu, S. Fan, Highly flexible and all-solid-state paperlike polymer supercapacitors, Nano Lett. 10 (2010) 4025–4031, https://doi.org/10.1021/nl1019672.

[129] V.H.R. De Souza, M.M. Oliveira, A.J.G. Zarbin, Thin and flexible all-solid supercapacitor prepared from novel single wall carbon nanotubes/polyaniline thin films obtained in liquid-liquid interfaces, J. Power Sources 260 (2014) 34–42, https://doi.org/10.1016/j.jpowsour.2014.02.070.

[130] Y. Chen, L. Du, P. Yang, P. Sun, X. Yu, W. Mai, Significantly enhanced robustness and electrochemical performance of flexible carbon nanotube-based supercapacitors by electrodepositing polypyrrole, J. Power Sources 287 (2015) 68–74, https://doi.org/10.1016/j.jpowsour.2015.04.026.

[131] M. Rajesh, C.J. Raj, R. Manikandan, B.C. Kim, S.Y. Park, K.H. Yu, A high performance PEDOT/PEDOT symmetric supercapacitor by facile in-situ hydrothermal polymerization of PEDOT nanostructures on flexible carbon fibre cloth electrodes, Mater. Today Energy 6 (2017) 96–104, https://doi.org/10.1016/j.mtener.2017.09.003.

[132] K. Liu, Y. Yao, T. Lv, H. Li, N. Li, Z. Chen, G. Qian, T. Chen, Textile-like electrodes of seamless graphene/nanotubes for wearable and stretchable supercapacitors, J. Power Sources 446 (2020) 227355, https://doi.org/10.1016/j.jpowsour.2019.227355.

[133] Y.H. Lee, K.H. Chang, C.C. Hu, Differentiate the pseudocapacitance and double-layer capacitance contributions for nitrogen-doped reduced graphene oxide in acidic and alkaline electrolytes, J. Power Sources 227 (2013) 300–308, https://doi.org/10.1016/j.jpowsour.2012.11.026.

[134] H.M. Jeong, J.W. Lee, W.H. Shin, Y.J. Choi, H.J. Shin, J.K. Kang, J.W. Choi, Nitrogen-doped graphene for high-performance ultracapacitors and the importance of nitrogen-doped sites at basal planes, Nano Lett. 11 (2011) 2472–2477, https://doi.org/10.1021/nl2009058.

[135] G. Lota, K. Lota, E. Frackowiak, Nanotubes based composites rich in nitrogen for supercapacitor application, Electrochem. Commun. 9 (2007) 1828–1832, https://doi.org/10.1016/j.elecom.2007.04.015.

[136] D. Yang, Y. Song, Y.J. Ye, M. Zhang, X. Sun, X.X. Liu, Boosting the pseudocapacitance of nitrogen-rich carbon nanorod arrays for electrochemical capacitors, J. Mater. Chem. A 7 (2019) 12086–12094, https://doi.org/10.1039/c9ta01973a.

[137] C.L. Rodríguez-Corvera, J.L. Fajardo-Díaz, A.J. Cortés-López, L.E. Jiménez-Ramírez, E. Muñoz-Sandoval, F. López-Urías, Nitrogen-doped carbon fiber sponges by using different nitrogen precursors: synthesis, characterization, and electrochemical activity, Mater. Today Chem. 14 (2019) 1–13, https://doi.org/10.1016/j.mtchem.2019.100200.

[138] C. Li, Y. Hu, M. Yu, Z. Wang, W. Zhao, P. Liu, Y. Tong, X. Lu, Nitrogen doped graphene paper as a highly conductive, and light-weight substrate for flexible supercapacitors, RSC Adv. (2014), https://doi.org/10.1039/c4ra11024b.

[139] X. Gao, G. Han, H. Song, Y. Chang, Y. Xiao, Y. Zhang, C. Liu, H. Li, Purified nitrogen-doped reduced graphene oxide hydrogels for high-performance supercapacitors, J. Electroanal. Chem. 834 (2019) 206–215, https://doi.org/10.1016/j.jelechem.2019.01.004.

[140] X. Wang, F. Wan, L. Zhang, Z. Zhao, Z. Niu, J. Chen, Large-area reduced graphene oxide composite films for flexible asymmetric sandwich and Microsized supercapacitors, Adv. Funct. Mater. 28 (2018) 1707247, https://doi.org/10.1002/adfm.201707247.

[141] S. Geetha, K.K. Satheesh Kumar, C.R.K. Rao, M. Vijayan, D.C. Trivedi, EMI shielding: methods and materials—a review, J. Appl. Polym. Sci. 112 (2009) 2073–2086, https://doi.org/10.1002/app.29812.

[142] J.-M. Thomassin, C. Jérôme, T. Pardoen, C. Bailly, I. Huynen, C. Detrembleur, Polymer/carbon based composites as electromagnetic interference (EMI) shielding materials, Mater. Sci. Eng. R Rep. 74 (2013) 211–232, https://doi.org/10.1016/j.mser.2013.06.001.

[143] X. Jian, B. Wu, Y. Wei, S.X. Dou, X. Wang, W. He, N. Mahmood, Facile synthesis of Fe3O4/GCs composites and their enhanced Microwave absorption properties, ACS Appl. Mater. Interfaces 8 (2016) 6101–6109, https://doi.org/10.1021/acsami.6b00388.

[144] Y. Wang, X. Jing, Intrinsically conducting polymers for electromagnetic interference shielding, Polym. Adv. Technol. 16 (2005) 344–351, https://doi.org/10.1002/pat.589.

[145] Y. Hu, D. Li, L. Wu, J. Yang, X. Jian, Y. Bin, Carbon nanotube buckypaper and buckypaper/polypropylene composites for high shielding effectiveness and absorption-dominated shielding material, Compos. Sci. Technol. 181 (2019) 107699, https://doi.org/10.1016/j.compscitech.2019.107699.

[146] L. Liu, A. Das, C.M. Megaridis, Terahertz shielding of carbon nanomaterials and their composites – a review and applications, Carbon 69 (2014) 1–16, https://doi.org/10.1016/j.carbon.2013.12.021.

[147] J. Liang, Y. Wang, Y. Huang, Y. Ma, Z. Liu, J. Cai, C. Zhang, H. Gao, Y. Chen, Electromagnetic interference shielding of graphene/epoxy composites, Carbon 47 (2009) 922–925, https://doi.org/10.1016/j.carbon.2008.12.038.

[148] H.-B. Zhang, Q. Yan, W.-G. Zheng, Z. He, Z.-Z. Yu, Tough Graphene−Polymer microcellular foams for electromagnetic interference shielding, ACS Appl. Mater. Interfaces 3 (2011) 918–924, https://doi.org/10.1021/am200021v.

[149] H. Zhang, G. Zhang, M. Tang, L. Zhou, J. Li, X. Fan, X. Shi, J. Qin, Synergistic effect of carbon nanotube and graphene nanoplates on the mechanical, electrical and electromagnetic interference shielding properties of polymer composites and polymer composite foams, Chem. Eng. J. 353 (2018) 381–393, https://doi.org/10.1016/j.cej.2018.07.144.

[150] F. Sharif, M. Arjmand, A.A. Moud, U. Sundararaj, E.P.L. Roberts, Segregated hybrid poly(methyl methacrylate)/graphene/Magnetite nanocomposites for electromagnetic interference shielding, ACS Appl. Mater. Interfaces 9 (2017) 14171–14179, https://doi.org/10.1021/acsami.6b13986.

[151] K. Batrakov, P. Kuzhir, S. Maksimenko, A. Paddubskaya, S. Voronovich, P. Lambin, T. Kaplas, Y. Svirko, Flexible transparent graphene/polymer multilayers for efficient electromagnetic field absorption, Sci. Rep. 4 (2014) 7191, https://doi.org/10.1038/srep07191.

[152] B. Shen, W. Zhai, W. Zheng, Ultrathin flexible graphene film: an excellent thermal conducting material with efficient EMI shielding, Adv. Funct. Mater. 24 (2014) 4542–4548, https://doi.org/10.1002/adfm.201400079.

[153] R. Yang, X. Gui, L. Yao, Q. Hu, L. Yang, H. Zhang, Y. Yao, H. Mei, Z. Tang, Ultrathin, lightweight, and flexible CNT buckypaper enhanced using MXenes for electromagnetic interference shielding, Nano-Micro Lett. 13 (2021) 66, https://doi.org/10.1007/s40820-021-00597-4.

[154] M. Fan, S. Li, L. Wu, L. Li, M. Qu, J. Nie, R. Zhang, P. Tang, Y. Bin, Natural rubber toughened carbon nanotube buckypaper and its multifunctionality in electromagnetic interference shielding, thermal conductivity, Joule heating and triboelectric nanogenerators, Chem. Eng. J. 433 (2022) 133499, https://doi.org/10.1016/j.cej.2021.133499.

[155] J.A. Rojas, B. Ribeiro, M.C. Rezende, Influence of serrated edge and rectangular strips of MWCNT buckypaper on the electromagnetic properties of glass fiber/epoxy resin composites, Carbon 160 (2020) 317–327, https://doi.org/10.1016/j.carbon.2020.01.036.

[156] M. Kim, S. Kim, Y.C. Seong, K.-H. Yang, H. Choi, Multiwalled carbon nanotube buckypaper/polyacrylonitrile nanofiber composite membranes for electromagnetic interference shielding, ACS Appl. Nano Mater. 4 (2021) 729–738, https://doi.org/10.1021/acsanm.0c03040.

[157] J. Federici, L. Moeller, Review of terahertz and subterahertz wireless communications, J. Appl. Phys. 107 (2010) 111101, https://doi.org/10.1063/1.3386413.

[158] J. Kim, D. Yoon, H. Son, D. Kim, J. Yoo, J. Yun, H.J. Ng, M. Kaynak, J.-S. Rieh, Terahertz signal source and Receiver operating near 600 GHz and their 3-D imaging application, IEEE Trans. Microw. Theor. Tech. 69 (2021) 2762–2775, https://doi.org/10.1109/TMTT.2021.3061596.

[159] O. Shenderova, V. Grishko, G. Cunningham, S. Moseenkov, G. McGuire, V. Kuznetsov, Onion-like carbon for terahertz electromagnetic shielding, Diam. Relat. Mater. 17 (2008) 462–466, https://doi.org/10.1016/j.diamond.2007.08.023.

[160] M.A. Kanygin, S.G. Stolyarova, K.V. Dorojkin, E.Y. Korovin, V.I. Suslyaev, L. G. Bulusheva, A.V. Okotrub, Electromagnetic properties of reduced graphene oxide buckypapers obtained by different reduction procedures, Phys. Status Solidi (2017) 1700271, https://doi.org/10.1002/pssb.201700271.

[161] J.T. Hong, D.J. Park, J.Y. Moon, S.B. Choi, J.K. Park, F. Rotermund, J.-Y. Park, S. Lee, Y.H. Ahn, Terahertz wave applications of single-walled carbon nanotube films with high shielding effectiveness, Appl. Phys. Express 5 (2012) 015102, https://doi.org/10.1143/APEX.5.015102.

[162] A. Das, T.M. Schutzius, C.M. Megaridis, S. Subhechha, T. Wang, L. Liu, Quasi-optical terahertz polarizers enabled by inkjet printing of carbon nanocomposites, Appl. Phys. Lett. 101 (2012) 243108, https://doi.org/10.1063/1.4770368.

[163] H. Yan, X. Li, B. Chandra, G. Tulevski, Y. Wu, M. Freitag, W. Zhu, P. Avouris, F. Xia, Tunable infrared plasmonic devices using graphene/insulator stacks, Nature Nanotech 7 (2012) 330–334, https://doi.org/10.1038/nnano.2012.59.

[164] J. Hansson, T.M.J. Nilsson, L. Ye, J. Liu, Novel nanostructured thermal interface materials: a review, Int. Mater. Rev. 63 (2018) 22–45, https://doi.org/10.1080/09506608.2017.1301014.

[165] A.A. Balandin, Thermal properties of graphene and nanostructured carbon materials, Nat. Mater. 10 (2011) 569–581, https://doi.org/10.1038/nmat3064.

[166] L. Wang, C. Pan, Z. Chen, W. Zhou, C. Gao, L. Wang, Enhanced Thermoelectric performance of conjugated polymer/single-walled carbon nanotube composites with strong stacking, ACS Appl. Energy Mater. 1 (2018) 5075–5082, https://doi.org/10.1021/acsaem.8b01126.

[167] K. Yoshino, T. Kato, Y. Saito, J. Shitaba, T. Hanashima, K. Nagano, S. Chiashi, Y. Homma, Temperature distribution and thermal conductivity measurements of chirality-Assigned single-walled carbon nanotubes by Photoluminescence imaging Spectroscopy, ACS Omega 3 (2018) 4352–4356, https://doi.org/10.1021/acsomega.8b00607.

[168] L. Lv, W. Dai, A. Li, C. Te Lin, Graphene-based thermal interface materials: an application-oriented perspective on architecture design, Polymers 10 (2018), https://doi.org/10.3390/polym10111201.

[169] C. Huang, X. Qian, R. Yang, Thermal conductivity of polymers and polymer nanocomposites, Mater. Sci. Eng. R Rep. 132 (2018) 1–22, https://doi.org/10.1016/j.mser.2018.06.002.

[170] S. Colonna, O. Monticelli, J. Gomez, C. Novara, G. Saracco, A. Fina, Effect of morphology and defectiveness of graphene-related materials on the electrical and thermal conductivity of their polymer nanocomposites, Polymer 102 (2016) 292–300, https://doi.org/10.1016/j.polymer.2016.09.032.

[171] H. Mohammadi, V. Morovati, E. Poshtan, R. Dargazany, Understanding decay functions and their contribution in modeling of thermal-induced aging of cross-linked polymers, Polym. Degrad. Stabil. 175 (2020) 109108, https://doi.org/10.1016/j.polymdegradstab.2020.109108.

[172] S. Huang, J. Bao, H. Ye, N. Wang, G. Yuan, W. Ke, D. Zhang, W. Yue, Y. Fu, L. Ye, K. Jeppson, J. Liu, The effects of graphene-based films as heat spreaders for thermal management in electronic packaging, 2016 17th International Conference on Electronic Packaging Technology, ICEPT 2016 (2016) 889–892, https://doi.org/10.1109/ICEPT.2016.7583272.

[173] M. Tortello, S. Colonna, M. Bernal, J. Gomez, M. Pavese, C. Novara, F. Giorgis, M. Maggio, G. Guerra, G. Saracco, R.S. Gonnelli, A. Fina, Effect of thermal annealing on the heat transfer properties of reduced graphite oxide flakes: a nanoscale characterization via scanning thermal microscopy, Carbon 109 (2016) 390–401, https://doi.org/10.1016/j.carbon.2016.08.017.

[174] X. Chen, X. Deng, N.Y. Kim, Y. Wang, Y. Huang, L. Peng, M. Huang, X. Zhang, X. Chen, D. Luo, B. Wang, X. Wu, Y. Ma, Z. Lee, R.S. Ruoff, Graphitization of graphene oxide films under pressure, Carbon 132 (2018) 294–303, https://doi.org/10.1016/j.carbon.2018.02.049.

[175] Y. Huang, Q. Gong, Q. Zhang, Y. Shao, J. Wang, Y. Jiang, M. Zhao, D. Zhuang, J. Liang, Fabrication and molecular dynamics analyses of highly thermal conductive reduced graphene oxide films at ultra-high temperatures, Nanoscale 9 (2017) 2340–2347, https://doi.org/10.1039/c6nr06653d.

[176] L. Peng, Z. Xu, Z. Liu, Y. Guo, P. Li, C. Gao, Ultrahigh thermal conductive yet Superflexible graphene films, Adv. Mater. 29 (2017) 1–8, https://doi.org/10.1002/adma.201700589.

[177] N. Wang, M.K. Samani, H. Li, L. Dong, Z. Zhang, P. Su, S. Chen, J. Chen, S. Huang, G. Yuan, X. Xu, B. Li, K. Leifer, L. Ye, J. Liu, Tailoring the thermal and mechanical properties of graphene film by structural engineering, Small 14 (2018) 1–8, https://doi.org/10.1002/smll.201801346.

[178] S. Ghosh, I. Calizo, D. Teweldebrhan, E.P. Pokatilov, D.L. Nika, A.A. Balandin, W. Bao, F. Miao, C.N. Lau, Extremely high thermal conductivity of graphene: prospects for thermal management applications in nanoelectronic circuits, Appl. Phys. Lett. 92 (2008) 151911, https://doi.org/10.1063/1.2907977.

[179] L. Cui, X. Du, G. Wei, Y. Feng, Thermal conductivity of graphene wrinkles: a molecular dynamics simulation, J. Phys. Chem. C 120 (2016) 23807–23812, https://doi.org/10.1021/acs.jpcc.6b07162.

[180] H. Lu, J. Zhang, J. Luo, W. Gong, C. Li, Q. Li, K. Zhang, M. Hu, Y. Yao, Enhanced thermal conductivity of free-standing 3D hierarchical carbon nanotube-graphene hybrid paper, Compos. Appl. Sci. Manuf. 102 (2017) 1–8, https://doi.org/10.1016/j.compositesa.2017.07.021.

[181] A. Akbari, B.V. Cunning, S.R. Joshi, C. Wang, D.C. Camacho-Mojica, S. Chatterjee, V. Modepalli, C. Cahoon, C.W. Bielawski, P. Bakharev, G.H. Kim, R.S. Ruoff, Highly ordered and dense thermally conductive graphitic films from a graphene oxide/reduced graphene oxide mixture, Matter 2 (2020) 1198–1206, https://doi.org/10.1016/j.matt.2020.02.014.

[182] X. Zhang, Y. Guo, Y. Liu, Z. Li, W. Fang, L. Peng, J. Zhou, Z. Xu, C. Gao, Ultrathick and highly thermally conductive graphene films by self-fusion strategy, Carbon 167 (2020) 249–255, https://doi.org/10.1016/j.carbon.2020.05.051.

[183] D.L. Nika, A.A. Balandin, Phonons and thermal transport in graphene and graphene-based materials, Rep. Prog. Phys. 80 (2017), https://doi.org/10.1088/1361-6633/80/3/036502.

[184] X. Mu, X. Wu, T. Zhang, D.B. Go, T. Luo, Thermal transport in graphene oxide - from ballistic extreme to amorphous limit, Sci. Rep. 4 (2014) 1–9, https://doi.org/10.1038/srep03909.

[185] Y. Yang, J. Cao, N. Wei, D. Meng, L. Wang, G. Ren, R. Yan, N. Zhang, Thermal conductivity of defective graphene oxide: a molecular dynamic study, Molecules 24 (2019), https://doi.org/10.3390/molecules24061103.

[186] S. Mann, I. Mudahar, H. Sharma, V.K. Jindal, G.S. Dubey, G. Gumbs, V. Fessatidis, Lattice Thermal Conductivity of Pristine and Doped (B,N) Graphene, arXiv, 2020.

[187] A.S. Nissimagoudar, N.S. Sankeshwar, Significant reduction of lattice thermal conductivity due to phonon confinement in graphene nanoribbons, Phys. Rev. B Condens. Matter 89 (2014), https://doi.org/10.1103/PhysRevB.89.235422.

[188] T. Ma, Z. Liu, J. Wen, Y. Gao, X. Ren, H. Chen, C. Jin, X.L. Ma, N. Xu, H.M. Cheng, W. Ren, Tailoring the thermal and electrical transport properties of graphene films by grain size engineering, Nat. Commun. 8 (2017) 1–9, https://doi.org/10.1038/ncomms14486.

[189] H. Li, S. Dai, J. Miao, X. Wu, N. Chandrasekharan, H. Qiu, J. Yang, Enhanced thermal conductivity of graphene/polyimide hybrid film via a novel “molecular welding” strategy, Carbon 126 (2018) 319–327, https://doi.org/10.1016/j.carbon.2017.10.044.

[190] H. Li, X. Wu, K. Cheng, J. Miao, Z. Tang, H. Qiu, J. Yang, Preparation of graphene oxide with large lateral size and graphene/polyimide hybrid film via in situ “molecular welding” strategy, Mater. Lett. 237 (2019) 168–171, https://doi.org/10.1016/j.matlet.2018.11.096.

[191] X. Wu, H. Li, K. Cheng, H. Qiu, J. Yang, Modified graphene/polyimide composite films with strongly enhanced thermal conductivity, Nanoscale 11 (2019) 8219–8225, https://doi.org/10.1039/c9nr02117e.

[192] R. Zou, F. Liu, N. Hu, H. Ning, X. Jiang, C. Xu, S. Fu, Y. Li, X. Zhou, C. Yan, Carbonized polydopamine nanoparticle reinforced graphene films with superior thermal conductivity, Carbon 149 (2019) 173–180, https://doi.org/10.1016/j.carbon.2019.04.038.

[193] J. Li, J. Lai, J. Liu, R. Lei, Y. Chen, Carbonized dehydroascorbic acid: aim for targeted repair of graphene defects and bridge connection of graphene sheets with small size, Nanomaterials 10 (2020), https://doi.org/10.3390/nano10030531.

[194] J. Li, X.Y. Chen, R.B. Lei, J.F. Lai, T.M. Ma, Y. Li, Highly thermally conductive graphene film produced using glucose under low-temperature thermal annealing, J. Mater. Sci. 54 (2019) 7553–7562, https://doi.org/10.1007/s10853-019-03406-x.

[195] K. Wang, M. Li, J. Zhang, H. Lu, Polyacrylonitrile coupled graphite oxide film with improved heat dissipation ability, Carbon 144 (2019) 249–258, https://doi.org/10.1016/j.carbon.2018.12.027.

[196] X. Su, H. Li, X. Lai, L. Zheng, Z. Chen, S. Zeng, K. Shen, L. Sun, X. Zeng, Bioinspired Superhydrophobic thermochromic films with robust healability, ACS Appl. Mater. Interfaces 12 (2020) 14578–14587, https://doi.org/10.1021/acsami.0c00344.

[197] B. Zhou, X. Han, L. Li, Y. Feng, T. Fang, G. Zheng, B. Wang, K. Dai, C. Liu, C. Shen, Ultrathin, flexible transparent Joule heater with fast response time based on single-walled carbon nanotubes/poly(vinyl alcohol) film, Compos. Sci. Technol. 183 (2019) 107796, https://doi.org/10.1016/j.compscitech.2019.107796.

[198] K.I.M. Duckjong, L. Zhu, D.-J. Jeong, K. Chun, Y.-Y. Bang, S.-R. Kim, J.-H. Kim, S.-K. Oh, Transparent flexible heater based on hybrid of carbon nanotubes and silver nanowires, Carbon 63 (2013) 530–536.

[199] Y. Kim, H.R. Lee, T. Saito, Y. Nishi, Ultra-thin and high-response transparent and flexible heater based on carbon nanotube film, Appl. Phys. Lett. 110 (2017) 153301, https://doi.org/10.1063/1.4978596.

[200] H. Im, E.Y. Jang, A. Choi, W.J. Kim, T.J. Kang, Y.W. Park, Y.H. Kim, Enhancement of heating performance of carbon nanotube sheet with granular metal, ACS Appl. Mater. Interfaces 4 (2012) 2338–2342, 5.

[201] F. Wang, W. Wang, X. Mu, J. Mao, Anisotropic conductive, tough and stretchable heater based on nacre-like crumpled graphene composite, Chem. Eng. J. 395 (2020) 125183, https://doi.org/10.1016/j.cej.2020.125183.

[202] P. Ilanchezhiyan, A.S. Zakirov, G.M. Kumar, S.U. Yuldashev, H.D. Cho, T. W. Kang, A.T. Mamadalimov, Highly efficient CNT functionalized cotton fabrics for flexible/wearable heating applications, RSC Adv. 5 (2015) 10697–10702, https://doi.org/10.1039/C4RA10667A.

[203] D. Janas, K.K. Koziol, Rapid electrothermal response of high-temperature carbon nanotube film heaters, Carbon 59 (2013) 457–463, https://doi.org/10.1016/j.carbon.2013.03.039.

[204] C. Kostaras, C. Pavlou, N. Koutroumanis, G. Paterakis, G. Trakakis, C. Galiotis, K. Dassios, Rapid resistive heating in graphene/carbon nanotube hybrid films for de-icing applications, ACS Appl. Nano Mater. 6 (2023) 5155–5167, https://doi.org/10.1021/acsanm.2c04999.

[205] Y. Lee, V.T. Le, J.-G. Kim, H. Kang, E.S. Kim, S.-E. Ahn, D. Suh, Versatile, high-power, flexible, stretchable carbon nanotube sheet heating elements tolerant to mechanical damage and severe deformation, Adv. Funct. Mater. 28 (2018) 1706007, https://doi.org/10.1002/adfm.201706007.

[206] R. Wang, Z. Xu, J. Zhuang, Z. Liu, L. Peng, Z. Li, Y. Liu, W. Gao, C. Gao, Highly stretchable graphene fibers with ultrafast electrothermal response for low-voltage wearable heaters, Adv. Electron. Mater. 3 (2017) 1600425, https://doi.org/10.1002/aelm.201600425.

[207] Y.-H. Yoon, J.-W. Song, D. Kim, J. Kim, J.-K. Park, S.-K. Oh, C.-S. Han, Transparent film heater using single-walled carbon nanotubes, Adv. Mater. 19 (2007) 4284–4287, https://doi.org/10.1002/adma.200701173.

[208] J. Wang, Z. Fang, H. Zhu, B. Gao, S. Garner, P. Cimo, Z. Barcikowski, A. Mignerey, L. Hu, Flexible, transparent, and conductive defrosting glass, Thin Solid Films 556 (2014) 13–17, https://doi.org/10.1016/j.tsf.2013.12.060.

[209] D. Sui, Y. Huang, L. Huang, J. Liang, Y. Ma, Y. Chen, Flexible and transparent electrothermal film heaters based on graphene materials, Small 7 (2011) 3186–3192, https://doi.org/10.1002/smll.201101305.

[210] D. Kim, H.-C. Lee, J.Y. Woo, C.-S. Han, Thermal behavior of transparent film heaters made of single-walled carbon nanotubes, J. Phys. Chem. C 114 (2010) 5817–5821, https://doi.org/10.1021/jp910799a.

[211] D. Jung, D. Kim, K.H. Lee, L.J. Overzet, G.S. Lee, Transparent film heaters using multi-walled carbon nanotube sheets, Sensor Actuator Phys. 199 (2013) 176–180, https://doi.org/10.1016/j.sna.2013.05.024.

[212] S. Sorel, D. Bellet, J.N. Coleman, Relationship between material properties and transparent heater performance for both bulk-like and percolative nanostructured networks, ACS Nano 8 (2014) 4805–4814, https://doi.org/10.1021/nn500692d.

[213] Y. Zhan, Y. Li, Y. Meng, Q. Xie, M. Lavorgna, Electric heating behavior of reduced oxide graphene/carbon nanotube/natural rubber composites with macro-porous structure and segregated filler network, Polymers 12 (2020) 2411, https://doi.org/10.3390/polym12102411.

[214] R. Zhou, P. Li, Z. Fan, D. Du, J. Ouyang, Stretchable heaters with composites of an intrinsically conductive polymer, reduced graphene oxide and an elastomer for wearable thermotherapy, J. Mater. Chem. C 5 (2017) 1544–1551, https://doi.org/10.1039/C6TC04849H.

[215] Z. Zhang, H. Dong, Y. Liao, E.X. Ding, L. Lv, H. Li, J. Yan, E.I. Kauppinen, Dry-transferred single-walled carbon nanotube thin films for flexible and transparent heaters, Surf. Interfaces 31 (2022) 101992, https://doi.org/10.1016/j.surfin.2022.101992.

[216] Y. Guo, C. Dun, J. Xu, J. Mu, P. Li, L. Gu, C. Hou, C.A. Hewitt, Q. Zhang, Y. Li, D. L. Carroll, H. Wang, Ultrathin, washable, and large-area graphene papers for personal thermal management, Small 13 (2017) 1702645, https://doi.org/10.1002/smll.201702645.

[217] J. Li, Y. Wang, T.-N. Yue, Y.-N. Gao, Y.-D. Shi, J.-B. Shen, H. Wu, M. Wang, Robust electromagnetic interference shielding, joule heating, thermal conductivity, and anti-dripping performances of polyoxymethylene with uniform distribution and high content of carbon-based nanofillers, Compos. Sci. Technol. 206 (2021) 108681, https://doi.org/10.1016/j.compscitech.2021.108681.

[218] H. Chang, Y. Jia, L. Xiao, H. Chen, K. Zhao, Y. Chen, Y. Ma, Three dimensional cross-linked and flexible graphene composite paper with ultrafast electrothermal response at ultra-low voltage, Carbon 154 (2019) 150–155, https://doi.org/10.1016/j.carbon.2019.08.008.

[219] L.R. Shobin, S. Manivannan, Enhancement of electrothermal performance in single-walled carbon nanotube transparent heaters by room temperature post treatment, Sol. Energy Mater. Sol. Cell. 174 (2018) 469–477, https://doi.org/10.1016/j.solmat.2017.09.041.

[220] A. Abdulkareem Muhsan, K. Lafdi, Fabrication and characterization of graphene-based de-icing heater, Mater. Today: Proc. 52 (2022) 206–211, https://doi.org/10.1016/j.matpr.2021.09.485.

[221] Y. Liu, C. Liang, A. Wei, Y. Jiang, Q. Tian, Y. Wu, Z. Xu, Y. Li, F. Guo, Q. Yang, W. Gao, H. Wang, C. Gao, Solder-free electrical Joule welding of macroscopic graphene assemblies, Materials Today Nano 3 (2018) 1–8, https://doi.org/10.1016/j.mtnano.2018.09.005.

[222] Y. Liu, P. Li, F. Wang, W. Fang, Z. Xu, W. Gao, C. Gao, Rapid roll-to-roll production of graphene film using intensive Joule heating, Carbon 155 (2019) 462–468, https://doi.org/10.1016/j.carbon.2019.09.021.

[223] Y. Chen, K. Fu, S. Zhu, W. Luo, Y. Wang, Y. Li, E. Hitz, Y. Yao, J. Dai, J. Wan, V. A. Danner, T. Li, L. Hu, Reduced graphene oxide films with ultrahigh conductivity as Li-ion battery current collectors, Nano Lett. 16 (2016) 3616–3623, https://doi.org/10.1021/acs.nanolett.6b00743.

[224] W. Bao, A.D. Pickel, Q. Zhang, Y. Chen, Y. Yao, J. Wan, K. Fu, Y. Wang, J. Dai, H. Zhu, D. Drew, M. Fuhrer, C. Dames, L. Hu, Flexible, high temperature, planar lighting with large scale printable nanocarbon paper, Adv. Mater. 28 (2016) 4684–4691, https://doi.org/10.1002/adma.201506116.

[225] J.D. Renteria, S. Ramirez, H. Malekpour, B. Alonso, A. Centeno, A. Zurutuza, A. I. Cocemasov, D.L. Nika, A.A. Balandin, Strongly anisotropic thermal conductivity of free-standing reduced graphene oxide films annealed at high temperature, Adv. Funct. Mater. 25 (2015) 4664–4672, https://doi.org/10.1002/adfm.201501429.

[226] S. Hong, S.S. Yoo, P.J. Yoo, Binder-free heat dissipation films assembled with reduced graphene oxide and alumina nanoparticles for simultaneous high in-plane and cross-plane thermal conductivities, J. Mater. Chem. C 7 (2019) 9380–9388, https://doi.org/10.1039/c9tc02143d.

[227] T.W. Pan, W.S. Kuo, N.H. Tai, Tailoring anisotropic thermal properties of reduced graphene oxide/multi-walled carbon nanotube hybrid composite films, Compos. Sci. Technol. 151 (2017) 44–51, https://doi.org/10.1016/j.compscitech.2017.07.015.

[228] H. Jia, Q.Q. Kong, X. Yang, L.J. Xie, G.H. Sun, L.L. Liang, J.P. Chen, D. Liu, Q. G. Guo, C.M. Chen, Dual-functional graphene/carbon nanotubes thick film: bidirectional thermal dissipation and electromagnetic shielding, Carbon 171 (2021) 329–340, https://doi.org/10.1016/j.carbon.2020.09.017.

[229] D. Hu, W. Gong, J. Di, D. Li, R. Li, W. Lu, B. Gu, B. Sun, Q. Li, Strong graphene-interlayered carbon nanotube films with high thermal conductivity, Carbon 118 (2017) 659–665, https://doi.org/10.1016/j.carbon.2017.04.005.

[230] J. Zhang, G. Shi, C. Jiang, S. Ju, D. Jiang, 3D bridged carbon nanoring/graphene hybrid paper as a high-performance lateral heat spreader, Small 11 (2015) 6197–6204, https://doi.org/10.1002/smll.201501878.

[231] J. Gao, Q. Yan, L. Lv, X. Tan, J. Ying, K. Yang, J. Yu, S. Du, Q. Wei, R. Xiang, Y. Yao, X. Zeng, R. Sun, C.P. Wong, N. Jiang, C. Te Lin, W. Dai, Lightweight thermal interface materials based on hierarchically strucntured graphene paper with superior through-plane thermal conductivity, Chem. Eng. J. 419 (2021), https://doi.org/10.1016/j.cej.2021.129609.

[232] G. Xin, H. Sun, T. Hu, H.R. Fard, X. Sun, N. Koratkar, T. Borca-Tasciuc, J. Lian, Large-area freestanding graphene paper for superior thermal management, Adv. Mater. 26 (2014) 4521–4526, https://doi.org/10.1002/adma.201400951.

[233] G. Xin, W. Zhu, T. Yao, S.M. Scott, J. Lian, Microstructure control of macroscopic graphene paper by electrospray deposition and its effect on thermal and electrical conductivities, Appl. Phys. Lett. 110 (2017) 091909, https://doi.org/10.1063/1.4977850.

[234] X. Gao, J. Jang, S. Nagase, Hydrazine and thermal reduction of graphene oxide: reaction mechanisms, product structures, and reaction design, J. Phys. Chem. C 114 (2010) 832–842, https://doi.org/10.1021/jp909284g.

[235] P. Kumar, F. Shahzad, S. Yu, S.M. Hong, Y.H. Kim, C.M. Koo, Large-area reduced graphene oxide thin film with excellent thermal conductivity and electromagnetic interference shielding effectiveness, Carbon 94 (2015) 494–500, https://doi.org/10.1016/j.carbon.2015.07.032.

[236] S. Pei, J. Zhao, J. Du, W. Ren, H.M. Cheng, Direct reduction of graphene oxide films into highly conductive and flexible graphene films by hydrohalic acids, Carbon 48 (2010) 4466–4474, https://doi.org/10.1016/j.carbon.2010.08.006.

[237] G. Yang, H. Yi, Y. Yao, C. Li, Z. Li, Thermally conductive graphene films for heat dissipation, ACS Appl. Nano Mater. (2020), https://doi.org/10.1021/acsanm.9b01955.

[238] Y. Li, Y. Zhu, G. Jiang, Z.P. Cano, J. Yang, J. Wang, J. Liu, X. Chen, Z. Chen, Boosting the heat dissipation performance of graphene/polyimide flexible carbon film via enhanced through-plane conductivity of 3D hybridized structure, Small 16 (2020) 1–9, https://doi.org/10.1002/smll.201903315.

[239] E. Lasseuguette, M.-C. Ferrari, Chapter 10 - polymer membranes for sustainable gas separation, in: G. Szekely, A. Livingston (Eds.), Sustainable Nanoscale Engineering, Elsevier, 2020, pp. 265–296, https://doi.org/10.1016/B978-0-12-814681-1.00010-2.

[240] B.M. Yoo, J.E. Shin, H.D. Lee, H.B. Park, Graphene and graphene oxide membranes for gas separation applications, Current Opinion in Chemical Engineering 16 (2017) 39–47, https://doi.org/10.1016/j.coche.2017.04.004.

[241] N. Zhang, Y. Luo, Z. Li, H. Yu, E. Jiang, Z. Li, Y. Dai, J. Bao, X. Zhang, G. He, Molecular investigation on the mechanism of permselective transport of CO2/N2 mixture through graphene slit, Separ. Purif. Technol. 282 (2022) 119986, https://doi.org/10.1016/j.seppur.2021.119986.

[242] F. Zhou, Q. Dong, J.-T. Chen, B. Sengupta, J. Jiang, W.L. Xu, H. Li, S. Li, M. Yu, Printed graphene oxide-based membranes for gas separation and carbon capture, Chem. Eng. J. 430 (2022) 132942, https://doi.org/10.1016/j.cej.2021.132942.

[243] J. Widakdo, G.T.M. Kadja, A. Anawati, T.M. Subrahmanya, H.F.M. Austria, T.-H. Huang, E. Suharyadi, W.-S. Hung, Graphene oxide-melamine nanofilm composite membrane for efficient CO2 gas separation, Separ. Purif. Technol. 323 (2023) 124521, https://doi.org/10.1016/j.seppur.2023.124521.

[244] S. Amjad-Iranagh, P. Mahimani, The effect of nanofillers in pollution and environment, in: S. Mallakpour, C.M. Hussain (Eds.), Handbook of Nanofillers, Springer Nature, Singapore, 2024, pp. 1–33, https://doi.org/10.1007/978-981-99-3516-1_59-1.

[245] J. Xu, D. Yang, H. Zhang, M. Guan, Q. Li, M. Cai, Q. Hu, Q. Liu, X. Han, Selectivity enhancement by the presence of HOF + CNT composite membranes investigated by non-equilibrium molecular dynamics, Separ. Purif. Technol. 330 (2024) 125472, https://doi.org/10.1016/j.seppur.2023.125472.

[246] S.W. Cranford, M.J. Buehler, In silico assembly and nanomechanical characterization of carbon nanotube buckypaper, Nanotechnology 21 (2010) 265706, https://doi.org/10.1088/0957-4484/21/26/265706.

[247] L. Li, C. Song, D. Jiang, T. Wang, Preparation and enhanced gas separation performance of Carbon/Carbon nanotubes (C/CNTs) hybrid membranes, Separ. Purif. Technol. 188 (2017) 73–80, https://doi.org/10.1016/j.seppur.2017.07.019.

[248] S.E. Kentish, C.A. Scholes, G.W. Stevens, Carbon Dioxide Separation through Polymeric Membrane Systems for Flue Gas Applications, Recent Pat. Chem. Eng. 1 (n.d.)52–66. https://doi.org/10.2174/2211334710801010052..

[249] I.J.M. De Boer, I.E. Hoving, T.V. Vellinga, G.W.J. Van De Ven, P.A. Leffelaar, P. J. Gerber, Assessing environmental impacts associated with freshwater consumption along the life cycle of animal products: the case of Dutch milk production in Noord-Brabant, Int. J. Life Cycle Assess. (2013), https://doi.org/10.1007/s11367-012-0446-3.

[250] S. Malamis, E. Katsou, K.J. Haralambous, Study of Ni(II), Cu(II), Pb(II), and Zn(II) removal using sludge and minerals followed by MF/UF, Water, Air, and Soil Pollution 218 (2011) 81–92, https://doi.org/10.1007/s11270-010-0625-4.

[251] E. Iloms, O.O. Ololade, H.J.O. Ogola, R. Selvarajan, Investigating Industrial Effluent Impact on Municipal Wastewater Treatment Plant in Vaal, South Africa,

International Journal of Environmental Research and Public Health, 2020, https://doi.org/10.3390/ijerph17031096.
[252] D.W. Kolpin, E.T. Furlong, M.T. Meyer, E.M. Thurman, S.D. Zaugg, L.B. Barber, H. T. Buxton, Pharmaceuticals, hormones, and other organic wastewater contaminants in U.S. streams, 1999-2000: a national reconnaissance, Environ. Sci. Technol. 36 (2002) 1202–1211, https://doi.org/10.1021/es011055j.
[253] N.B. Singh, G. Nagpal, S. Agrawal, Rachna, water purification by using adsorbents: a review, Environ. Technol. Innovat. 11 (2018) 187–240, https://doi.org/10.1016/j.eti.2018.05.006.
[254] C.S. Lee, J. Robinson, M.F. Chong, A review on application of flocculants in wastewater treatment, Process Saf. Environ. Protect. 92 (2014) 489–508, https://doi.org/10.1016/j.psep.2014.04.010.
[255] S. Ahmadvand, B. Abbasi, B. Azarfar, M. Elhashimi, X. Zhang, B. Abbasi, Looking beyond energy efficiency: an applied review of water desalination technologies and an introduction to capillary-driven desalination, Water (Switzerland) 11 (2019), https://doi.org/10.3390/w11040696.
[256] N.K. Khanzada, M.U. Farid, J.A. Kharraz, J. Choi, C.Y. Tang, L.D. Nghiem, A. Jang, A.K. An, Removal of organic micropollutants using advanced membrane-based water and wastewater treatment: a review, J. Membr. Sci. 598 (2020) 117672, https://doi.org/10.1016/j.memsci.2019.117672.
[257] R. Semiat, Energy Issues in Desalination Processes, Environmental Science and Technology, 2008, https://doi.org/10.1021/es801330u.
[258] S. Lin, Energy Efficiency of Desalination: Fundamental Insights from Intuitive Interpretation, Environmental Science and Technology, 2020, https://doi.org/10.1021/acs.est.9b04788.
[259] A. Al-Karaghouli, L.L. Kazmerski, Energy Consumption and Water Production Cost of Conventional and Renewable-Energy-Powered Desalination Processes, Renewable and Sustainable Energy Reviews, 2013, https://doi.org/10.1016/j.rser.2012.12.064.
[260] M. Qasim, M. Badrelzaman, N.N. Darwish, N.A. Darwish, N. Hilal, Reverse osmosis desalination: a state-of-the-art review, Desalination 459 (2019) 59–104, https://doi.org/10.1016/j.desal.2019.02.008.
[261] K. Elsaid, E.T. Sayed, M.A. Abdelkareem, A. Baroutaji, A.G. Olabi, Environmental Impact of Desalination Processes: Mitigation and Control Strategies, Science of the Total Environment, 2020, https://doi.org/10.1016/j.scitotenv.2020.140125.
[262] H. Shemer, R. Semiat, Sustainable RO desalination – energy demand and environmental impact, Desalination 424 (2017) 10–16, https://doi.org/10.1016/j.desal.2017.09.021.
[263] S. Lattemann, T. Höpner, Environmental Impact and Impact Assessment of Seawater Desalination, 2008, https://doi.org/10.1016/j.desal.2007.03.009. Desalination.
[264] H. Frank, E. Rahav, E. Bar-Zeev, Short-term Effects of SWRO Desalination Brine on Benthic Heterotrophic Microbial Communities, 2017, https://doi.org/10.1016/j.desal.2017.04.031. Desalination.
[265] B. Khorshidi, T. Thundat, B.A. Fleck, M. Sadrzadeh, A novel approach toward fabrication of high performance thin film composite polyamide membranes, Sci. Rep. (2016), https://doi.org/10.1038/srep22069.
[266] B. Deng, Effects of polysulfone (PSf) support layer on the performance of thin-film composite (TFC) membranes, Journal of Chemical and Process Engineering (2013), https://doi.org/10.17303/jce.2014.102.
[267] S. Hong, I.-C. Kim, T. Tak, Y.-N. Kwon, Interfacially synthesized chlorine-resistant polyimide thin film composite (TFC) reverse osmosis (RO) membranes, Desalination 309 (2013) 18–26, https://doi.org/10.1016/j.desal.2012.09.025.
[268] S.T. Mitrouli, A.J. Karabelas, N.P. Isaias, Polyamide active layers of low pressure RO membranes: data on spatial performance non-uniformity and degradation by hypochlorite solutions, Desalination 260 (2010) 91–100, https://doi.org/10.1016/j.desal.2010.04.061.
[269] Y. Hanafi, A. Szymczyk, M. Rabiller-Baudry, K. Baddari, Degradation of Poly (ether Sulfone)/polyvinylpyrrolidone Membranes by Sodium Hypochlorite: Insight from Advanced Electrokinetic Characterizations, Environmental Science and Technology, 2014, https://doi.org/10.1021/es5027882.
[270] A. Antony, R. Fudianto, S. Cox, G. Leslie, Assessing the oxidative degradation of polyamide reverse osmosis membrane-Accelerated ageing with hypochlorite exposure, J. Membr. Sci. (2010), https://doi.org/10.1016/j.memsci.2009.10.018.
[271] M. Stolov, V. Freger, Degradation of Polyamide Membranes Exposed to Chlorine: an Impedance Spectroscopy Study, Environmental Science and Technology, 2019, https://doi.org/10.1021/acs.est.8b04790.
[272] R. Verbeke, V. Gómez, I.F.J. Vankelecom, Chlorine-resistance of reverse osmosis (RO) polyamide membranes, Prog. Polym. Sci. 72 (2017) 1–15, https://doi.org/10.1016/j.progpolymsci.2017.05.003.
[273] J. Kucera, Biofouling of polyamide membranes: fouling mechanisms, current mitigation and cleaning strategies, and future prospects, Membranes 9 (2019), https://doi.org/10.3390/membranes9090111.
[274] L. Zhou, L. Zhou, M. Yang, D. Wu, L. Liao, K. Yan, Q. Xie, Z. Liu, H. Peng, Z. Liu, Free radical reactions in two dimensions: a case study on photochlorination of graphene, Small 9 (2013) 1388–1396, https://doi.org/10.1002/smll.201202969.
[275] A. Martínez, A. Galano, Free radical scavenging activity of ultrashort single-walled carbon nanotubes with different structures through electron transfer reactions, J. Phys. Chem. C 114 (2010) 8184–8191, https://doi.org/10.1021/jp100168q.
[276] A. Galano, Carbon nanotubes as free-radical scavengers, J. Phys. Chem. C 112 (2008) 8922–8927, https://doi.org/10.1021/jp801379g.
[277] H.J. Kim, M.Y. Lim, K.H. Jung, D.G. Kim, J.C. Lee, High-performance reverse osmosis nanocomposite membranes containing the mixture of carbon nanotubes and graphene oxides, J. Mater. Chem. A 3 (2015) 6798–6809, https://doi.org/10.1039/c4ta06080f.
[278] V.V. Neklyudov, N.R. Khafizov, I.A. Sedov, A.M. Dimiev, New insights into the solubility of graphene oxide in water and alcohols, Phys. Chem. Chem. Phys. 19 (2017) 17000–17008, https://doi.org/10.1039/c7cp02303k.
[279] G. Hamdy, A. Taher, Enhanced chlorine-resistant and low biofouling reverse osmosis polyimide-graphene oxide thin film nanocomposite membranes for water desalination, Polym. Eng. Sci. 60 (2020) 2567–2580, https://doi.org/10.1002/pen.25495.
[280] H.R. Chae, J. Lee, C.H. Lee, I.C. Kim, P.K. Park, Graphene oxide-embedded thin-film composite reverse osmosis membrane with high flux, anti-biofouling, and chlorine resistance, J. Membr. Sci. (2015), https://doi.org/10.1016/j.memsci.2015.02.045.
[281] S. Rajesh, A.B. Bose, Development of graphene oxide framework membranes via the “from” and “to” cross-linking approach for ion-selective separations, ACS Appl. Mater. Interfaces 11 (2019) 27706–27716, https://doi.org/10.1021/acsami.9b05465.
[282] W. Choi, J. Choi, J. Bang, J.-H. Lee, Layer-by-Layer assembly of graphene oxide nanosheets on polyamide membranes for durable reverse-osmosis applications, ACS Appl. Mater. Interfaces 5 (2013) 12510–12519, https://doi.org/10.1021/am403790s.
[283] F. Shao, L. Dong, H. Dong, Q. Zhang, M. Zhao, L. Yu, B. Pang, Y. Chen, Graphene oxide modified polyamide reverse osmosis membranes with enhanced chlorine resistance, J. Membr. Sci. (2017), https://doi.org/10.1016/j.memsci.2016.12.001.
[284] W. Ma, A. Soroush, T.V.A. Luong, M.S. Rahaman, Cysteamine- and graphene oxide-mediated copper nanoparticle decoration on reverse osmosis membrane for enhanced anti-microbial performance, J. Colloid Interface Sci. 501 (2017) 330–340, https://doi.org/10.1016/j.jcis.2017.04.069.
[285] A. Lerf, A. Buchsteiner, J. Pieper, S. Schöttl, I. Dekany, T. Szabo, H.P. Boehm, Hydration behavior and dynamics of water molecules in graphite oxide, J. Phys. Chem. Solid. 67 (2006) 1106–1110, https://doi.org/10.1016/j.jpcs.2006.01.031.
[286] J. Abraham, K.S. Vasu, C.D. Williams, K. Gopinadhan, Y. Su, C.T. Cherian, J. Dix, E. Prestat, S.J. Haigh, I.V. Grigorieva, P. Carbone, A.K. Geim, R.R. Nair, Tunable sieving of ions using graphene oxide membranes, Nat. Nanotechnol. (2017), https://doi.org/10.1038/nnano.2017.21.
[287] G. Liu, H. Ye, A. Li, C. Zhu, H. Jiang, Y. Liu, K. Han, Y. Zhou, Graphene oxide for high-efficiency separation membranes: role of electrostatic interactions, Carbon 110 (2016) 56–61, https://doi.org/10.1016/j.carbon.2016.09.005.
[288] N.K. Khanzada, S. Rehman, S.Y. Leu, A.K. An, Evaluation of anti-bacterial adhesion performance of polydopamine cross-linked graphene oxide RO membrane via in situ optical coherence tomography, Desalination 479 (2020) 114339, https://doi.org/10.1016/j.desal.2020.114339.
[289] M. Abbaszadeh, D. Krizak, S. Kundu, Layer-by-layer assembly of graphene oxide nanoplatelets embedded desalination membranes with improved chlorine resistance, Desalination 470 (2019) 114116, https://doi.org/10.1016/j.desal.2019.114116.
[290] J. Kucera, Biofouling of polyamide membranes: fouling mechanisms, current mitigation and cleaning strategies, and future prospects, Membranes 9 (2019), https://doi.org/10.3390/membranes9090111.
[291] F. Perreault, M.E. Tousley, M. Elimelech, Thin-film composite polyamide membranes functionalized with biocidal graphene oxide nanosheets, Environ. Sci. Technol. Lett. 1 (2014) 71–76, https://doi.org/10.1021/ez4001356.
[292] Y. Li, S. Yuan, Y. Xia, W. Zhao, C.D. Easton, C. Selomulya, X. Zhang, Mild annealing reduced graphene oxide membrane for nanofiltration, J. Membr. Sci. 601 (2020) 117900, https://doi.org/10.1016/j.memsci.2020.117900.
[293] T. Yoshioka, K. Kotaka, K. Nakagawa, T. Shintani, H.-C. Wu, H. Matsuyama, Y. Fujimura, T. Kawakatsu, Molecular dynamics simulation study of polyamide membrane structures and RO/FO water permeation properties, Membranes 8 (2018) 127, https://doi.org/10.3390/membranes8040127.
[294] P. Tapia-Quirós, M.F. Montenegro-Landívar, M. Reig, X. Vecino, J. Saurina, M. Granados, J.L. Cortina, Integration of nanofiltration and reverse osmosis technologies in polyphenols recovery schemes from winery and olive mill wastes by aqueous-based processing, Membranes 12 (2022) 339, https://doi.org/10.3390/membranes12030339.
[295] K. Maheshwari, A.B. Gupta, R. Gupta, M. Agarwal, Desalinating RO retentate employing NF coupled with CDI: a path towards cleaner production, J. Clean. Prod. 395 (2023) 136405, https://doi.org/10.1016/j.jclepro.2023.136405.
[296] K. Goh, L. Setiawan, L. Wei, R. Si, A.G. Fane, R. Wang, Y. Chen, Graphene oxide as effective selective barriers on a hollow fiber membrane for water treatment process, J. Membr. Sci. 474 (2015) 244–253, https://doi.org/10.1016/j.memsci.2014.09.057.
[297] N. Song, X. Gao, Z. Ma, X. Wang, Y. Wei, C. Gao, A review of graphene-based separation membrane: materials, characteristics, preparation and applications, Desalination 437 (2018) 59–72, https://doi.org/10.1016/j.desal.2018.02.024.
[298] J. Zhu, M. Tian, J. Hou, J. Wang, J. Lin, Y. Zhang, J. Liu, B. Van Der Bruggen, Surface zwitterionic functionalized graphene oxide for a novel loose nanofiltration membrane, J. Mater. Chem. A 4 (2016) 1980–1990, https://doi.org/10.1039/c5ta08024j.
[299] J. Kim, S.E. Lee, S. Seo, J.Y. Woo, C.S. Han, Near-complete blocking of multivalent anions in graphene oxide membranes with tunable interlayer spacing from 3.7 to 8.0 angstrom, J. Membr. Sci. 592 (2019) 117394, https://doi.org/10.1016/j.memsci.2019.117394.
[300] P. Sun, F. Zheng, M. Zhu, Z. Song, K. Wang, M. Zhong, D. Wu, R.B. Little, Z. Xu, H. Zhu, Selective trans-membrane transport of alkali and alkaline earth cations through graphene oxide membranes based on Cation−$\pi$ interactions, ACS Nano 8 (2014) 850–859, https://doi.org/10.1021/nn4055682.

[301] G.S. Lai, W.J. Lau, P.S. Goh, A.F. Ismail, N. Yusof, Y.H. Tan, Graphene oxide incorporated thin film nanocomposite nanofiltration membrane for enhanced salt removal performance, Desalination 387 (2016) 14–24, https://doi.org/10.1016/j.desal.2016.03.007.

[302] S. Zheng, Q. Tu, J.J. Urban, S. Li, B. Mi, Swelling of graphene oxide membranes in aqueous solution: characterization of interlayer spacing and insight into water transport mechanisms, ACS Nano (2017), https://doi.org/10.1021/acsnano.7b02999.

[303] H. Yu, Y. He, G. Xiao, Y. Fan, J. Ma, Y. Gao, R. Hou, X. Yin, Y. Wang, X. Mei, The roles of oxygen-containing functional groups in modulating water purification performance of graphene oxide-based membrane, Chem. Eng. J. 389 (2020), https://doi.org/10.1016/j.cej.2020.124375.

[304] C.J. Shih, S. Lin, R. Sharma, M.S. Strano, D. Blankschtein, Understanding the pH-dependent behavior of graphene oxide aqueous solutions: a comparative experimental and molecular dynamics simulation study, Langmuir 28 (2012) 235–241, https://doi.org/10.1021/la203607w.

[305] Y. Mo, X. Zhao, Y. xiao Shen, Cation-dependent structural instability of graphene oxide membranes and its effect on membrane separation performance, Desalination 399 (2016) 40–46, https://doi.org/10.1016/j.desal.2016.08.012.

[306] H. Huang, Y. Mao, Y. Ying, Y. Liu, L. Sun, X. Peng, Salt concentration, pH and pressure controlled separation of small molecules through lamellar graphene oxide membranes, Chem. Commun. 49 (2013) 5963, https://doi.org/10.1039/c3cc41953c.

[307] Y. Wei, Y. Zhang, X. Gao, Y. Yuan, B. Su, C. Gao, Declining flux and narrowing nanochannels under wrinkles of compacted graphene oxide nanofiltration membranes, Carbon 108 (2016) 568–575, https://doi.org/10.1016/j.carbon.2016.07.056.

[308] Y. Zhang, K. Su, Z. Li, Graphene oxide composite membranes cross-linked with urea for enhanced desalting properties, J. Membr. Sci. 563 (2018) 718–725, https://doi.org/10.1016/j.memsci.2018.06.037.

[309] W.S. Hung, Y.H. Chiao, A. Sengupta, Y.W. Lin, S.R. Wickramasinghe, C.C. Hu, H. A. Tsai, K.R. Lee, J.Y. Lai, Tuning the interlayer spacing of forward osmosis membranes based on ultrathin graphene oxide to achieve desired performance, Carbon 142 (2019) 337–345, https://doi.org/10.1016/j.carbon.2018.10.058.

[310] Z. Jia, W. Shi, Y. Wang, J. Wang, Dicarboxylic acids crosslinked graphene oxide membranes for salt solution permeation, Colloids Surf. A Physicochem. Eng. Asp. 494 (2016) 101–107, https://doi.org/10.1016/j.colsurfa.2016.01.023.

[311] Z. Jia, W. Shi, Tailoring permeation channels of graphene oxide membranes for precise ion separation, Carbon 101 (2016) 290–295, https://doi.org/10.1016/j.carbon.2016.02.016.

[312] Z. Jia, Y. Wang, W. Shi, J. Wang, Diamines cross-linked graphene oxide free-standing membranes for ion dialysis separation, J. Membr. Sci. 520 (2016) 139–144, https://doi.org/10.1016/j.memsci.2016.07.042.

[313] W.S. Hung, C.H. Tsou, M. De Guzman, Q.F. An, Y.L. Liu, Y.M. Zhang, C.C. Hu, K. R. Lee, J.Y. Lai, Cross-linking with diamine monomers to prepare composite graphene oxide-framework membranes with varying d-spacing, Chem. Mater. 26 (2014) 2983–2990, https://doi.org/10.1021/cm5007873.

[314] M. Hu, B. Mi, Enabling graphene oxide nanosheets as water separation membranes, Environ. Sci. Technol. 47 (2013) 3715–3723, https://doi.org/10.1021/es400571g.

[315] J.L. Han, X. Xia, Y. Tao, H. Yun, Y.N. Hou, C.W. Zhao, Q. Luo, H.Y. Cheng, A. J. Wang, Shielding membrane surface carboxyl groups by covalent-binding graphene oxide to improve anti-fouling property and the simultaneous promotion of flux, Water Res. 102 (2016) 619–628, https://doi.org/10.1016/j.watres.2016.06.032.

[316] H. Deng, P. Sun, Y. Zhang, H. Zhu, Reverse osmosis desalination of chitosan cross-linked graphene oxide/titania hybrid lamellar membranes, Nanotechnology 27 (2016), https://doi.org/10.1088/0957-4484/27/27/274002.

[317] A. Anand, B. Unnikrishnan, J.-Y. Mao, H.-J. Lin, C.-C. Huang, Graphene-based nanofiltration membranes for improving salt rejection, water flux and antifouling–A review, Desalination 429 (2018) 119–133, https://doi.org/10.1016/j.desal.2017.12.012.

[318] Y. Li, W. Zhao, M. Weyland, S. Yuan, Y. Xia, H. Liu, M. Jian, J. Yang, C.D. Easton, C. Selomulya, X. Zhang, Thermally reduced nanoporous graphene oxide membrane for desalination, Environ. Sci. Technol. 53 (2019) 8314–8323, https://doi.org/10.1021/acs.est.9b01914.

[319] I. Alsvik, M.-B. Hägg, Pressure retarded osmosis and forward osmosis membranes: materials and methods, Polymers 5 (2013) 303–327, https://doi.org/10.3390/polym5010303.

[320] V. Yangali-Quintanilla, Z. Li, R. Valladares, Q. Li, G. Amy, Indirect desalination of Red Sea water with forward osmosis and low pressure reverse osmosis for water reuse, Desalination 280 (2011) 160–166, https://doi.org/10.1016/j.desal.2011.06.066.

[321] S. Lee, C. Boo, M. Elimelech, S. Hong, Comparison of fouling behavior in forward osmosis (FO) and reverse osmosis (RO), J. Membr. Sci. 365 (2010) 34–39, https://doi.org/10.1016/j.memsci.2010.08.036.

[322] N.D. Suzaimi, P.S. Goh, A.F. Ismail, S.C. Mamah, N.A.N.N. Malek, J.W. Lim, K. C. Wong, N. Hilal, Strategies in forward osmosis membrane substrate fabrication and modification: a review, Membranes 10 (2020) 1–42, https://doi.org/10.3390/membranes10110332.

[323] L. Jin, Z. Wang, S. Zheng, B. Mi, Polyamide-crosslinked graphene oxide membrane for forward osmosis, J. Membr. Sci. 545 (2018) 11–18, https://doi.org/10.1016/j.memsci.2017.09.023.

[324] J. Jang, I. Park, S.S. Chee, J.H. Song, Y. Kang, C. Lee, W. Lee, M.H. Ham, I.S. Kim, Graphene oxide nanocomposite membrane cooperatively cross-linked by monomer and polymer overcoming the trade-off between flux and rejection in forward osmosis, J. Membr. Sci. 598 (2020) 117684, https://doi.org/10.1016/j.memsci.2019.117684.

[325] H. Salehi, M. Rastgar, A. Shakeri, Anti-fouling and high water permeable forward osmosis membrane fabricated via layer by layer assembly of chitosan/graphene oxide, Appl. Surf. Sci. 413 (2017) 99–108, https://doi.org/10.1016/j.apsusc.2017.03.271.

[326] H. Kang, W. Wang, J. Shi, Z. Xu, H. Lv, X. Qian, L. Liu, M. Jing, F. Li, J. Niu, Interlamination restrictive effect of carbon nanotubes for graphene oxide forward osmosis membrane via layer by layer assembly, Appl. Surf. Sci. 465 (2019) 1103–1106, https://doi.org/10.1016/j.apsusc.2018.09.255.

[327] I. Alam, L.M. Guiney, M.C. Hersam, I. Chowdhury, Pressure-driven water transport behavior and antifouling performance of two-dimensional nanomaterial laminated membranes, J. Membr. Sci. 599 (2020) 117812, https://doi.org/10.1016/j.memsci.2019.117812.

[328] H. Liu, H. Wang, X. Zhang, Facile fabrication of freestanding ultrathin reduced graphene oxide membranes for water purification, Adv. Mater. 27 (2015) 249–254, https://doi.org/10.1002/adma.201404054.

[329] F. Yan, C. Yu, B. Zhang, T. Zou, H. Zhao, J. Li, Preparation of freestanding graphene-based laminar membrane for clean-water intake via forward osmosis process, RSC Adv. 7 (2017) 1326–1335, https://doi.org/10.1039/c6ra27141c.

[330] E. Yang, C.M. Kim, J. ho Song, H. Ki, M.H. Ham, I.S. Kim, Enhanced desalination performance of forward osmosis membranes based on reduced graphene oxide laminates coated with hydrophilic polydopamine, Carbon 117 (2017) 293–300, https://doi.org/10.1016/j.carbon.2017.03.005.

[331] W.S. Hung, Q.F. An, M. De Guzman, H.Y. Lin, S.H. Huang, W.R. Liu, C.C. Hu, K. R. Lee, J.Y. Lai, Pressure-assisted self-assembly technique for fabricating composite membranes consisting of highly ordered selective laminate layers of amphiphilic graphene oxide, Carbon 68 (2014) 670–677, https://doi.org/10.1016/j.carbon.2013.11.048.

[332] Q. Wang, N. Li, B. Bolto, M. Hoang, Z. Xie, Desalination by pervaporation: a review, Desalination 387 (2016) 46–60, https://doi.org/10.1016/j.desal.2016.02.036.

[333] R. Castro-Muñoz, Breakthroughs on tailoring pervaporation membranes for water desalination: a review, Water Res. 187 (2020) 116428, https://doi.org/10.1016/j.watres.2020.116428.

[334] J.I. Paredes, S. Villar-Rodil, A. Martínez-Alonso, J.M.D. Tascón, Graphene oxide dispersions in organic solvents, Langmuir 24 (2008) 10560–10564, https://doi.org/10.1021/la801744a.

[335] J. Zhao, Y. Zhu, F. Pan, G. He, C. Fang, K. Cao, R. Xing, Z. Jiang, Fabricating graphene oxide-based ultrathin hybrid membrane for pervaporation dehydration via layer-by-layer self-assembly driven by multiple interactions, J. Membr. Sci. 487 (2015) 162–172, https://doi.org/10.1016/j.memsci.2015.03.073.

[336] D. Hua, R.K. Rai, Y. Zhang, T.-S. Chung, Aldehyde functionalized graphene oxide frameworks as robust membrane materials for pervaporative alcohol dehydration, Chem. Eng. Sci. 161 (2017) 341–349, https://doi.org/10.1016/j.ces.2016.12.061.

[337] K. Guan, Q. Liu, G. Zhou, G. Liu, Y. Ji, G. Liu, W. Jin, Cation-diffusion controlled formation of thin graphene oxide composite membranes for efficient ethanol dehydration, Sci. China Mater. 62 (2019) 925–935, https://doi.org/10.1007/s40843-018-9401-1.

[338] B.F. Machado, P. Serp, Graphene-based materials for catalysis, Catal. Sci. Technol. 2 (2011) 54–75, https://doi.org/10.1039/C1CY00361E.

[339] D. Higgins, P. Zamani, A. Yu, Z. Chen, The application of graphene and its composites in oxygen reduction electrocatalysis: a perspective and review of recent progress, Energy Environ. Sci. 9 (2016) 357–390, https://doi.org/10.1039/C5EE02474A.

[340] P. Yang, X. Yang, W. Liu, R. Guo, Z. Yao, Graphene-based electrocatalysts for advanced energy conversion, Green Energy Environ. 8 (2023) 1265–1278, https://doi.org/10.1016/j.gee.2022.06.008.

[341] X. Chen, W.-D. Oh, T.-T. Lim, Graphene- and CNTs-based carbocatalysts in persulfates activation: material design and catalytic mechanisms, Chem. Eng. J. 354 (2018) 941–976, https://doi.org/10.1016/j.cej.2018.08.049.

[342] M. Beltrán-Gastélum, M.I. Salazar-Gastélum, J.R. Flores-Hernández, G.G. Botte, S. Pérez-Sicairos, T. Romero-Castañon, E. Reynoso-Soto, R.M. Félix-Navarro, Pt-Au nanoparticles on graphene for oxygen reduction reaction: stability and performance on proton exchange membrane fuel cell, Energy 181 (2019) 1225–1234, https://doi.org/10.1016/j.energy.2019.06.033.

[343] X. Li, X. Huang, S. Xi, S. Miao, J. Ding, W. Cai, S. Liu, X. Yang, H. Yang, J. Gao, J. Wang, Y. Huang, T. Zhang, B. Liu, Single cobalt atoms anchored on porous N-doped graphene with dual reaction sites for efficient fenton-like catalysis, J. Am. Chem. Soc. 140 (2018) 12469–12475, https://doi.org/10.1021/jacs.8b05992.

[344] Y. Yan, J. Miao, Z. Yang, F.-X. Xiao, H.B. Yang, B. Liu, Y. Yang, Carbon nanotube catalysts: recent advances in synthesis, characterization and applications, Chem. Soc. Rev. 44 (2015) 3295–3346, https://doi.org/10.1039/C4CS00492B.

[345] M.D. Yadav, H.M. Joshi, S.V. Sawant, K. Dasgupta, A.W. Patwardhan, J.B. Joshi, Advances in the application of carbon nanotubes as catalyst support for hydrogenation reactions, Chem. Eng. Sci. 272 (2023) 118586, https://doi.org/10.1016/j.ces.2023.118586.

[346] Y. Cheng, S. Zhao, B. Johannessen, J.-P. Veder, M. Saunders, M.R. Rowles, M. Cheng, C. Liu, M.F. Chisholm, R. De Marco, H.-M. Cheng, S.-Z. Yang, S. P. Jiang, Atomically dispersed transition metals on carbon nanotubes with ultrahigh loading for selective electrochemical carbon dioxide reduction, Adv. Mater. 30 (2018) 1706287, https://doi.org/10.1002/adma.201706287.

[347] S. Chen, S. Perathoner, C. Ampelli, C. Mebrahtu, D. Su, G. Centi, Electrocatalytic synthesis of ammonia at room temperature and atmospheric pressure from water

and nitrogen on a carbon-nanotube-based electrocatalyst, Angew. Chem. Int. Ed. 56 (2017) 2699–2703, https://doi.org/10.1002/anie.201609533.

[348] J. Kang, H. Zhang, X. Duan, H. Sun, X. Tan, S. Liu, S. Wang, Magnetic Ni-Co alloy encapsulated N-doped carbon nanotubes for catalytic membrane degradation of emerging contaminants, Chem. Eng. J. 362 (2019) 251–261, https://doi.org/10.1016/j.cej.2019.01.035.

[349] B. Xia, Y. Yan, X. Wang, X.W. (David) Lou, Recent progress on graphene-based hybrid electrocatalysts, Mater. Horiz. 1 (2014) 379–399, https://doi.org/10.1039/C4MH00040D.

[350] W. Fan, L. Zhang, T. Liu, Graphene-CNT hybrids for environmental applications, in: W. Fan, L. Zhang, T. Liu (Eds.), Graphene-Carbon Nanotube Hybrids for Energy and Environmental Applications, Springer, Singapore, 2017, pp. 91–102, https://doi.org/10.1007/978-981-10-2803-8_4.

[351] P. Zamani, D.C. Higgins, F.M. Hassan, X. Fu, J.-Y. Choi, MdA. Hoque, G. Jiang, Z. Chen, Highly active and porous graphene encapsulating carbon nanotubes as a non-precious oxygen reduction electrocatalyst for hydrogen-air fuel cells, Nano Energy 26 (2016) 267–275, https://doi.org/10.1016/j.nanoen.2016.05.035.

[352] N. Pongpichayakul, P. Waenkeaw, J. Jakmunee, S. Themsirimongkon, S. Saipanya, Activity and stability improvement of platinum loaded on reduced graphene oxide and carbon nanotube composites for methanol oxidation, J. Appl. Electrochem. 50 (2020) 51–62, https://doi.org/10.1007/s10800-019-01368-1.

[353] E. Kusiak-Nejman, A.W. Morawski, TiO2/graphene-based nanocomposites for water treatment: a brief overview of charge carrier transfer, antimicrobial and photocatalytic performance, Appl. Catal. B Environ. 253 (2019) 179–186, https://doi.org/10.1016/j.apcatb.2019.04.055.

[354] R. Li, J. Huang, M. Cai, J. Huang, Z. Xie, Q. Zhang, Y. Liu, H. Liu, W. Lv, G. Liu, Activation of peroxymonosulfate by Fe doped g-C3N4/graphene under visible light irradiation for Trimethoprim degradation, J. Hazard Mater. 384 (2020) 121435, https://doi.org/10.1016/j.jhazmat.2019.121435.

[355] A.A. Isari, A. Payan, M. Fattahi, S. Jorfi, B. Kakavandi, Photocatalytic degradation of rhodamine B and real textile wastewater using Fe-doped TiO2 anchored on reduced graphene oxide (Fe-TiO2/rGO): characterization and feasibility, mechanism and pathway studies, Appl. Surf. Sci. 462 (2018) 549–564, https://doi.org/10.1016/j.apsusc.2018.08.133.

[356] A.O. Oluwole, E.O. Omotola, O.S. Olatunji, Pharmaceuticals and personal care products in water and wastewater: a review of treatment processes and use of photocatalyst immobilized on functionalized carbon in AOP degradation, BMC Chemistry 14 (2020) 62, https://doi.org/10.1186/s13065-020-00714-1.

[357] R. Baby, B. Saifullah, M.Z. Hussein, Carbon nanomaterials for the treatment of heavy metal-contaminated water and environmental remediation, Nanoscale Res. Lett. 14 (2019) 341, https://doi.org/10.1186/s11671-019-3167-8.

[358] A.K. Singha Deb, V. Dwivedi, K. Dasgupta, Sk Musharaf Ali, K.T. Shenoy, Novel amidoamine functionalized multi-walled carbon nanotubes for removal of mercury(II) ions from wastewater: combined experimental and density functional theoretical approach, Chem. Eng. J. 313 (2017) 899–911, https://doi.org/10.1016/j.cej.2016.10.126.